Shock and Vibration Characteristics of a Bio-Inspired Structure under Blast Loading

Author: Jason Mathews – Masters Student,

New Mexico Institute of Mining and Technology, Mechanical Engineering Department, 801 Leroy Place Socorro, NM 87801

Advisor: Dr. Ashok Ghosh

Abstract

This paper will introduce the topics related to, and research done on several aspects of, blast loading of porous structures. This paper will also report the findings of a blast load study on a bio-inspired porous structure, along with further testing results from Split Hopkinson Bar testing, analytical modeling, and computer modeling of the structure. The blast loading tests were performed at the Energetic Materials Research and Testing Center (EMRTC) in conjunction with New Mexico Institute of Mining and Technology's (NMT) Mechanical Engineering Department to characterize an engineered porous structure under blast loading. The structure was subjected to impulsive loads of varying magnitudes produced by the detonation of one-pound hemispheres of C-4. Variables considered in this experiment included the geometry of the structure, the material makeup of the structure, dynamic characteristics of the structure, and the magnitude of the air blast due to varying standoff distances. Experimental data including acceleration, reflected pressure, and structural deflection were collected in the field at EMRTC using accelerometers, pressure gauges, and digital high-speed cameras.

Acknowledgements

I would like to thank the following for their help during my thesis research:

Dr. Ashok Ghosh for his help and patience throughout my research and writing

Nick Spinhirne for his help during the sample construction phase

Jason Metzger for his help with testing and getting testing time at EMRTC

Dr. Thomas Duffy for his introduction into explosive analysis and litterature

Dr. Warren Ostergren for his personal skills and the use of the design class report on their Split Hopkinson Bar

Dr. Andrei Zagrai for his help with sensors and the preliminary test set up and experience in Mechatronics

Dr. Yilmaz for handling my various questions throughout the research

Dr. B for this opportunity and his patience and efforts towards this research

Dr. Keith Miller for fielding my numerous questions and his help in finding people and information

Dr. Bin Lim for fielding my questions and his help with AUTODYN

James Peralta for his help during the EMRTC testing

Ordnance Tech's for their help during the EMRTC testing

Iris Pascal for their help with several questions

M.R.O. for the testing space and their interest in the research

Dr. Chen from Purdue University for his Split Hopkinson bar expertise and fielding my various questions

Dr. Frew from Sandia National Laboratories for his Split Hopkinson bar expertise and fielding my various questions

Dr. Romero for his support and finding me a place to conduct my research

Table of Contents

Section **Page**

List of Tables

List of figures

List of Abbreviations

EMRTC = Energetic Materials Research and Testing Center

AFRL = Air Force Research Laboratories

Approval Page

1. Introduction

1.1 Bio-Inspired Structures

Biological concepts have become sources of inspiration for those wanting to create new, or improve upon the existing. The evolutionary "strategy" [1] that has created structures such as bone, wood, and even flower stems has created them so that they are uniquely adapted and extraordinarily engineered for multifunctions.

> *"Billions of years of evolution have given mankind a wide variety of biological solutions to materials problems. The challenge lies in identifying relevant defense applications and understanding and manipulating the biological systems to solve them. It must be borne in mind, however, that the actual use of biological materials that mimic biological systems lags far behind our enthusiasm for them. With a few notable exceptions, these bimolecular materials remain the materials of the future: despite an extraordinary rate of progress in the field, they are likely to be materials of the future for a number of years."* [1]

Bio-inspired structures have been, and continue to be, utilized in industry, everyday life, and even military applications.

> *"Mankind has been using biological materials for defense purposes for millennia: wooden staffs for spears or axe handles, vines for ropes, snake venom or plant extracts for biological weapons, shaped bone*

for tools and weapons…, multilayered abalone shell could point the way toward a new tough, lightweight vehicle armor, and spider silk fibers could become the basis for enhanced protection of personnel." [2]

Using biological structures to inspire new structures based on physical properties or phenomena or to actually implement them into a structure to utilize those desired properties has proven to be a challenging task. Yet, successfully implemented into a design, and used for idea forming for possible new and better structural designs and materials, bio-inspired structures and materials have helped mankind to quicken the development of better and more useful designs and structures. Some examples of successful implementation of bio-inspired structures include helmets, skull bone inspired, swaying of skyscrapers to prevent failure of the building due to winds, tall tree inspired, and even sensor arrays used in structural health monitoring and nondestructive evaluation, nervous system inspired. [3]

1.2 Bone Structure

The dynamic load carrying capabilities of skull bone was the inspiration for this thesis project. Skull bone is comprised of 70% collagen [4]. This is the hard outer layer of the bone. The inner layer of bone is composed of marrow and blood. The marrow is a porous sponge like material that is interwoven in the cancellous structure of bone. [5]

"Bone is a relatively hard and lightweight composite material, formed mostly of calcium phosphate in the chemical arrangement termed

calcium hydroxyapatite. It has relatively high compressive strength but poor tensile strength. While bone is essentially brittle, it does have a degree of significant elasticity contributed by its organic components (chiefly collagen). Bone has an internal mesh-like structure, the density of which may vary at different points.

Bone can be either compact or cancellous (spongy). Cortical (outer layer) bone is compact; the two terms are often used interchangeably. Cortical bone accounts for 80% of the total bone mass of the adult skeleton. Because of its high density it accounts for approximately 10% of the total surface area. Cancellous bone is trabecular (has an open, meshwork or sponge-like structure). It has a relatively high surface area (about 10 times that of cortical bone) and it accounts for approximately 20% of the total bone mass."[5]

Some pertinent characteristics of skull bone are that:

- Cancellous bone is functionally graded, open-celled, and rod-like where stresses are low, and it changes to an approximately shell-like structure at points of higher stress.
- Cancellous bone structure is a piezoelectric material that has been suggested to be responsible for stress-induced growth in its material structure. This means that it is adaptive to its environment. [6]

Bone is comprised of ~25% fluid and the remaining 75% contains organic and mineral components. It has been demonstrated that significant dampening caused by fluid flow occurs only above 1 MHz frequencies of mechanical loading, and that below 1 MHz the pore fluid pressures required for dampening through mechanical transduction are extremely low. Transduction is the process of converting one type of energy into another. In this case the vibration energy is converted to pressure and strain energy in the material. [5] It has been demonstrated that skull bone has significant impact and sound dampening characteristics from 0.2 – 2 MHz frequencies. This is said to be due to the reflective characteristic of the outer shell and the dampening characteristic of the organic, porous, pressurized, fluid filled structure of the inside bone. This phenomenon has inspired a great deal of different materials that try to mimic skull bone. [6,7,8]

Bovine bone is one of the closest bone structures to human bone. Vibration tests have been conducted on bovine bone, and it has been determined that the bone exhibits vibration dampening characteristics at frequencies over 1 MHz. [9] This is with the outer and inner bone together.

1.3 Porous Media

Stress-strain behavior of many artificial cellular materials (foams) used in energy absorption products like impact limiter in packaging and crush padding are similar to bone characteristics. Foams are typically formed by generating bubbles in a liquid medium. After nucleation the bubbles grow and pack together. When bubbles make contact with each other, a flat surface defines the boundary between two neighboring

bubbles. The bubbles then become polyhedral cells. At some point the liquid solidifies and the result is a cellular solid or foam. If the faces of polyhedral remain intact it is closed-cell foam. If the cell walls are broken, only the cell edges remain intact and the resulting structure is referred to as open-cell foam. Figure 1 (a) shows a 2-D natural structure and (b) an artificial 3-D open celled foam structure.

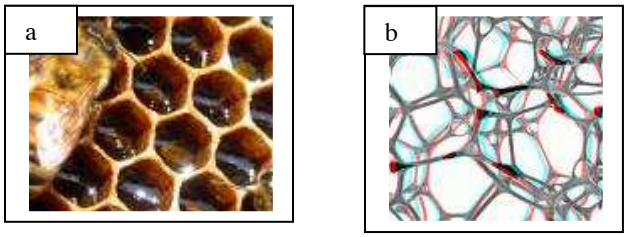

Figure 1: (a) Honey comb- A 2-D cellular structure with ends open; (b) 3-D open celled foam.

Relative density of cellular solid (ratio of density of cellular material to density of the solid from which the cell walls are made), can be as low as 0.001. Almost any material can be foamed. Polymers, of course, are the most common.

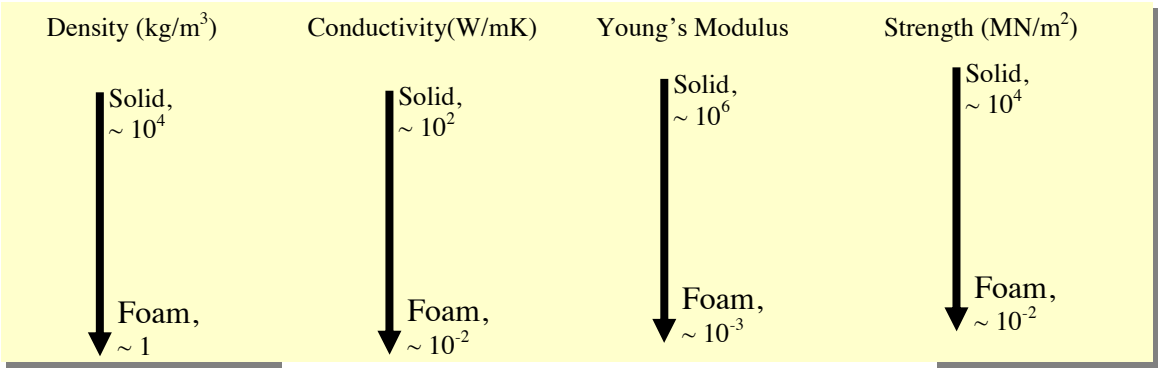

Figure 2: Variation of properties due to foaming (16)

Cellular solids have various other characteristics. They have high damping characteristics. They are used as impact limiter. They have useful electrical properties. The attenuation of electromagnetic waves, for instance, depends on the dielectric loss in the medium through which they travel. Natural structures are very complex in their morphology.

Foam materials are used in several applications for their energy absorptive properties. Packaging materials such as polystyrene, polyurethane and polyethylene are used as packaging materials for a few reasons. Some of these reasons include the low density of foam materials, which means that the package can be protected without adding a large amount of mass. This in turn reduces shipping cost while protecting the package. Foams are also relatively easy to mold and therefore packages can be molded into the foam to give added impact absorption. The energy absorptive property of these foams comes from their ability to have high compression (~0.7 strain) at an almost constant stress. This means that a large amount of energy can be absorbed without generating high stresses. The same principles have been used in aircraft to reduce weight and relieve stresses in the shell of the plane. Adding fibers and honeycomb structures also give the material a high specific bending stiffness and strength without added weight. These materials are also used in car seats, couches, and chairs not only for their compressive and energy absorption capabilities but also because when the load is let off of the foam, the foam regains its original shape. Polyurethane foam is one prime example of this because it has a quick recovery "rubbery" type property that allows for large compression without permanent displacements.

These porous media can be said to be bio-inspired materials. Foams have been used in products such as helmets, carpet cushioning, and car seats because of their energy absorption and impact resilience. Helmets, especially, are inspired by bone, skull bone to be precise.

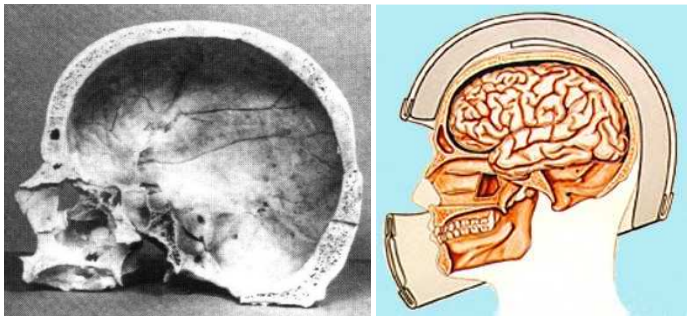

Figure 3: Comparing Skull bone and helmet cross-sections

A helmet is an added "skull" used to protect the user's brain from shock, impact, and severe injury. The foam coupled with the hard outer shell makes for a high strength energy absorptive material. Foams can also be used for blast load absorption and protection. Many different foam materials are used in structures for their light weight, sound dampening, insulating, and impact resistant qualities. Such applications include sandwich paneling on commercial aircraft [10]. Different porous media have different general material properties as shown in figure 2.

Studies have been conducted using polyurethane foam spray on masonry walls for protection against blast loading [11, 12]. Foams used as cladding between structures or sandwiched between rigid plates for building protection against explosions have also

been studied [12-21]. Even ordnance storage facilities have used the energy absorption properties of foams [22]. An SEM picture of metal coated polyurethane foam is given in the figure 4.

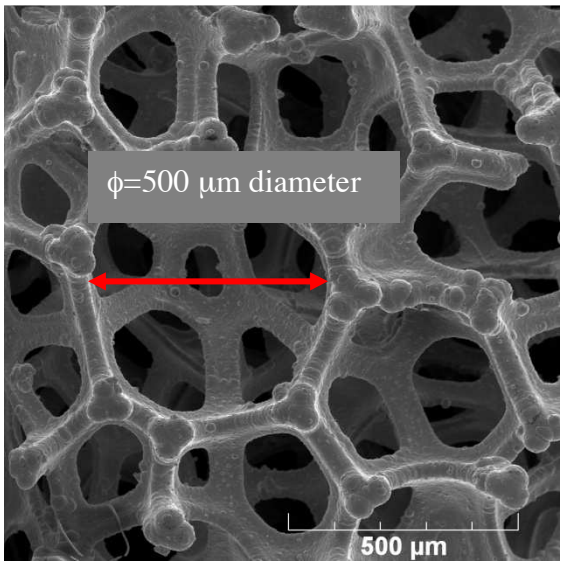

Fig. 4: SEM of a Metal Foam (RECEMAT); Over 95% cavities;

Polyurethane foam is often created by adding small amounts of blowing agents, volatile substance, to the polyurethane reaction mixture. The most common way to produce foams is to add water to one of the liquid precursors of polyurethane prior to mixing them together. This reacts with a portion of the isocyanate, a functional group in polyurethane –N=C=O (1 nitrogen, 1 carbon, 1 oxygen), generating carbon dioxide bubbles in the liquid. These bubbles and the liquid polyurethane then harden to form a solid foam structure. [23]

There are two main structures of foam. One structure is formed when the foam bubbles remain closed, and the gas forms closed cell cavities within the foam structure. The other structure being when the foam has mostly open cells (bubbles), resulting after a critical stage in the foam-making process. For foam to be flexible the cells are required to be of the open structure. [23]

For a given porous media, the fluid flow of a viscous fluid can contribute to the energy absorption and dissipation capacity of the material. Allowing the energy of loading to be converted to the energy required to initiate and keep fluid flow dynamic energy is dissipated by means of the small area of the flow passage and the viscosity of the fluid. [24, 25, 26] As pressures differ in an elastic media the fluid pressure can also dissipate energy through deformation of the media that the fluid flows through. One other energy absorption factor comes from frictional losses between the fluid and the porous/fibrous media/structure. [27]

The viscous flow through a media can also contribute to the strength of an elastic media. This can be seen in Darcy's law [28] [29]:

$$\vec{q} = -\frac{k}{\mu}\vec{\nabla}p \text{ (Flow)} \qquad \text{(eq. 1)}$$

where q (or q with a bar on top) is the flow velocity, μ the dynamic viscosity of the fluid, κ is a unit area of permeability, and p the fluid pressure [28]

$$\sigma_g = \frac{C\mu\varepsilon^*}{1-\varepsilon}\left(\frac{L}{l}\right)^2 \qquad \text{(eq. 2)}$$

Where σ_g is the contribution of a viscous pore fluid to the strength; C is the constant of proportionality; μ is the viscosity of the fluid; ε^* is the strain-rate; ε is the strain; L is the length of a block of foam; and l is the cell-edge length [6].

As for relating the permeability, k, of a porous media to the relevant structural characteristics the Kozeny-Carman equation is one the most widely used models.

$$k = \frac{1}{c\tau^2 S_o^2}\frac{\phi^3}{(1-\phi)^2} \qquad \text{(eq. 3)}$$

Where ϕ is the porosity, S_o the specific surface area, (i.e. pore-surface area in a unit volume of the solid material), τ the tortuosity (i.e. the ratio of the average length of the flow paths to the thickness of the sample), and c the dimensionless Kozeny's constant [28].

Quick recovery polyurethane foam (PU) was used to simulate the cancellous trabecular structure in bone for the current tests. . This foam is open celled, which is useful for the introduction of a fluid into the pores of the foam. This helps more closely to mimic the fluid structure interaction in bone. The foam is also elastic with a quick recovery

characteristic, which adds to the energy dissipation in the foam while allowing for rapid recovery to the original shape after loading. The foam used is a:

- non-adhesive backed, half-inch thick foam.
- The foam has a firmness rating of 4 (at ambient conditions, it takes approximately 4 psi to indent the sample a distance of 25% of its original thickness).
- a density of 15lb/ft^3.
- a tensile strength of 40 psi.
- 4-8 psi is required to compress the foam by 25% depending on environmental conditions [30].

1.4 Modeling

Modeling of a foam system can pose quite a challenge. Mathematical, analytical, and numerical models of different porous media and plate structures can be looked at to decide how best to approach this problem.

For a basic model of a foam structure a cubic cell with a series of beams, shown figure 5 [31], joining with other cells at the center of the beams can be used, but this model inherently has geometrical limitations and can cause errors.

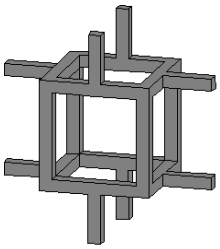

Figure 5: Cube Beam Structure for Foam Pores.

A trabecular structure is often used to model porous media. A cubic cell uses a series of square beams loaded in the center, while the trabecular structure uses circular beams loaded at the corners of the cell. In cancelous bone, and most foam, circular beams are most common.

This model works under the condition that the material has limited elasticity and is an ideal material. Different finite element meshing was studied in detail by Ulrich, D., Van Rietbergen, B., Weinans, H., and Ruegsegger, P. [32] in order to understand and more closely model the characteristics of cancellous bone. Shown below in figure 6 are two meshes that most closely matched with previous experimental investigation.

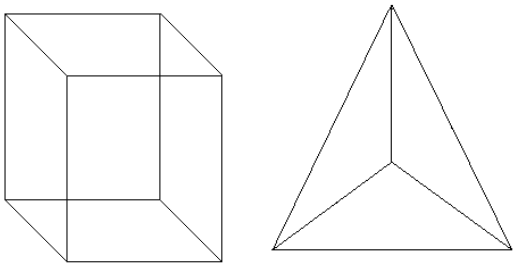

Hexahedral element Tetrahedral element

Figure 6: Hexahedral and tetrahedral elements

Lee and Lakes [32] demonstrated that both the elements, hexahedral and tetrahedral, validate bone compression tests. Both meshing styles closely described experimental results depending on the type and structure of the bone being studied. For these meshing styles to match closely with experimental data the meshing resolution had to be at least 84μm. A meshing size of 168μm yielded results that differed greatly from experimental results in stresses and Young's Modulus of the cancellous bone.

PU foam has been determined to have nonlinear and viscoelastic properties. Three widely used finite element models of this foam structure include bubbles with viscoelastic shells, 3D honeycomb with tetrakaidecahedron (Kelvin cell), and a combination of the two allowing the bubble structure to expand to the honeycomb structure. [33]

Most properties of foams depend on their relative densities [34]. For an open celled foam;

$$\frac{\rho^*}{\rho_s} = C_2\left(\frac{t}{l}\right)^2\left(1 - D_4\frac{t}{l}\right) \qquad \text{(eq. 4)}$$

Where C_2 is a foam's constant dependent on cell geometry, t is the cell wall thickness, l is the edge length of the cell, ρ_s is the density of the solid portion of the foam, ρ^* is the equivalent density of the foam, and D_4 is a correction factor which can be ignored if the relative density is less than 0.2. [31]

Many properties of foams also depend on the mean cell diameter in the material.

$$\bar{L}_1 = \frac{1.5}{N_c} \qquad \text{(eq. 5)}$$

Where L_1 is the mean cell diameter, and N_c is the number of cells per unit length (usually measurements taken in microscopes). [31]

The anisotropy of a foam material can be derived by determining L_1, L_2, L_3 (the x, y, and z lengths) in the above method. Another way to determine this anisotropy of the material is to use the mean intercept length in the principle directions. This can also be used in place of the dispersion of cell sizes in the material as such a value can be quite difficult to obtain depending on the cell size. The basic concept of H, the mean intercept length from the center of a pore to its boundaries, is shown in matrix form below. The anisotropy of the pores can affect the modulus of the foam in the x, y, and z directions.

Looking more towards the macro mechanical behavior of an elastic porous structure it should be taken into consideration that most "elastic cellular polymers are foam rubbers." [35] In a porous material a very important mechanical characteristic is its relative Young's modulus:

$$\frac{E_f}{E} \qquad \text{(eq. 6)}$$

Where E is the Young's modulus of the solid phase and E_f is the effective Young's modulus of the porous material. [34] The modulus of the solid phase can be estimated as follows for small strains.

$$E_s = \frac{3\rho_s RT}{M_e} \qquad \text{(eq. 7)}$$

Where ρ_s is the density of the solid phase, R is the relative gas constant of the gas surrounding the material, T is the temperature, and M_e is the average molecular weight between cross links. [36]

When looking at the modulus of a polymer one can see in the figure below that the modulus can change significantly depending on the loading time or rate.

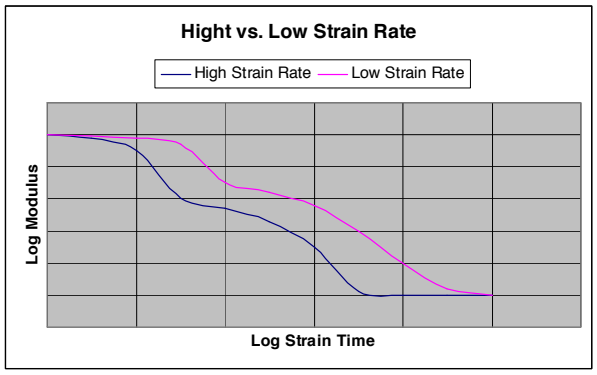

Figure 7: Modulus vs. Stress Time to Failure.

For an elastic porous material it has been determined that the use of small cubic cells of random orientation with at least four strut structures inside is the best at estimating strut end forces and structure displacement (figure 5). This relates q, φ (volume fraction of the solid phase in the porous material, ν Poisson's ratio, E, and E_f as follows [36] :

$$E_f = \frac{24E}{q_1[28q_1 + 16(1+\upsilon)q + 64q^3]}$$

$$\varphi = \frac{\sqrt{3q} + \frac{1}{6}\sqrt{2}}{8\sqrt{3(q + \frac{1}{2}\sqrt{6})^3}} \qquad \text{(eq. 8-10)}$$

$$q_1 = q + \frac{1}{2\sqrt{6}}$$

This model has yielded close values to experimental observations in elastic porous materials at an approximate volume fraction of 0.1. [35]

Using the volume strain, Θ, relation with the critical buckling force relation, F_{cr}, and the Poisson ratio of the porous material, ν_f, the critical strain, $\varepsilon_{cr,}$ can be determined at the point of critical buckling [35].

$$\Theta = -0.08t$$

$$F_{CR} = -\frac{\pi^2 EJ}{4L^2} \qquad \text{(eq. 11-14)}$$

$$\Theta_{CR} \approx \frac{\pi^3}{72}\upsilon_f$$

$$\varepsilon_{CR} = \frac{\Theta_{CR}}{1-2\upsilon_f}$$

Where L is the length of the struts, and J is the second moment of area of its transverse cross section about the x axis.

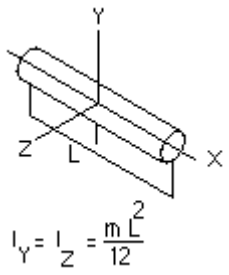

Figure 8: Second Moment of Area

The critical strain is one of the most important basic characteristics of a porous material. [35] The critical strain, ε_{cr} is important until the critical strain is reached and the material behaves in a linear fashion. After the critical strain has been reached, the materials modulus decreases at a rapid rate. If the material has not failed, once the load has been taken off the materials modulus increases again rapidly until the critical strain is reached and the material again follows the relative modulus to the original unstrained state. [23]

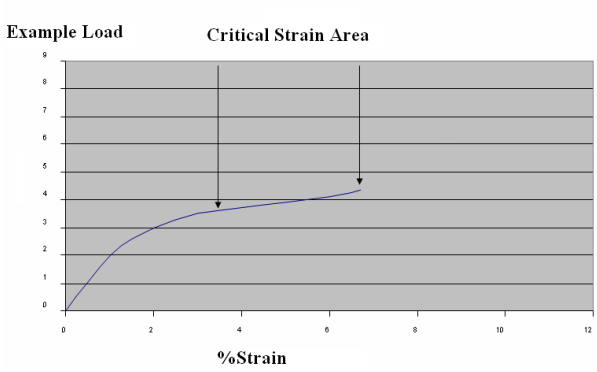

Figure 9: Critical Strain Portion of Loading under an example load, Mpa.

Three different approaches have often been used to attempt modeling the elastic along with the visco-elastic characteristics of foams.

1) One method focuses on the macroscopic response of the foam while making assumptions about the microstructure characteristics of the cellular solid. This method has the inherent issue of assuming and not calculating the microstructure characteristics and taking them into account. [37]

2) The second method commonly used assumes that the foam is a rubbery continuum. This solely focuses on the macro-mechanical behavior of the structure while not taking the porous characteristic of the material. This method neither considers micromechanical characteristics nor carries room for different cellular material characteristics that can change and affect the macro-mechanical characteristics differently in different materials. [37]

3) The third approach is phenomenological. This approach takes experimental data and uses that data to derive a model of the material. With this approach, prediction of individual loading situations can be useful. It does not, however, show anything about different loading situations or give a predictive model for other types of foam structures. [37]

The Ogden Model [37] has been used to improve the estimation techniques used in determining the mechanical characteristics of elastic and viscoelastic foams. This model has given very close values to the experimental values.

$$\psi = \sum_{l=1}^{L} \frac{\hat{\mu}_l}{\gamma_l}(\lambda_1^{\gamma_l} + \lambda_2^{\gamma_l} + \lambda_3^{\gamma_l} - 3) + \tilde{\psi}(J)$$

$$P_i = \frac{\partial \psi}{\partial \lambda_i}' i = 1,2,3 \qquad \text{(eq. 15-17)}$$

$$F_O = P_2 h_1 h_3 = \frac{1}{\varepsilon + 1} \sum_{l=1}^{L} \mu_l [(\varepsilon + 1)^{\gamma_l} - 1] + \int_0^t \sum_{n=1}^{N} a_n e^{-\alpha_n (t-\tau)} \varepsilon(\tau) d\tau$$

Where $\mu_l = h_1 h_3 \mu_l \psi$ is the strain energy, λ_i are principal stresses, μ_l and γ_l are the fitted parameters, ε is the strain, $J = \lambda_1 \lambda_2 \lambda_3$, and P_i is the first Piola-Kirchhoff stress.

A series of steps have been developed to identify some important variables used in Ogden's Model. Ogden's Model takes into account both the elastic and visco-elastic characteristics of the porous material in question.

While this model has proven to have very close results to experimental data at the Ray W. Gerrick Laboratories in conjunction with the School of Mechanical Engineering at Purdue University, it has been shown that the iterative process is very slow. Even with good initial assumptions 1000 to 3000 iterations are required to achieve convergence. [37]

Based on the Ogden strain-energy function the elastic and visco-elastic stresses have been derived as follows in terms of engineering strain. The terms are the same as in equations 15-17 [formatting should be same of eq or equation].

$$\sigma_E = \frac{1}{1+\varepsilon}\sum_{k=1}^{K}\mu_k[(1+\varepsilon)^{\gamma_k} - 1]$$

$$\sigma_V = \int_0^t \sum_{l=1}^{L} a_l e^{-\alpha_l(t-\tau)}\varepsilon(\tau)d\tau - \sum_{l=1}^{L}\frac{a_l}{\alpha_l}\varepsilon \qquad \text{(eq. 18-19)}$$

where the bulk modulus K and the thermal conductivity α_1 have been taken into consideration.

Since the foam pore geometry is not perfect in shape, and the model assumes that they are, an additional ε_o has to be added to the strain term to shift the strain axis to accommodate for this. This can only be seen while comparing calculated values to experimental data. The issue with this model and estimation is that it has only been tested at exceedingly slower strain rates than those seen under blast loading. [38]

Another factor that can be taken into consideration using FEA to analyze such a structure is that the cell or pore structure inside the material can have a significant effect on the results. The factors μ and γ in the Ogden model have been shown to be significantly altered depending on the foam microstructure chosen. [40] The model provides a good description of the uniaxial compression of a two-dimensional Voronoi honeycomb structures, also honeycomb structures with convex hulls [41], and boundaries that make up the smallest polygon that defines the exterior of a set of points defining a pore [41]. This model only gives good results up to 10% strain.

A previous attempt was made to model the polyurethane foam using FEA techniques by Nick Spinhirne, a graduate student at New Mexico Tech. This was done using compression test data from the foam manufactures' loaded into an ANSYS finite element program. Using a unit cell (pore) of p x p x p (p = pore side length) the volume can be considered unity so that the porosity is p^3. The polynomial form hyper-elastic material model was used to limit the number of coefficients needed in the model with more accuracy than a Blatz-Ko foam model at relatively large strains. The Blatz-Ko strain energy density function is useful for modeling compressible polyurethane foam type rubbers. The form of strain energy potential for the Blatz-Ko model is:

$$W = \frac{\mu}{2}\left(\frac{I_2}{I_3} + 2\sqrt{I_3} - 5\right) \qquad \text{(eq. 20)}$$

Where μ is the initial shear modulus of the material and I is the moment of inertia in the principle directions. The initial bulk modulus of the material is defined below.

$$k = \frac{5}{3}\mu \qquad \text{(eq. 21)}$$

A structure type Solid 187 (tetrahedral solid), shown below, was used in ANSYS due to its ability to model visco-elastic behavior of a material under deformation conditions.

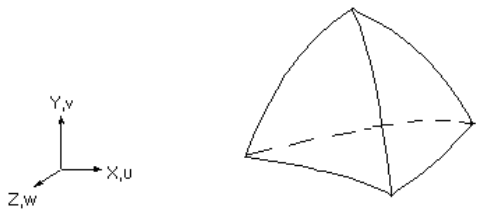

Figure 10: ANSYS Solid 187 tetrahedral solid

The strain energy potential in this model is defined by:

$$W = \sum_{i+j=1}^{N} c_{ij}(\bar{I}_1 - 3)^j + \sum_{K=1}^{N} \frac{1}{d_k}(J-1)^{2k} \qquad \text{(eq. 22)}$$

"where I_1 "(bar)" and I_2 "(bar)" are the first and second deviatoric strain invariants, J is the determinant of the elastic deformation gradient F, and N, c_{ij}, and d are material constants" [42]

This model still needs refinement in areas such as element size and number. Spinhirne used a smaller mesh size than the initial model and produced better but still incorrect results. It was theorized that the use of an even smaller mesh might correct the error, but no adequate computer was located to attempt this.[42]

Different mathematical models have been presented to calculate the effective elastic properties of porous materials. One such model is the composite sphere model (CSM).

$$\frac{K_*}{K_o} = \frac{2(1-2\upsilon_o)(1-\phi)}{2(1-2\upsilon_o)+(1+\upsilon_o)\phi}$$

$$\frac{E_*}{E_o} = \frac{(1-\phi)^2}{1+(2-3\upsilon_o)\phi} \qquad \text{(eq. 23-25)}$$

$$\frac{\mu_*}{\mu_o} = \frac{4(1+\upsilon_o)(1-\phi)^2}{4(1+\upsilon_o)+(11-19\upsilon_o)\phi}$$

K_*/K_o is the effective elastic modulus, E_*/E_o is the effective Young's modulus, μ_*/μ_o is the effective sheer modulus, and ϕ is the porosity of the material. The composite sphere model matches close to experimental data but tends to be increasingly higher as the porosity increases. [43]

R. W. Zimmerman came up with these equations for the elastic moduli.

$$\frac{K_*}{K_o} = \frac{2(1-2\upsilon_o)\frac{\mu_*}{\mu_o}}{(1+\upsilon_o) = (1-5\upsilon_o)(\frac{\mu_*}{\mu_o})^{\frac{3}{5}}}$$

(eq. 26-27)

$$\frac{\mu_*}{\mu_o} = \frac{(1-\phi)^2}{3(1-\upsilon_o)}[2(1-\upsilon_o) + (1-5\upsilon_o)(\frac{\mu_*}{\mu_o})^{\frac{3}{5}}]^{\frac{1}{3}}$$

The Zimmerman model matches even closer to experimental data for the modulus of visco-elastic materials but tends to be slightly low and adjustments are usually made if necessary.

A model from Liangsheng Wang and Kevin K. Tseng [44] came even closer for most porous materials.

$$\frac{K_*}{K_o} = \frac{2(1-2\upsilon_o)(1-\phi)}{2(1-2\upsilon_o) + (1+\upsilon_o)\phi}$$

$$\frac{\mu_*}{\mu_o} = \frac{(7-5\upsilon_o)(1-\phi)}{7-5\upsilon_o + 2(4-5\upsilon_o)\phi}$$

(eq. 28-30)

$$\frac{E_*}{E_o} = \frac{2(7-5\upsilon_o)(1-\phi)}{2(7-5\upsilon_o) + (1+\upsilon_o)(13-15\upsilon_o)\phi}$$

These equations become much longer if inter-pore interaction is taken into consideration.[44]

Taking impact, bending, and the foam being a strain rate dependent material into consideration the following equations have been used in structural impact dynamics to describe an elastic/plastic material under impulsive loading situations. [44]

$$\dot{\varepsilon} = D\left(\frac{\sigma_o' - \sigma(\varepsilon)}{\sigma_o}\right)^q$$

or

$$\dot{\varepsilon} = D\left(\frac{\sigma_o'}{\sigma(\varepsilon)} - 1\right)^q \qquad \text{(eq. 31-33)}$$

with

$$\dot{\varepsilon} = \frac{\dot{\sigma}'}{E}$$

Where σ'_o is the dynamic flow stress, $\dot{\varepsilon}$ is the uniaxial plastic strain rate, D and q are constants for the material, and σ_o is the associated static flow stress. [44]

One important note to take into consideration is that the pressure pulse, blast wave, does not just affect the front of the plate being tested. It also wraps around the sample and has a pressure affect on the back of the sample. This has been studied by modeling plate structures using FEA and comparing the results to experimental data. [45]
This leads to trying to distribute the pressure on the faces of the model to simulate an actual blast loading of thin structure.

The main deformation mechanism for open celled foams is through cell face bending. An example for elastic open cell polyurethane foam can be seen below [31]:

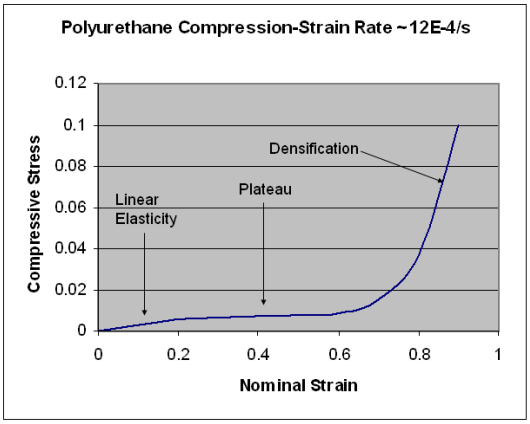

Figure 11: Compressive Stress vs. Strain Curve for Open Cell Polyurethane Foam. [31]

This increases the stiffness of the foam under tension and/or compression. E, G (sheer modulus), and v all have relations to solid modulus and densities of the foam material before foaming [31].

$$\frac{E^*}{E_s} = \left(\frac{\rho^*}{\rho_s}\right)^2$$

$$\frac{G^*}{E_s} = \frac{3}{8}\left(\frac{\rho^*}{\rho_s}\right)^2 \qquad \text{(eq. 34-36)}$$

$$\upsilon^* = \frac{1}{3};(approximately)$$

Under pure hydrostatic loading there becomes a linear dependence on the bulk modulus, K, of the material. This shows a change in dependence when fluid is added to the system.

$$\frac{K^*}{E_S} = \frac{1}{9}\left(\frac{\rho^*}{\rho_s}\right) \qquad \text{(eq. 37)}$$

With cells that contain fluid in foam the permeability, K, of the foam comes into play. This can help strengthen the foam material with added mass and viscosity from the fluid. [46]

$$K = 0.4\left(1 - \frac{\rho^*}{\rho_s}\right)^{\frac{3}{2}} d^2 \qquad \text{(eq. 38)}$$

Where d is the average cell diameter in the foam. This adds to the strength of the material through equation 2.

Where C is the combined constant of proportionality, μ is the fluid viscosity, L is the length of the sample, and l is the average side length of the cells.

1.5 Energy Absorption

The main idea behind impulse energy absorption is to construct a structure that can dissipate the energy through the means of deformation or energy dispersion. A widely used method is deformation of a material to absorb more energy from impact. This is used in structures as simple as guard rails on highways. To allow for added deformation before failure creates a situation where a substantial increase in impact energy absorption can be achieved.

Using deformation in the middle layer of sandwich plates is a relatively new technique in blast protection. Three types of middle layer structures are commonly used: pyramidal

truss, square honeycomb, and folded/corrugated plate. [47] Again, increasing the deformation allowable in these structures vastly increases their impulsive loading energy absorption before failure.

Another factor to look at is that the sound speed in air is much slower than the sound speed in a fluid. This is due to the fact that a fluid is much denser than air. This denseness is added mass for a wave to push. Studies have shown that the momentum transfer in air from a blast load is 2-3 times higher than the momentum transfer in water because of its greater density. Theoretically this would mean that if the middle layer of a sandwich structure was filled with water the back plate of the structure would see approximately $1/3^{rd}$ of the impulsive loading that is would see if the structure was filled with air, decreasing as the structure is compressed. [47]

Since water decreases the amount of energy transferred to a plate material, studies have been conducted with plates of different thicknesses resting on water with a blast load from above. When compared to tests with only air surrounding the plate a range of 30-50% reduction in plate deformation was observed depending on the plate thickness and radius. When H/R (height/radius) of a circular plate = 0.04, a reduction in maximum deformation of ~30% was observed. When the H/R= 0.015 the reduction in maximum deformation was ~50%. For most cases an average of 40% reduction in deflection was observed. [48]

The use of foam plates is another approach to the impulse energy absorption problem. Aluminum foam plates have been tested in explosive/impulsive loading situations to determine if their use would allow for more energy to be extracted from close range blast loading. Experiments were conducted using a pendulum with a mass at the end. The mass was covered with aluminum foam on the side facing the blast.

Near field blast tests were conducted. It was found that the foam allowed for more energy absorption from the blast load. The foam material would keep a pressure equivalent to the foam materials crushing strength on the side of the mass facing the blast. This "sacrificial layer" of aluminum foam would allow for a time wise decrease in the pressure affecting the protected surface, but the foam would blow apart or disintegrate in most cases.

To compensate for the surface disintegration and/or failure another surface plate of solid metal was added. This allowed for, even concentrated, blast loads to be dispersed through the foam material, and therefore allowing for less deformation of the foam and underlying protected structure. [49]

1.6 Modeling and Testing Methods for Energy Absorption

As mentioned before in equation 2, the fluid to cell interaction in foams contributes to their strength and energy absorption ability.

When calculating the energy absorbed to stop a moving object we have to focus on the varying strain rate and the strain at each point between the quickest strain rate point ε_i and the point of the final strain rate, 0, ε_f. If the strain rate decreases linearly then we can say:

$$\dot{\varepsilon} = \frac{\dot{\varepsilon}_i\left(\varepsilon_f - \varepsilon\right)}{\varepsilon_f} \qquad \text{(eq. 39)}$$

The main idea in these equations is that the energy dissipated will increase as the viscosity of the fluid increases, and also as the cell size decreases. [31]

There are two main factors to look at when calculating a foams energy absorption capability; the Janssen (J) factor, and the Cushion factor (which was also refined by Rusch). [49] The J factor is based off of Newtons law;

$$F = ma \_\_\_ or \_\_\_ a = \frac{F}{m} \qquad \text{(eq. 40)}$$

Where F is the force exerted on an object, a is the acceleration or deceleration of that object, and m is the mass of the object. [31]

An ideal foam material will absorb energy at a constant deceleration, a_i, and this can be related to the peak deceleration that the foam causes on the object, a_p. Relating kinetic energy and work done by a constant for a_i can be defined as follows:

$$a_i = \frac{v^2}{2t} \qquad \text{(eq. 41)}$$

Where v is the velocity of the object during deceleration and t is the thickness of the foam. From this the effective energy absorption can be shown in the ratio: [50]

$$J = \frac{a_p}{a_i} \qquad \text{(eq. 42)}$$

This can also be shown when relating the initial and final kinetic energies before and after an impact: [50]

$$\Delta T = \sum \frac{1}{2} m v_f^{\,2} - \sum \frac{1}{2} m v_i^{\,2} \qquad \text{(eq. 43)}$$

The second factor to take into consideration is the Cushion factor. The Cushion factor relates a materials stress-strain characteristic (much data has been collected and recorded for different materials) to its efficiency of energy absorption such as plotting the energy absorbed vs. the applied stress. To get the Cushion factor this plot must be modified by dividing stress by the energy absorbed and putting these values in place of the energy absorbed. [31]

Rusch has added to these methods by introducing an empirical shape factor, ψ(ε), of the stress-strain curve and related it to stress. He also defined a variable K as "…the maximum deceleration produced by an ideal foam divided by that of the foam in question." to account for no foam being ideal. He relates this with the impact energy per unit volume to show a correlation between I, K, σ, and E*.

$$\sigma = E^{*}\psi(\varepsilon)\varepsilon$$
$$K = \frac{a_i}{a_p}$$
$$I = \frac{W}{E^{*}} \qquad \text{(eq. 44-47)}$$
$$\frac{I}{K} = \frac{\sigma}{E^{*}}$$

Where W is the amount of work done on the foam during impact. [51]

1.7 Possible Tests

The main scope of this study is to determine the impact resistance to blast loading of the polyurethane foam plates. Using pressure vs. time and deflection vs. time curves an approximate material dynamic modulus can be determined. The deflection vs. time curves can be found by differentiating acceleration vs. time curves gathered from accelerometers used in the blast load testing. The maximum of these curves will be compared to the maximum deflection of the blast loading test results from optical measurements.

Other tests are needed for comparison of the energy absorption and dynamic modulus of the foam plates. Two tests that can give the impact energy absorption and dynamic modulus characteristics of the foam material at high strain rates are split-Hopkinson pressure bar test and the impact pendulum test. [52, 53, 54] Tests have been preformed with high strain rates with the use of a split-Hopkinson pressure bar apparatus (shown in the figure below) on thermoplastic elastomeric polyurethane foam.

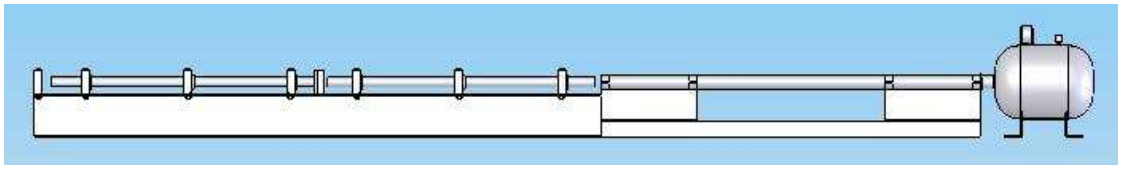

Figure 12: Split-Hopkinson Pressure Bar Apparatus. [30]

A split Hopkinson pressure bar is a device used to get accurate high strain rate data from materials. This data is used to more accurately model explosive and ballistic events. The apparatus consists of a striker bar, an incident bar, and an output bar inside a long straight tube (see the figure below). [54]

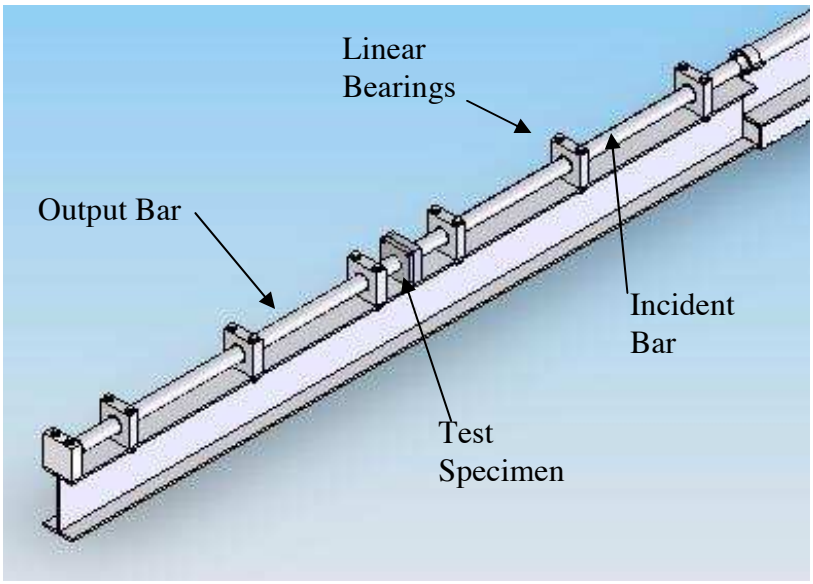

Figure 13: Components of the Split-Hopkinson Bar Apparatus. [30]

The sample is placed between the output and incident bars. The striker is then shot down the tube by compressed gas. When the striker hits the incident bar some of the impact energy is transmitted through the sample to the output bar, and some of the energy is reflected back to through the incident bar. [54]

Two main things need to be taken into consideration when determining the material and length of the input, output, and impact bars as well as the size of the strain gages and sampling rate from the strain gages. The impedance of the bars or sample can be calculated as follows:

$Z = s\rho C_o$ (eq. 48)

Where Z is the impedance, s is the cross sectional area ρ is the material density and C_o is the wave speed in the material. [54]

The impedance mismatch at the interfacial boundaries can be calculated as follows:

$$\alpha_{12} = \frac{2s_1(\rho C_o)_2}{s_1(\rho C_o)_1 + s_2(\rho C_o)_2} \qquad \text{(eq. 49)}$$

where α is the transmission coefficient, which is preferred to be as close to 1 as possible. Minimizing the impedance mismatch will allow for a greater amplitude of transmitted wave. Having higher impedance input and output bars, and lower impedance samples, will reduce the risk of damage to the input and output bars during testing. [54]

For the following, let it be assumed that the impact, input, and output bars are made of the same material. The length of the pulse created by the impact bar can be calculated from:

$$T = \frac{2l_1}{C_o} \qquad \text{(eq. 50)}$$

where l_1 is the impact bar length and T is the impact pulse period. Since the pulse period multiplied by the wave speed gives the pulse length this suggests that the length of the impact pulse is twice the impact bar length. [54]

The strain gage must be placed at the middle of the input bar. This is because the incident pulse must fully pass the strain gage and the strain gage must have ample settling time (1/2 – 1 pulse width) before the wave is again reflected off of the end of the bar back to the strain gage. The wave will reflect back and forth between the ends of the bar. This is why the gage must be at the middle of the input bar. [54]

Since the pulse length is twice the impact bar length, and ample settling time is required for the strain gages, a value of ~4-5 impact bar lengths should be given on either side of the input bar's strain gage. This would require the input bar to be 8-10 times the length of the impact bar. This will allow for a clear reading of the incident and reflected wave histories.

The output bar, on the other hand, can be 2/3 the length of the input bar because only the first transmitted wave time history need be recorded. Instead of being 4-5 times the length of the impact bar, the output bar should be 5.5-6.5 times the length of the impact bar due to a slight slowing in the pulse, and therefore lengthening of the pulse, in the lower impedance sample.

The strain measurements in the output and incident bars give a high strain rate stress vs. strain curve of the material being tested [30]. The stress vs. strain curve

is calculated using the recorded incident, reflected, and transmitted waves in the following equations: [54]

$$\dot{\varepsilon}(t) = -\frac{2C_o}{L}\varepsilon_r(t) \qquad \text{(eq. 51)}$$

&

$$\sigma(t) = \frac{A_o}{A_s}E\varepsilon_t(t) \qquad \text{(eq. 52)}$$

Where $\dot{\varepsilon}(t)$ is the nominal strain rate, C_o is the wave velocity in the incident bar, L is the original length of the specimen, $\varepsilon_r(t)$ is the recorded reflected wave history, $\sigma(t)$ is the nominal stress, A_o is the output bar cross sectional area, A_s is the samples cross sectional area, E is the Young's Modulus of the output bar material, and $\varepsilon_t(t)$ is the transmission wave recorded history. [54, 55, 56]

It was discovered that the transmission wave could be amplified by reducing the input and output bars impedance, and also by using a hollow output bar to reduce the cross sectional area to reduce the impedance mismatch between the sample and output bar. (hollow bar) A cap must be placed on the sample side of the output bar to prevent damage to the bar and sample and to better transmit the impact pulse. [55, 56]

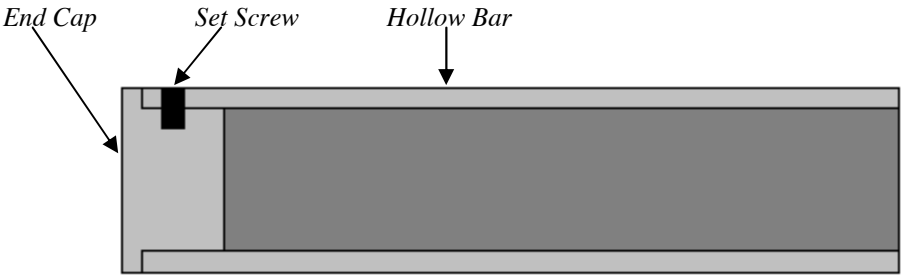

Figure 14: Transmission bar cross section with cap

The strain equation for the sample material must then be modified because the first strain equation assumes that the input and output bars have the same cross sectional area.

$$\varepsilon(t) = \frac{C_o}{L}\left(1 - \frac{A_i}{A_t}\right)\int_0^t \varepsilon_i\,(t)dt - \frac{C_o}{L}\left(1 + \frac{A_i}{A_t}\right)\int_o^t \varepsilon_r\,(t)dt \qquad \text{(eq. 53)}$$

Where A_i is the cross sectional area of the input bar, A_t is the cross sectional area of the output bar, $\varepsilon(t)$ is the sample strain time history, and $\varepsilon_i(t)$ is the recorded incident wave time history. [56]

Another possible test would be the ball rebound test. ASTM standardized tests D 3574-01 are specifically meant for "Flexible Cellular Materials-Slab, Bonded, and Molded". [52, 53] Test H is the ball rebound test which measures the difference between the initial height of a ball dropped onto the foam slab and the rebound

height of the ball. This difference is a way of measuring impact resistance and energy absorption of the foam.

The issues are that the samples are flat and not standing up (as in the blast load testing), there is a back boundary condition from the table below the sample, and the sample is not allowed to displace (as in the blast load testing). ASTM standardized test D 1054-02 is specifically for "Rubber Property-Resilience Using a Goodyear-Healey Rebound Pendulum". [52, 53]

With the use of optics to measure the displacement of the plates, strain gages to measure the strain in the plate, and pressure transducers to measure the pressure the pendulum creates on the face of the plates, this test would meet the needed requirements. The only issue is that the split Hopkinson bar would allow for measurements at greater strain rates. This would better simulate the high strain rates that occur during explosive loading situations. For this reason the Split Hopkinson Bar will be used.

1.8 Air Blasts

When an explosive is detonated in air we can consider the characteristics of an ideal blast wave. "Regardless of the source of the initial finite pressure disturbance, the properties of air as a compressible gas will cause the front of this disturbance to become steeper as it passes through the air ("shocks up") until it exhibits nearly discontinuous increases in pressure, density, and temperature. The resulting shock front moves supersonically,

faster than the speed of sound, in the air ahead of it." [57] The speed of sound in ambient sea level condition air is defined as follows:

$$a = \sqrt{\frac{\gamma p}{\rho}} = \sqrt{\gamma RT} \qquad \text{(eq. 54)}$$

Where a is the speed of sound in air, γ is the specific heat ratio of the gas, p is the pressure of the gas, ρ is the density of the gas, R is the gas constant, and T is the temperature of the gas. [58]

"The air particles are also accelerated by the passage of the shock front, producing a net particle velocity in the direction of travel of the front." [57] In addition, when thinking of this pressure disturbance, we must first make a few assumptions about the explosive being used and air. First,

> *"Assume the explosion occurs in a still, homogenous atmosphere and that the source is spherically symmetric so that the characteristics of the blast wave are functions only of distance from the center of the source (R) and time (t). Let us further assume that an ideal pressure transducer, which offers no resistance to flow behind the shock front and follows perfectly all variations in pressure, records the time history of absolute pressure at some given fixed distance R." [57]*

The time pressure record of such a gauge would look similar like Figure 15.

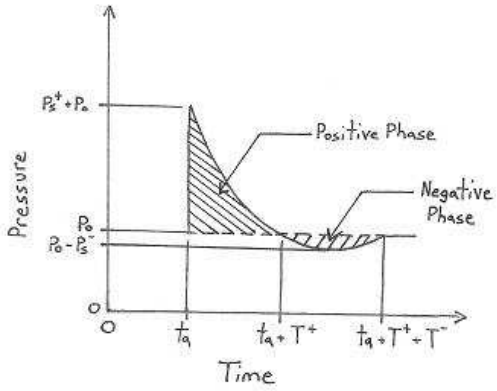

Figure 15: Ideal Blast Wave.

Where the parameters of Figure 15 are:

P_o = Ambient Pressure

$P_s^+ + P_o$ = Peak Pressure

$P_o - P_s^-$ = Peak Partial Vacuum Pressure

t_a = Arrival Time

$t_a + T^+$ = Time when Pressure is between Positive Phase and Negative Phase at P_o

$t_a + T^+ + T^-$ = Time at which Pressure returns to P_o

Also, where the positive impulse of the blast wave is defined by:

$$I = \int_{ta}^{ta+T+} [p(t) - po]\, dt \qquad \text{(eq. 55)}$$

The most significant parameters for use in data reduction of air blasts include peak incident overpressure, peak reflected pressure, arrival time, positive phase duration, distance from charge, incident impulse, and reflected impulse. Vast amounts of data have been collected over the years on air blast parameters from TNT spherical air burst and hemispherical surface bursts and are reported in Reference [59].

Where an explosive is detonated, on or near the ground, can also influence blast waves. A charge detonated on the ground will consist only of the ground reflected wave (Figure 17). This assumption greatly simplifies the calculations and modeling of the blast wave and its effects. These blast waves from large energy sources detonated above, but near, the ground can be considerably modified by certain ground effects such as the reflection off the ground where the fusion of the incident and reflected shock fronts form a third shock front known as a Mach stem, which Figure 15 shows in detail. All of these added shock fronts can complicate the analysis of the wave and its effects. A few other significant variables that come into play are: 1) charge geometry, charge size, and charge confinement, 2) atmospheric conditions, and 3) the effects of after burn due to the oxygen balance of an explosive [60]. All these variables are explained in great detail in References [57], [59], [61], and [62].

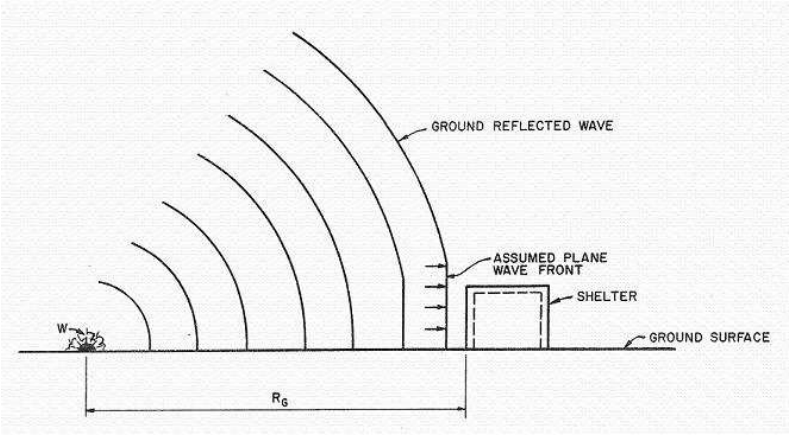

Figure 16: Surface Burst Mach Wave. [63]

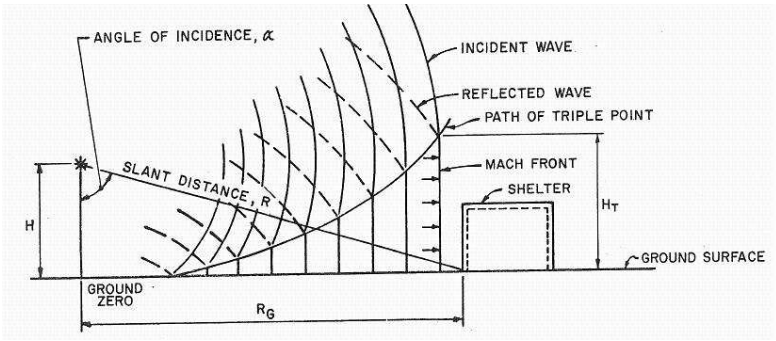

Figure 17: Geometry of Mach Reflection. [63]

Where the parameters of Figure 18 are:

H = Height of Burst

R = Slant Distance

I = Incident Shock Wave

α = Angle of the Incident Shock Wave with Respect to the Horizontal

P_T = Path of Triple Point

M = Mach Wave (Mach Stem), Mach Front

H_T = Height of Triple Point

R_G = Ground Distance to Object

1.8 TNT Equivalency

Traditionally, all explosives have their power output compared to that of TNT because of TNT's long history in military applications and the tremendous body of knowledge relating to its "ideal" explosive properties. This comparison is referred to as "TNT equivalency". TNT equivalency is one of the prime tools utilized to judge the work output of a non-ideal explosive [64]. TNT equivalency is simply defined as the mass of TNT needed to replicate an effect produced by a given explosive, divided by the mass of the explosive tested. An example being, two pounds of explosive "X" was needed to do the work of one pound of TNT, so the TNT equivalency of explosive "X" would be 1 lb / 2 lb = 50% [65]. TNT equivalency is based on explosive energy in various ways. The preferred method of calculation is to use either the hydrodynamic or the thermodynamic work function, as shown in Reference [66]. TNT weight equivalence is defined as:

$$wt(\text{TNT equiv}) = wt(\text{HE}) \times (E_{EXP}(\text{HE}) / E_{EXP}(\text{TNT})) \qquad \text{(eq. 56)}$$

Where,

wt(HE) = Weight of Questioned Explosive

E_{EXP}(HE) = Explosive Energy of Questioned Explosive

E_{EXP}(TNT) = Explosive Energy of TNT

NOTE: Some values for E_{EXP}(HE) / E_{EXP}(TNT) can be found in References 2 and 9.

Other methods for estimating TNT equivalence are based either on correlation, empirical tests, or chemical composition. Some empirical tests include Air Blast, Trauzl, Ballistic Mortar, Sand Crush, and Plate Dent [57, 64]. The values used in the calculations in this report were based off C4 air blast pressure data that was compared to TNT air blast pressure data at the same distances. These comparisons give a first order approximation of the non-ideal explosives TNT equivalencies. One more simplified version of TNT equivalence is reported in Reference [66] as being,

$$\text{TNT equivalent} = D^2 / D^2_{TNT} \tag{57}$$

Where,

D = Detonation Velocity (km/s) of the Explosive in Question

D_{TNT} = Detonation Velocity (km/s) of TNT @ 1.64 g/cm^3 = 6.95 km/s

For C4 this calculation would produce values equal to:

$$\text{C4 (TNT equivalency)} = 8.193^2 / 6.95^2 = 1.39$$

, which is very close to the values given for sea level conditions from 1.18 to 1.70 depending on the exact composition of the C4.

1.9 Impact Dynamics of Circular Plates

A good way of approaching the impulsive loading of a circular plate problem is to start at the blast wave pressure pulse, and pulse duration, on the circular plate face. The impulse *I* is the total force on the face of the plate integrated over time. [55]

$$I = \int p(r,\theta,t)dAdt \qquad \text{(eq. 57)}$$

τ is the pressure pulse duration on the face of the plate. After that time p drops to 0 for mathematical purposes. [67, 68]

Because an impulsive loading situation allows for such a small amount of loading time, approximately zero seconds, the integration terms that come out with time as a variable cannot be used. The impulse must be put into the form of an initial impulse velocity (V_o) giving a no period impulsive load per unit area of the plate ($\hat{I}$).

$$V_o = \frac{\hat{I}}{\rho h} \qquad \text{(eq. 58)}$$

, where ρ is the density of the plate and h is the thickness of the plate. [69]

Equations have been developed and compared [69] to finite element models with almost exact results for sandwich plate composite structures.

$$\frac{\delta_{\max}}{R} = \left(V_o \sqrt{\frac{\rho}{\sigma_y}} + 0.84 \sqrt{\frac{\sigma_Y}{E}} - 0.03 \right) \left[1 - 8.3 \frac{h}{R} + 25 \left(\frac{h}{R} \right)^2 \right] \qquad \text{(eq. 59)}$$

R is the radius of the plate σ_y is the yield stress of the plate material , and E is the plates Young's modulus. [69]

Now to look at the equations used to describe a circular plate loaded impulsively in "Structural Impact" by Norman Jones.

$$M_o = \frac{\sigma_o H^2}{4} \qquad \text{(eq. 60)}$$

Where M_o is the fully plastic bending moment of the plate per unit length, σ_o is the uniaxial yield stress, and H is the plate thickness. p_o (impulsive loading pressure) and p_c (plastic collapse pressure determine which equations to use for a circular plate (dynamic or impulsively loaded). When po/pc >>1 impulsive loading equations are used. [70]

For simple supports:

$$p_c = \frac{6M_o}{R^2} \qquad \text{(eq. 61)}$$

$$\frac{W_f}{H} \cong \frac{\lambda}{8}$$

Where

(eq. 62-63)

$$\lambda = \frac{\mu V_o^2 R^2}{M_o H}$$

, where λ is the dimensionless initial kinetic energy from the impulsive loading, V_o is the impact velocity of the impulsive loading, μ is the density per unit area of the face being impulsively loaded, R is the outer radius of the face, and W_f is the maximum final displacement of the center of the sample. [70]

For clamped supports:

$$p_c \cong \frac{11.26 M_o}{R^2}$$

$$\frac{W_f}{H} \cong \frac{0.84\lambda}{12}$$

Where

(eq. 64-66)

$$\lambda = \frac{\mu V_o^2 R^2}{M_o H}$$

Elasticity of the material also has to be taken into consideration with these general definitions. [70]

Another factor that must be taken into consideration is the blast wave "wrap around" that occurs as the shock wave passes the target. A shock wave passing a target causes pressure not only on the front face of the object but also along the sides, top, and rear. Peak pressures occur at the times shown in the equations below.

$$p_s = [p + C_d q]; t = \frac{L}{2\bar{u}}$$
$$p_r = [p + C_d q]; t = \frac{(L + 45)}{\bar{u}} \qquad \text{(eq. 67-68)}$$

Where p_s is the side and top pressure, p is the front face pressure, C_d is the drag coefficient, q is the dynamic pressure, L is the length of the sides of the structure, and u is the velocity of the shockwave. [71, 65]

2. Methodology

2.1 Sample Construction

The main objective of this testing was to compare the properties of different shapes of Poron® foam with and without water introduced into the foam's pores during explosive loading. We were hoping to find that a foam sample with a domed shape and filled with water would perform better under an explosive load. We theorized at the beginning of this project that the flat fluid filled samples would have the least amount of deflection during the testing because of the limited surface area and the added mass, but that the

fluid filled domed shaped sample would take the highest explosive load before failure because of the added surface area and mass.

Before the explosive testing or Split Hopkinson Bar testing could be completed the samples had to be constructed. Four different sets of samples of the same black polymer based Poron® foam were constructed for the explosive testing. The four samples constructed were: 1) dry and flat with the faces coated with Lexel, 2) filled with water, flat, and coated with Lexel, 3) dry and dome shaped with the faces coated with Lexel, and 4) filled with water, dome shaped, and coated with Lexel.

The foam used in the samples was a ½ in thick and 8 in square black Poron® Quick Recovery Polyurethane Foam (Figure 18).

Figure 18: Sheet of ½ in Poron® Quick Recovery Polyurethane Foam

As mentioned before, this foam displays a 4-8 psi compression at 25% deflection. It has a density of 15 lb/ft^3, a minimum tensile strength of 40 psi at 0.2 in/min strain rate, and a useful temperature range of -40°F to 250°F. [30]

Lexel is a type of caulk/glue that was spreadable, adhesive, and stretchy enough after setting (~25% stretch) to be used in this experiment. Lexel also bonds to plastics and will even bond if the material is wet, which was useful for our application (Figure 19). Another added bonus is that Lexel dries clear so that the foam sealed in the Lexel can be observed. One downside to the Lexel is that it takes 30 minutes to become tack free, cures firm in 2-4 days, and it only fully cures after 1-2 weeks.

Figure 19: Lexel

8in square, ½in thick polyurethane rings, with a 6 ¼ in hole in the middle (Figure 21) were manufactured by the machine shop in Workman Hall on campus.

Figure 20: Polyurethane Ring

These rings were used as a mounting and reinforcement for the different samples during testing. The foam left exposed in the open space of the ring was the portion of the sample that underwent the testing. (Figure 21).

Figure 21: Flat Sample

The 8 in square foam piece was placed on a table and the top face was then coated with a thin layer of Lexel. The Lexel became tack-free in 30 minutes and cured firm in 2 days. After waiting the 2 days a thin sheet of plastic was put on the table and coated with chalk to ensure that the Lexel from the top side of the foam would not bond with the plastic sheet. The sample was then turned over with the Lexel coated side on the chalk covered plastic sheet. The bottom side of the foam was then coated with Lexel and the polyurethane ring was then placed on top of freshly coated Lexel side. This was done so that there would not have to be the separate step of gluing the ring to the sample after the Lexel dried 2 days later, saving time in the process. With 2 days cure time the samples were ready to test.

The wet flat sample (Figure 21) was a bit more complicated to fabricate. Each wet sample was weighed before they were filled with water. Pablo Garibay and Holly Chamberlin, undergraduates in the Mechanical Engineering Department at NMT, devised a process to evacuate the air out of the pores in the foam and fill them with water. The method they devised is approximately 80% efficient, meaning that 80% of the space previously occupied by air in the sample will now be occupied by water. A large aluminum pan (Figure 23) was filled with approximately 4 in of water.

Figure 22: Aluminum Pan

A ¼ in thick, 10in square piece of steel was then laid in the water with a same sized piece of plastic sheet on top. The foam was then placed on top of the plastic sheet. An approximately 100 lb steel cylinder (Figure 23) was then placed on the foam.

Figure 23: Steel Cylinder

This cylinder was rolled back and forth over the foam sample to remove the air from the sample and fill it with water. After the foam was rolled over approximately 20 times with the cylinder it was removed and weighed to compare its wet weight to its dry weight. Each sample gained about 2 ½ times its original weight after being filled. The foam was porous enough that water could be put inside it but the pores were also small enough to keep the water from flowing out at a high rate after the water was inside the foam and the foam was removed from the pan.

The sample was then placed on a sheet of plastic and patted dry around the top and edges with paper towels. The samples never fully dried on the outside, but they dried enough for the Lexel to bond to and seal the sample. Lexel was then spread on the top and sides of the sample. A thicker bead of Lexel was used along the edges of the samples to ensure that the sides were sealed. The samples were then left for 3 days while the Lexel cured. It was decided that the wet samples should cure a day longer than the dry samples due to the possible lengthening effect of the present water on the Lexels cure time.

The samples Lexel seals were then examined. Samples that appeared to need added sealing were touched up during initial 3 day cure time and allowed to cure for an additional 2 days. The sealed samples were then turned over and the plastic sheet was cut off leaving as much of the Lexel side seals intact as possible. The last side of the samples was then sealed with Lexel (Figure 24) and the polyurethane ring was placed on top.

Figure 24: Fully Sealed Wet Sample

This was once again done to combine the last stage of sealing the sample and gluing the ring to the sample into the same step to save time. With 3 days of cure time the samples were ready to test.

The curved dry samples were first sealed flat like the flat dry samples. Creating and holding a dome shape in the samples without ripping or separating the Lexel seal from the foam was now the problem to over come.

It was decided that the dry samples should be experimented on first to ensure that the wet samples kept their water until the dome creating technique was perfected. A plastic salad mixer with an approximate 7 in diameter hemispherical top was purchased. This top was the best sized dome shape that was found for this application (Figure 25).

Figure 25: Salad Mixer Top

There was an aluminum ring covered in tape and chalk with a 6 ½ in inside diameter that was made by the on campus machine shop that also played a role in this fabrication (Figure 26).

Figure 26: Aluminum Ring

A 7in gear with a 3in inside diameter hole (Figure 27) was also used.

Figure 27: 7in Gear

The aluminum ring, 2 of the plastic mounting rings, the gear, the salad mixer top, 4 clamps, tape, chalk, a hair dryer (Figure 28), and Loctite Power Grab Adhesive (Figure 29) all played a part in the fabrication of the domed samples.

Figure 28: Hair Dryer

Figure 29: Loctite Power Grab

The dome shaped salad mixer lid was placed on the table and covered with chalk dust to ensure that the sample did not stick to the lid. This prevented the Lexel from delaminating from the foam. The aluminum ring and the gear were used to prevent the brittle plastic rings from breaking due to bending during clamping. Clamping was

needed to ensure that the sample stay in shape while the adhesive cured. The aluminum ring was covered with a tape and chalk dust to prevent sticking to the Lexel during clamping. The aluminum ring was then placed on the dome shaped lid. The first plastic mounting ring was used to mount the foam to its bottom side with the Loctite Power Grab.

The gear and second plastic ring were not placed on top of the first plastic ring during the first trial fabrication. This resulted in the ring breaking in half during the clamping process. Once this was observed it was decided that a rigid ring was also needed for the top, in addition to the aluminum ring on the bottom, of the sample during clamping to ensure that the rings did not bend to failure. The second plastic ring was incorporated to make sure there was enough room between the foam and the gear to create a dome shape.

Once this assembly was laid together like a sandwich one person pushed down on the sample to create the dome shape from the salad mixer top below. The other person then clamped the aluminum ring and gear on opposite edges of the sample. This ensured that the adhesive would set before the sample moved.

While allowed to sit on top of the salad mixer, the foam was heated with a hair dryer to soften the material enough to get even more of the desired dome shape. Once the sample was heated it was allowed to sit on the mixer top clamped over night and cool to room temperature (Figure 30).

Figure 30: Setup to Manufacture a Dome Shape in the Foam

This allowed the foam to stretch enough and cool enough from the heat forming to keep its shape. The next day the sample was unclamped and set aside (Figure 31) to make room for more sample fabrication.

Figure 31: Dry Dome Shaped Sample After Fabrication

Before the fabrication of this sample, a ¼ in sample of dry foam was experimented on by heating while in the dome shape to see if it would keep its form after it was unloaded and allowed to cool. It kept its shape for approximately 3 weeks, so it seemed that heating to shape was a good tactic.

The curved wet samples were first sealed flat like the flat wet samples. They were also formed into shape the same way the dry dome shaped samples were formed. There was, however, a problem encountered during this forming. When the sealed wet samples were pushed onto the dome and clamped between the gear and the aluminum ring some of the

water inside of the samples was pushed out at a slow drip-like rate through small gaps in the Lexel that were overlooked when the samples were first sealed.

The samples that lost water had to be submerged in water for 2 days to regain there water weight and then carefully gone over with Lexel to seal up any noticeable gaps in the original Lexel seal. The samples then had to cure for another 2-3 days. Once all of this was done the samples were once again ready to shape into form. Once formed, the dome shaped wet samples posed another problem. They would only keep there dome shape for a short amount of time; approximately ½ hour (Figure 32).

Figure 32: Wet Dome Shaped Sample After Fabrication

It was theorized that this was due to the added water weight of the foam and a possible softening effect that the water may have on the foam. If the sample lost its shape it would have to be formed again and let to sit over night. This had to be done the night before testing to ensure that the sample would hold its shape, and the sample was taken out of the forming setup as close to testing as possible. To manufacture all 4 samples took about 2 weeks due to cure time of the Lexel and adhesive, and the time required to get the desired dome shape out of the samples.

The samples for the Split Hopkinson Bar tests were constructed in the same fashion. The differences were that the samples were 3/16 inch thick samples that were 1.25 inches by 1.25 inches. Also, since no doming of the samples was possible, all of the samples were flat.

2.2 Sample Water Absorption

The data sheet for the polyurethane foam that was used stated that the sheets of foam had a density of 15 lb/ft^3 ~ 240.28 kg/m^3. Each sample for the EMRTC testing was ½ in thick and 8in by 8 in square ~ 0.000524 m^3. This should have given the dry samples a mass of ~ 126 g. Water has a density of 1000 kg/m^3. The sample material was previously determined to be 80% porous by Pablo Garibay and Holly Chamberlin. Therefore the wet samples, if fully saturated with water, should have had a mass of approximately 545 g. This was calculated using the equation to determine the volume fraction of the pores:

$$\phi_v = \frac{m_{total} - m_{foam} / \rho_{fluid}}{V_{foam}} \qquad \text{(eq. 69) [72]}$$

The mass of the samples with and without the introduction of water are listed in Table 1:

Sample #	**Mass (g) Dry**	**Mass (g) Saturated With Water**	**% Void Volume Filled for 80% Porosity**	**% Void Volume Filled with Air For 80% Porosity**

1 Dry	131	NA	NA	NA
2 Dry	139	NA	NA	NA
3 Wet	136	346	52.5	47.5
4 Wet	128	352	53.9	46.1

Table 1: Volume of Pores Filled in Sample Foam

If the pores were mostly saturated with water I would assume that the foam had an approximate porosity of 50%. This discrepancy was due to using cold instead of hot water during the fluid filling process. The warmer water would have opened the pores more and allowed more water to fill the voids. The cold water actually closed off the pores more and allowed less water into the samples.

Additional experiments were done with hot water to determine if the temperature of the water used was a factor. These experiments were done in the current year.

Sample #	**Mass (g) Dry**	**Mass (g) With Water**	**% Void Volume Filled with Water**	**% Void Volume Filled with Air**
1 Wet	130	437	79.5	20.5
2 Wet	128	443	80.8	19.2
3 Wet	124	427	78.5	21.5
4 Wet	135	401	72.3	27.7

Table 2: Volume of Pores Filled in Sample Foam

It can be clearly seen from the table that the higher temperature water had a significant effect on the amount of water that the samples absorbed.

This method of filling the samples was utilized in the making of the samples for the Split Hopkinson Bar testing. The samples water absorbance are shown in the table below.

Sample	Mass Dry (g)	Mass With Water (g)	% Void Filled With Water
1	1	7	81
2	1	7	81
3	1	6.5	75
4	1	7	81
5	1	6.5	75
6	1	7	81
7	1	7	81
8	1	6.5	75
9	1	7	81
10	1	6.5	75

Table 3: Split Hopkinson Bar Wet Samples %Void Filled With Water

2.3 Testing Procedures

2.3.1 EMRTC Test Description

The table below lists the samples tested at EMRTC and the standoff distances that the samples were subject to.

Test #	Sample	Distance
1	Flat (dry and wet)	45
2	Flat (dry and wet)	35
3	Flat (dry and wet)	25
4	Domed (dry and wet)	45
5	Domed (dry and wet)	25
6	Domed (dry and wet)	15

Table 4: EMRTC Tests, Samples, and Standoff Distances

2.3.2 Blast Testing Instrumentation

Pressure and impulse data was collected from all 6 tests by means of PCB™ piezoelectric transducers and a corresponding PCB™ 855 gauge power amplifier. The amplifier used managed the reflected pressure measurements for each experiment. Reflected pressure gauges were mounted in the stand, at locations shown in Figure 33.

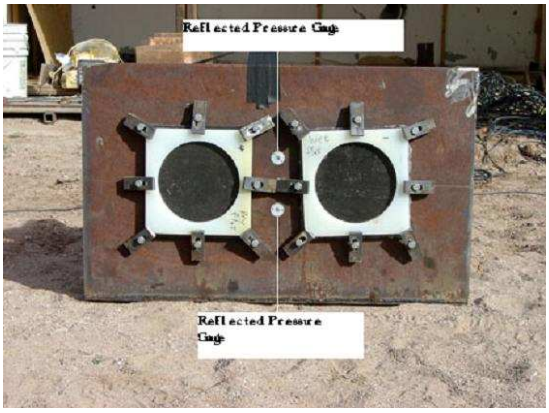

Figure 33: Placement of Reflected Pressure Gauges on Stand.

Accelerometers were attached to the back of the samples (Figure 34).

Figure 34: Attached Accelerometer

Phantom high speed cameras (Figure 35) on either side of the test set up were also used to measure the displacement of the samples and to have data to compare to the accelerometer data.

Figure 35: Phantom High Speed Cameras on Either Side of the Test Stand

This was done to determine the validity of the accelerometer data. 1 in lines were drawn onto toothpicks glued next to the accelerometers (Figure 36). This mark was made as a reference point to determine the displacement of the samples during testing from the phantom high speed cameras.

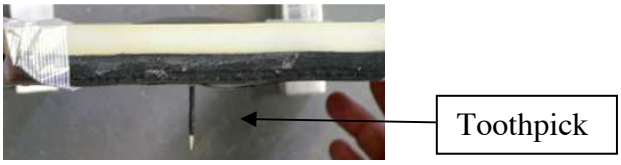

Figure 36: Toothpick Mark

The wet samples were placed in the south opening of the test stand and the dry samples were placed in the north opening of the stand to keep track of sample data (Figure 37).

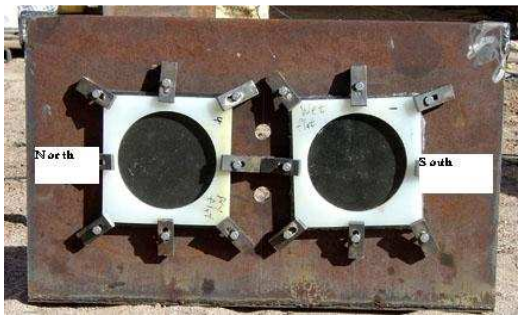

Figure 37: North and South of Test Stand

6 tests were conducted. The flat dry and flat wet samples were hit with a blast wave from a 1 lb hemispherical charge of C-4 set at 45, 35, and 25 ft.

Figure 38: Separated Accelerometer Flat 35 ft Test

The dome shaped dry and wet samples were also hit with a blast from a 1 lb hemispherical charge of C-4, but the distances changed to 45, 25, and 15 ft to push the limits of the accelerometers delaminating from the samples. The accelerometer slightly delaminated from the wet dome shaped sample during the 25 ft test. This may have led to some error in the data. Both accelerometers separated from the samples during the 15

ft test (Figure 39) showing a need for better adhesion to the samples in the future if close blast tests are to be performed.

Figure 39: Separated Accelerometers Domed 15 ft Test

2.3.3 EMRTC Data Reduction

EMRTC's raw data were reduced using DPlot software. The pressure traces were used to determine the peak pressures and were integrated to find the positive phase peak impulses. The acceleration traces were used to determine the peak accelerations in the positive direction (blast direction), and they were double-integrated to generate the maximum positive displacements. The maximum positive displacements were also collected from the Phantom 7 software and are reported in the results section of this document. Figure 40 shows an example of the EMRTC data plot for reflected pressure, impulse, and displacement.

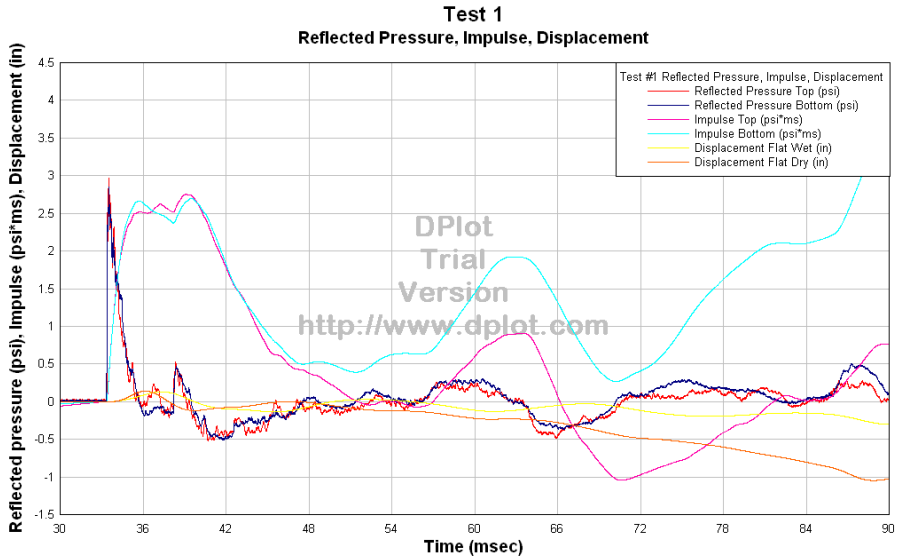

Figure 40: Reflected Pressure, Impulse, Displacement vs. Time Plot

Figure 41 shows an example of the EMRTC data plot for acceleration.

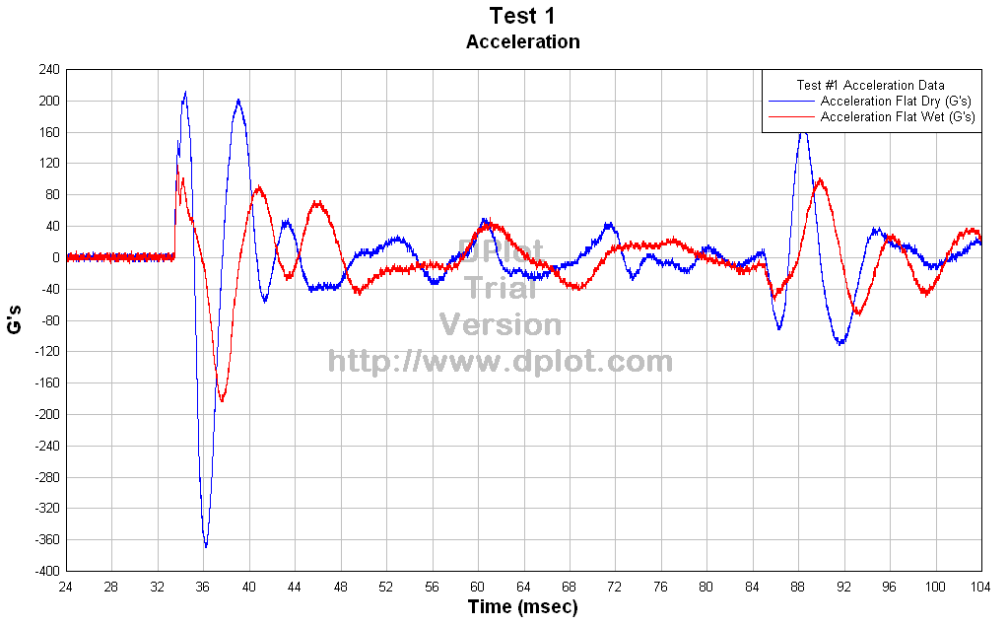

Figure 41: EMRTC Acceleration Data

2.3.4 Split Hopkinson Bar Testing Procedures

Figure 42: Split Hopkinson Bar in Built Room Iris Passcal Warehouse

In order to validate the air-blast test observations using AUTODYN, Split-Hopkinson Pressure Bar tests were performed to determine the dynamic modulus at various strain rates.

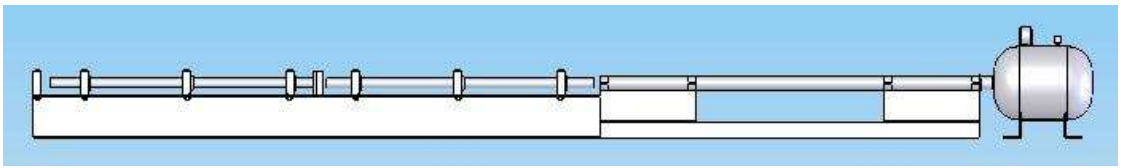

Figure 43: Split-Hopkinson Pressure Bar Apparatus as Modeled in SolidWorks.

A split Hopkinson pressure bar is a device used to get accurate high strain rate data from materials. This data is used to more accurately model explosive and ballistic events. The apparatus consists of a striker bar, an incident bar, and an output bar (refer to figures x-y below).

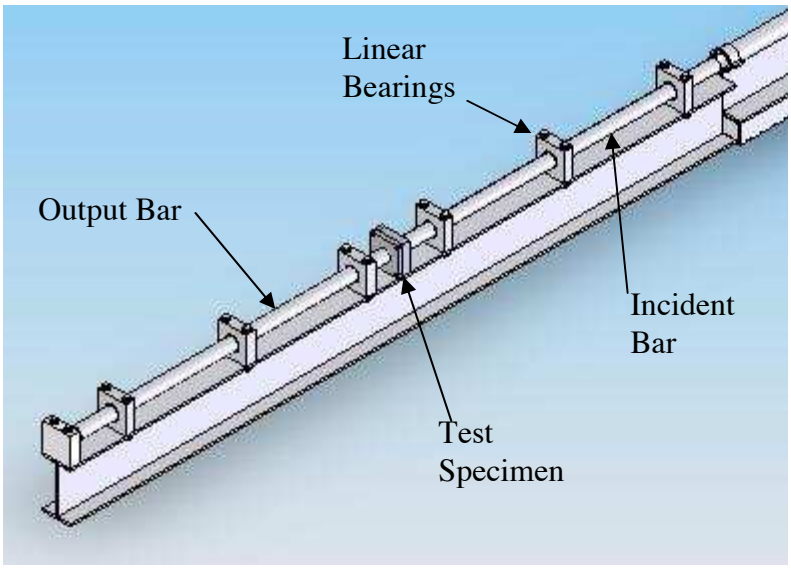

Figure 44: Wave Analysis Portion of the Split-Hopkinson Bar Apparatus.

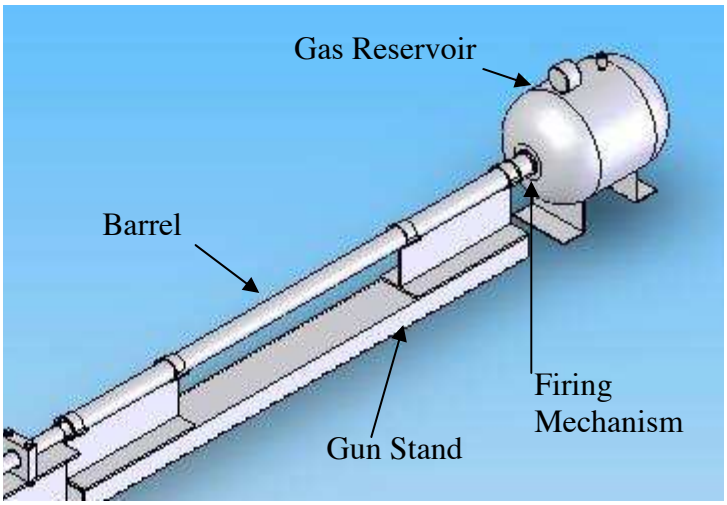

Figure 45: Air Gun Portion of the Split-Hopkinson Bar Apparatus.

The sample is placed between the output and incident bars. The striker is then shot down the barrel by compressed gas. When the striker hits the incident bar the impact energy is sent through the incident bar and transmitted through the sample to the output bar, and some of the energy is reflected back to the incident bar. The strain measurements in the

output and incident bars give a high strain rate stress-strain curve of the material being tested. This data is gathered with the use of strain gages placed on both the incident and output bars.

Testing elastic/visco-elastic materials with this method has been quite a challenge. The issue is that the bars need to be rigid in order to limit deflection and damage during testing. Commonly hardened steel, or other metal, rods have been used for this purpose. Materials such as foams have very low impedance when compared to metal bars. This impedance mismatch between the materials can greatly reduce the amount of wave transmitted into and through the sample being tested.

A few ideas have been thought of and tested to take care of the mismatch problem. One idea, from Dr. Chen at Purdue University and Dr. Frew from Sandia National Laboratories was to use polymer or aluminum instead of steel rods to lower the impedance of the bars. This is implemented in the current test. This led to another idea. That idea (which was implemented in the current test) was to use a hollow output bar with a cap fitted at the sample end to further lower the impedance. A non-dispersive ramp pulse from the impact bar is required to precisely control the profile of the incident pulse so that the specimen deforms at a nearly constant strain rate under a dynamically equilibrated stress. This should be true through large to even small strains. [54, 55, 56]

2.3.5 The Split Hopkinson Bar Apparatus

An adjustable, up to 200 psi, compressor is used to provide the air pressure to the gas gun and actuated ball valve portion of the apparatus (Shown below). It is a DeWALT Heavy-Duty 200 PSI Electric Wheeled Portable 1.8 Hp Compressor with a 4.5 gallon tank.

Figure 46: DeWALT 200 psi compressor.

This adjustment allows for different velocities of the striker bar and different incident wave amplitudes in the incident bar.

A 4.5 gallon reservoir, with a pressure gage, is used to store the compressed air before the air actuated ball valve is opened to drive the striker bar down the 4 ft barrel (See figure below).

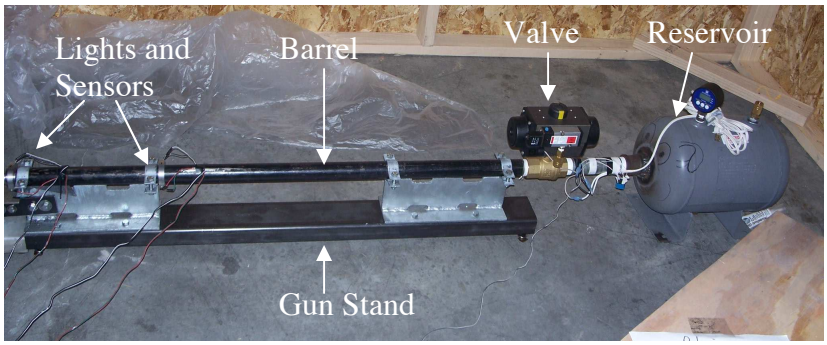

Figure 47: Reservoir, actuated ball valve, and barrel portion of the Split Hopkinson Bar.

A pressure transducer is attached to the 4 gallon reservoir tank to take pressure data during testing. The pressure sensor was tested to check for linearity.

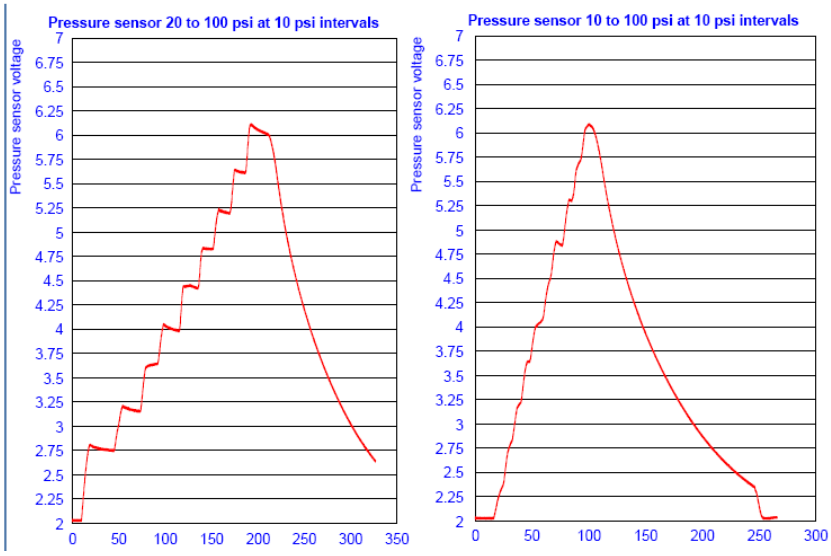

5 Second Delay 0.5 Second Delay

Figure 48: Pressure Sensor Testing Results

The gun stand and the stand that holds the incident and output bars are bolted together to prevent the striker bar from completely exiting the barrel after hitting the incident bar.

There are two bright white LED's and two SFH 314 light sensors across from each other 1 ft apart towards the end of the barrel to estimate the exit velocity of the striker bar. This helps to adjust the amplitude of the incident wave. The higher the velocity of the striker bar, the larger the amplitude of the impact pulse.

The incident and output bars, each 4 ft long, are attached to a 9 ft aluminum I-beam, each with 3 mounting blocks with oil infused bushings to help reduce friction and allow the bars to move as freely in the axial direction as possible (See Below). The incident bar is a solid aluminum rod.

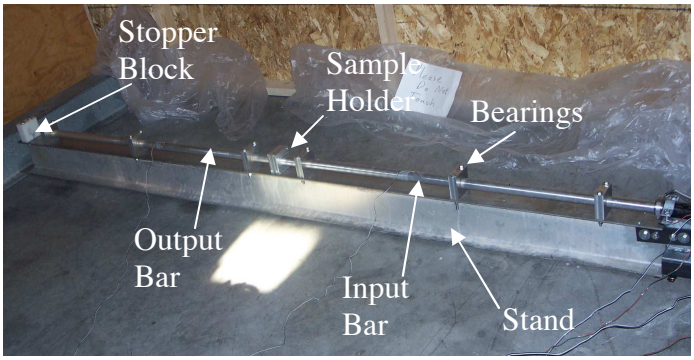

Figure 49: Incident bar, sample holder, and output bar of the Split Hopkinson Bar.

Aluminum was used because of the low impedance material being tested. When testing other materials it is preferred that a material slightly harder but close to the same impedance be used to get the best results. The idea is to use a material that can take a beating from the projectile over several tests while limiting the impedance mismatch between the sample and the bars. A Vishay ¼ in 120 ohm uniaxial strain gage was

attached to the center of the 4 ft input bar. Another was attached 4 inches from the sample end on the output bar.

Figure 50: Vishay ¼ in 120 Uniaxial Strain Gage (Broken Solder Connections)

Normally there is no need for a sample holder between the two bars. The standard method of mounting the sample is to place a small amount of lubricant on either side of the sample and press the two bars against its sides. This normally holds the sample in place. A sample holder was experimented with due to fluids being present in some of the samples.

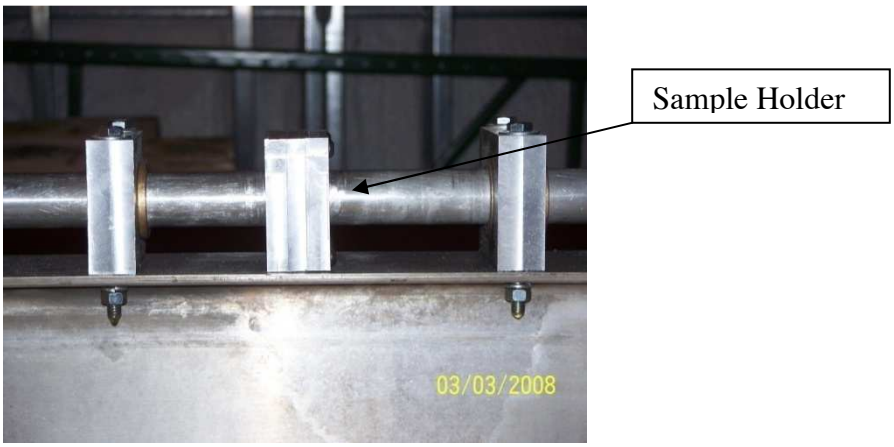

Figure 51: Sample Holder

At the end of the apparatus there is a 2 in thick block of Teflon bolted to the I-beam. Teflon has been used to limit the damage to the output bar during testing. An additional 4 inches of polyurethane foam was needed in front of the stopper plate to reduce the amplitude and rise time of the stopping impact pulse.

The apparatus is controlled through the use of a National Instruments SCXI module that plugs in through a USB port. This module is then controlled by LabView 8.2. The instrumentation is LabView programming in conjunction with a National Instruments SCXI-1600 USB chassis with three different modules (SCXI-1100, 1520, and 1124) and three different terminal blocks (SCXI-1300, 1314, 1325) (Seen Below).

Figure 52: SCXI-1600 with modules and terminal blocks.

The accuracy of this instrumentation was checked by the use of a Vishay P3 Strain Indicator and Recorder (Shown Below).

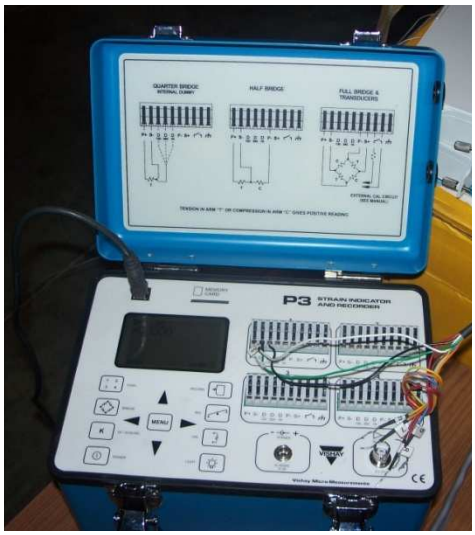

Figure 53: Vishay P3 Strain Indicator and Recorder

2.3.6 Strain Gage Set Up

There are two wires, black and white, coming from the strain gages. The white wire splits into two red wires towards the end. This is to reduce the amount of noise from the strain gage during operation. The two red wires and the black wire were hooked up to the SCXI-1314 terminal block as shown in the quarter bridge configuration in the SCXI-1520 users manual.

The two channels that were chosen for the strain gages were written down and later entered into the LabView program. The strain gages have resistances. This resistance was made to be the same as the resistors next to the channels chosen in the SCXI-1314 terminal block. These resistors were replaced with the correct high accuracy resistors.

The SCXI-1314 terminal block was attached later to the SCXI-1520 module. This was the last terminal block attached the SCXI Modules in the SCXI 1600 chassis to allow for

as much slack in the strain gage wires as possible to prevent possible detachment during testing.

2.3.7 Light Sensors Set Up

On the barrel of the gas gun are holders for the light sensors and bright LED's as shown below.

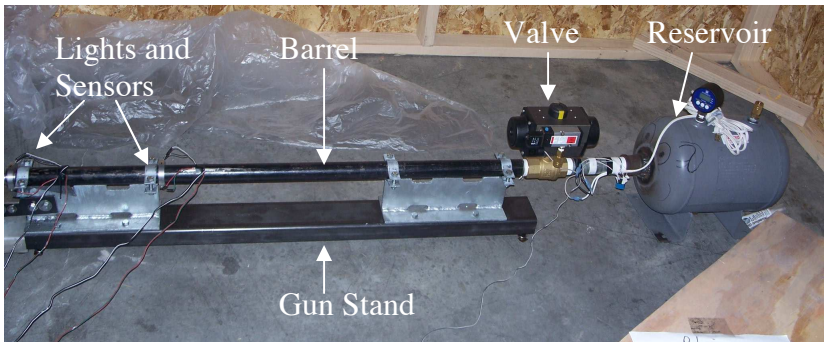

Figure 54: Reservoir, actuated ball valve, and barrel portion of the Split Hopkinson Bar.

The wires to the light sensors were labeled with + and GRND labels as well as which light sensor they are attached to. Light sensor 1 is the first light sensor that the projectile will pass as it travels down the barrel to impact the input bar.

Two channels were chosen in the SCXI-1300 terminal block for the light sensors. Approximately 1 ft wires were attached to the Vin and GRND's of these channels. The wires were then be labeled and written down so that they could later be entered into the LabView program.

Two channels were chosen in the SCXI-1300 terminal block for the +10V, -10V, and GRND required for the signal amplification circuitry shown in the figure below. These channels were written down and the wires were labeled.

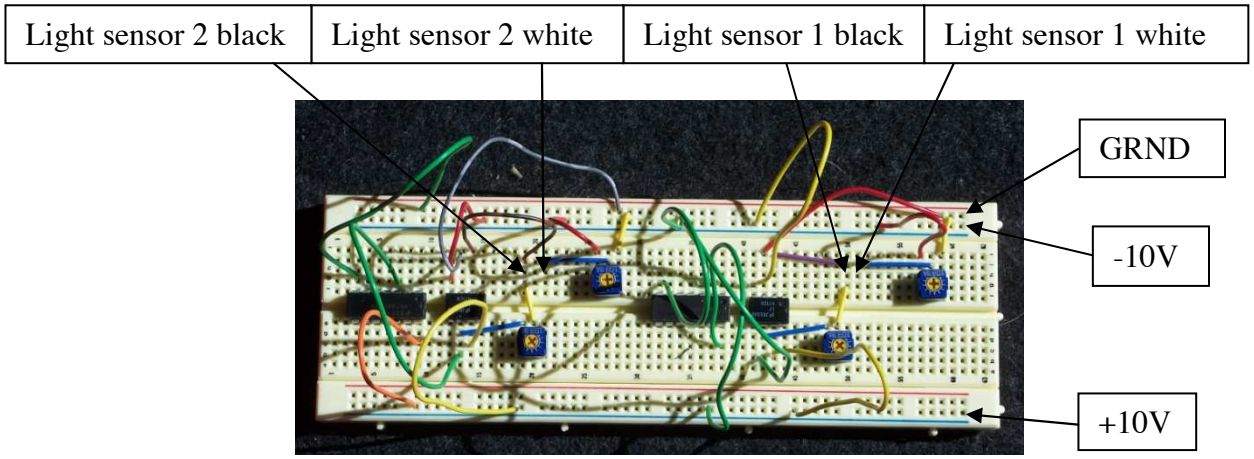

Figure 55: Signal amplification circuitry for the light sensors.

The wires for the light sensors, +10V, -10V, and GRND were hooked up to the signal amplification circuitry as shown in the figure above once the SCXI-1300 and SCXI-1325 terminal blocks were attached to the SCXI-1100 and SCXI-1124 modules respectively. This was done once the pressure sensor was hooked up.

2.3.8 LEDs Set Up

On the barrel of the gas gun was two holders for the light sensors and bright LED's as shown in figure 54.

The wires to the LEDs were labeled with + and GRND labels as well as which LED they are attached to. LED 1 is the first light sensor that the projectile will pass as it travels down the barrel to impact the input bar.

Two channels were chosen in the SCXI-1325 terminal block for the light sensors. These channels were written down so that they could later be entered into the LabView program.

2.3.9 Relay Set Up

Under the actuated ball valve and just towards the reservoir of the gas gun was a relay as shown below.

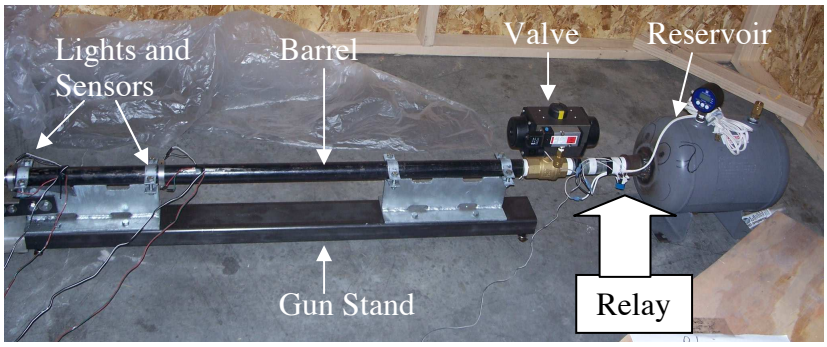

Figure 56: Relay, actuated ball valve, and barrel portion of the Split Hopkinson Bar.

The wires to the relay were labeled with + and GRND labels. A channel was chosen in the SCXI-1325 terminal block for the relay. This channel was written down so that it could later be entered into the LabView program. The AC plug of the relay was plugged

into an AC outlet when all of the other sensory components such as the pressure sensor, LEDs, light sensors, and strain gages were set up and ready for testing.

2.3.10 Pressure Sensor Set Up

Figure 57: PB.503 Proto Board

The pressure sensor is on top of the reservoir and has 4 wires coming out of it. The red wire attached to the Vin wire on the pressure sensor and the green wire attached to the resistor and output wire of the pressure sensor were attached to the +15 and GRNDs on the PB.503 Proto Board respectively. A multimeter was used to check that the pressure sensor was receiving 20 Volts once the Proto Board was turned on. The PB.503 Proto Board was turned off until the sensor check was finished.

The red and green wires attached to either side of the resistor were attached to a channel on the SCXI-1300 terminal block. The red wire was hooked up to the Vin and the green wire was hooked up to the GRND. This channel was written down so that it could be entered into LabView later. Once this had been done the SCXI terminal blocks were

hooked up to the SCXI modules. Use the top and bottom screws on the SCXI terminal blocks to secure them into place on the modules.

2.3.11 Compressor Set Up

The compressor, regulator, compressor outputs, and the hose output valves are shown in the figure below.

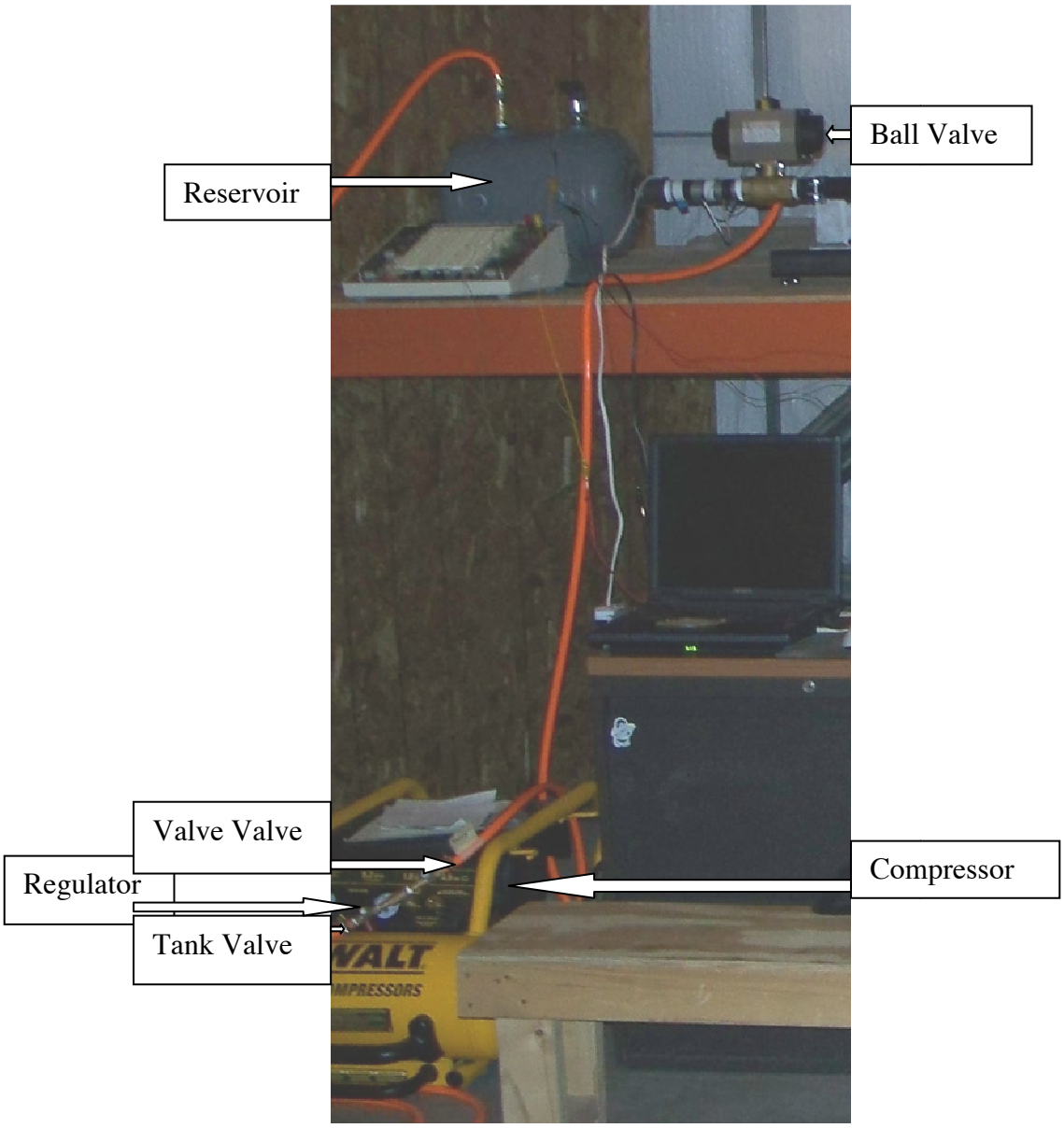

Figure 58: Compressor, regulator, compressor outputs, and the hose output valves.

Before turning the compressor on the regulator was turned counterclockwise until it stopped and the hose output valves were set to the closed (handle not pointed inline with the hose) position. This set the regulator to put out 0 psi and kept air from flowing through the hoses to the reservoir or the actuated ball valve. The compressor was then turned on.

The hose labeled valve was attached to the air hose inlet under the actuated ball valve closest to the reservoir. The hose labeled tank was attached to the hose inlet on top of the reservoir. The tee between the valve and tank valves was attached to the hose inlet on the compressor closest to the regulator.

2.3.12 LabView Set Up

Two VI's are needed to be opened up to carry out the strain gage, light senor, LED, relay, and pressure sensor checks as well as the wave capturing, strain gage data, and velocity and pressure data tests. The VI db-peasure-voltage-strain-pressure-try2 and just try strain gages VI's were opened.

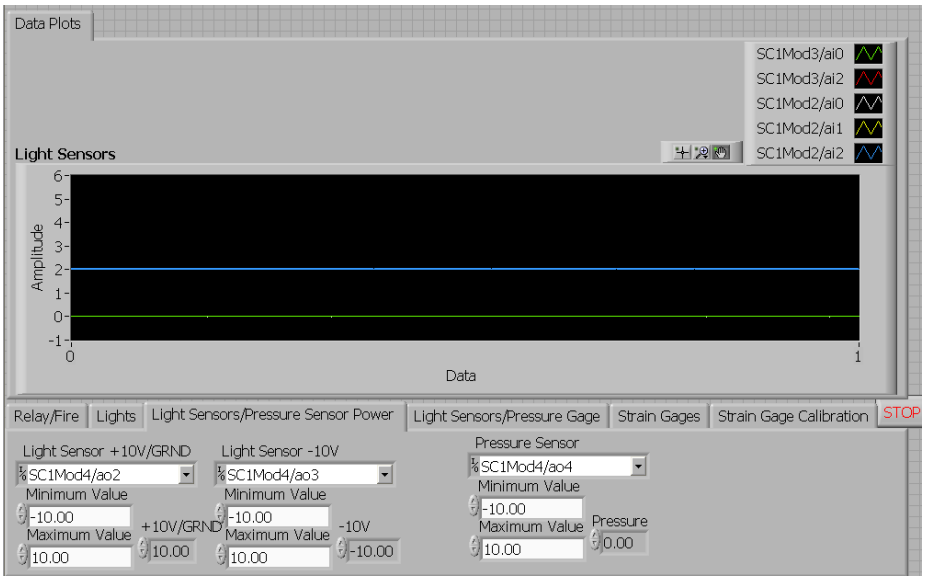

Figure 59: db-peasure-voltage-strain-pressure-try2 VI Front Panel

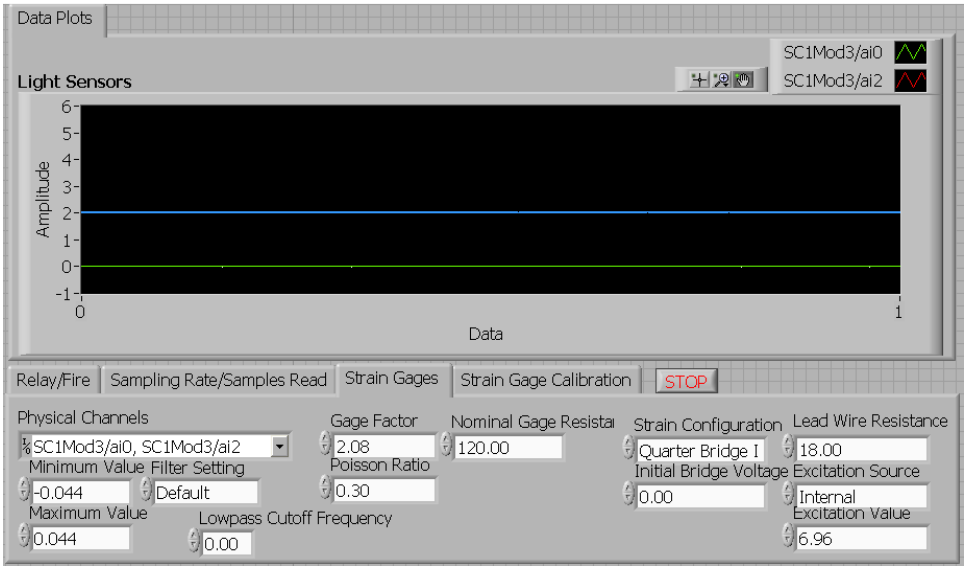

Figure 60: just try strain gages VI Front Panel

To check the strain gages the just try strain gages VI was opened. The relay voltage was set to 0 and the strain null and measure actual excitation buttons were on. The shunt

calibration was not turned on. The sample rate and samples to read were set to 100k. Values in the strain gages tab were calculated by using the SCXI-1520 user manual.

The module and channels for the strain gages were defined. These were found in the measurement and automation explorer. The program was then run. Once the program was running the input and output bars were tapped approximately 4-6 inches from the strain gages with a short aluminum rod. The stop button was then hit. The TDMS viewer then opened up and the data from the strain gages was checked.

2.3.13 Light senor, LED, relay, pressure sensor, and actuated ball valve check

To check the light sensors, LED's, relay, and pressure sensor the db-peasurevoltagestrainpressuretry2 VI was opened. All of the channels were defined. These were found in the measurement and automation explorer. The relay was set to 0 V, the LED's were set to 3.6 V, the pressure sensor voltage was set to 0, and the light sensor channels +10V and -10V were set to the proper voltages.

The program was then run. To check the LED's the LED voltages were set to 0V and then back to 3.6V one at a time and make sure that the LED's responded accordingly by making sure the LED's turn on and off. This was observed at the back of the LED's.

To check the light sensors the LED's were set to 0V and back to 3.6V one at a time to make sure that the light sensor channels responded accordingly.

The relay was checked by turning the relay from 0V to 9V and back while the relay AC connection was plugged in and there was no pressure in the reservoir tank. This was made sure of by opening the bottom valve on the tank. Each time the voltage was changed a slight click was heard from the relay.

The pressure sensor was then checked. It was made sure that the bottom valve on the tank was closed as well as the tank and valve valves on the compressor outlet. It was also made sure that the regulator on the compressor was turned all the way counterclockwise. The compressor was then turned on and allowed to fill until it turned off. Then the tank valve at the compressor was opened and the Proto Board was turned on. The Proto Board output was checked with a multimeter and was giving 20V. The VI was run. Gradually the compressor regulator was turned clockwise until the compressor read 100psi. Next, the compressor regulator was turned counterclockwise until the compressor read 0psi. The TDMS viewer was checked to make sure that the sensor voltage gradually increased and decreased during this procedure. All of the tank and compressor pressure was bled off and all of the valves were closed.

The actuated ball valve was checked by opening the valve valve at the compressor and making sure that the relay AC connection was plugged in. The program was then run. The relay was then set to 9V. Gradually the regulator on the compressor was turned clockwise until the actuated ball valve opened. The relay voltage was then set to 0. The valve then closed. The regulator on the compressor was turned counterclockwise until the compressor read 0. The valve valve on the compressor was then closed.

Figure 61: Air Actuated Ball Valve.

Figure 62: Reservoir, Ball Valve, Proto Board.

2.3.14 Wave capturing, strain gage data

To get the strain gage data from the tests the just try strain gages VI was used. This VI was used because of its ability to sample at a higher sample rate of 100k samples per second. This sample rate was required in order to get a clear picture of the impact, reflected, and transmitted waves. The relay voltage was set to 0 and the strain null and measure actual excitation buttons were on. The shunt calibration was not turned on. The

sample rate and samples to read were set to 100k. Values in the strain gages tab were found by using the SCXI-1520 user manual.

The modules and channels for the strain gages, light sensors, LED's, pressure sensor, and relay were then defined in the VI. These channels were found in the National Instruments Measurement and Automation Explorer program. The regulator on the compressor was set to zero. The valve and tank valves on the compressor were closed, and the valve on the bottom of the reservoir was closed. The reservoir contained 0 psi. To make sure of this the valve on the bottom of the reservoir tank was slowly opened and closed.

Before the program was run the input and output bars were pushed to the stopper plate (the impact absorption foam was moved out of the way).

Figure 63: Impact Absorption Foam.

The valve valve on the compressor was then opened and the regulator was rotated clockwise until the compressor read 80 psi. The program was then run until the strain

null was finished. The ball valve frequently opened and closed briefly as the ball valve reached the needed pressure with the sudden AC burst from the relay as the program started the SCXI chassis. The stop button was then hit. This procedure was done to make sure that the ball valve did not accidentally actuate prematurely.

The hose was then disconnected from the reservoir tank and used the hose to push the impact bar back in the barrel until it touched the ball valve. This was done to act as a safety precaution that disconnected the air pressure from the tank while utilizing the hose to load the impact bar. The wave shaper (a polymer, nylon, ring with two squares of tissue paper all attached by vacuum grease) at the end of the striker bar that would be impacted by the striker bar with vacuum grease.

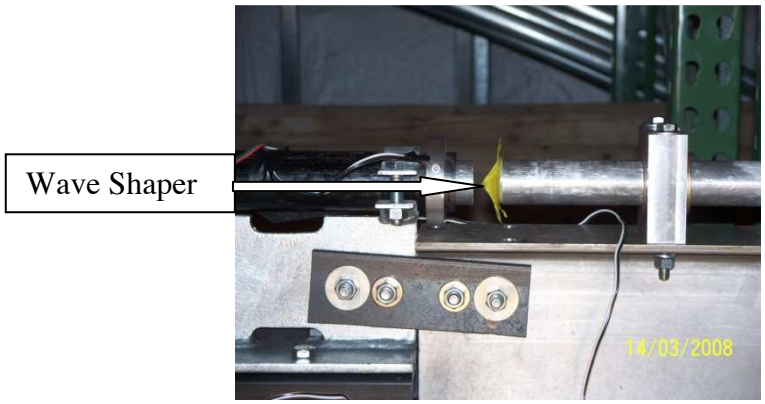

Figure 64: Wave Shaper.

The wave shaper filtered out high frequency noise while slowing the rise time of the pulse enough as to minimize damage to the strain gage solder connections. The input bar was then moved towards the barrel until the wave shaper was at the end of it. The sample

was then placed at the other end of the input bar by gently sliding the output bar towards the input bar until the sample was held in place.

Figure 65: Sample Held in Place.

The impact absorption foam was then placed back between the output bar and the stopper plate without moving the input bar.

The valve valve on the compressor was then closed and the regulator was rotated counterclockwise until the compressor read 0 psi. The tank valve was then opened at the compressor and the regulator was rotated clockwise until the compressor read a constant desired pressure (10-20psi for these tests). Now the relay was set to 9V in the VI.

The VI was then run. Once the program was running the impact bar was fired and the relay voltage was set back to 0, closing the ball valve. The VI was then stopped. The TDMS viewer then opened up and the data was checked. The data from these tests were analyzed in the DIAdem program.

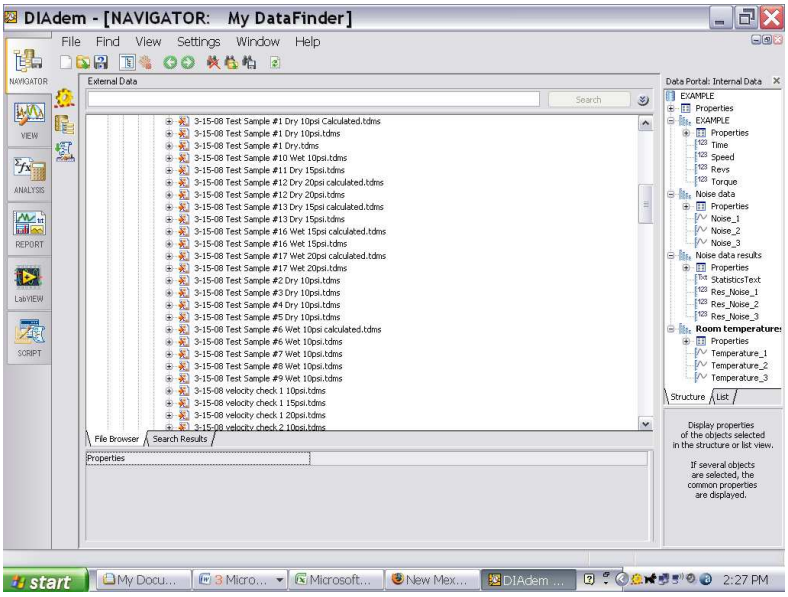

Figure 66: DIAdem Work Space.

2.3.15 Velocity and pressure data

To get the light sensor (velocity) and pressure data from the test the "db-peasurevoltagestrainpressuretry2" VI was used. The strain portion of this VI was ignored as it was previously found that this VI could not sample at the required rate for the strain gage measurements. The relay voltage was set to 0 and the strain null, shunt calibration, and measure actual excitation buttons were off. The sample rate and samples to read were set to 10k.

The modules and channels for the strain gages, light sensors, LED's, pressure sensor, and relay were found in the Measurement and Automation Explorer and put into the LabView VI. The regulator on the compressor was set to zero. The valve and tank valves on the compressor were closed, and the valve on the bottom of the reservoir was closed. The

reservoir had 0 pressure. To make sure of this the valve on the bottom of the reservoir tank was slowly opened and closed.

Before the program was run the input and output bars were pushed to the stopper plate (making sure that the impact absorption foam was out of the way). The valve valve on the compressor was opened and the regulator was rotated clockwise until the compressor read 80 psi. The program was run until the strain null was finished and the ball valve opened and closed. The VI was then stopped.

The hose was disconnected from the reservoir tank and the hose was used to push the impact bar back in the barrel until it touched the ball valve. Dummy wave shapers (usually a ½ inch thick foam square attached by vacuum grease) were then placed at the end of the striker bar that would be impacted by the striker bar with vacuum grease. The input bar was then moved towards the barrel until the wave shaper was at the end of it. The dummy sample (again usually a ½ inch thick foam square) was placed at the other end of the input bar by gently sliding the output bar towards the input bar until the dummy sample was held in place. The impact absorption foam was then again placed between the output bar and the stopper plate without moving the input bar.

The valve valve on the compressor was then closed and the regulator was rotated counterclockwise until the compressor read 0psi. The tank valve at the compressor was opened and the regulator was rotated clockwise until the compressor read a constant desired pressure (10-20 for these tests). Now, the relay was set to 9V in the VI.

The VI was then run. Once the program was running the impact bar was fired and the relay voltage was then set back to 0 closing the ball valve. The VI was then stopped. The TDMS viewer then opened up and the data was checked. The data from these tests was be analyzed in DIAdem.

2.3.16 Different materials considerations

The present Split Hopkinson Bar set up is for testing low impedance materials such as foams, epoxies, and rubbers. To test other materials the impedance between the sample material and the input and output bar materials should be as close as possible.

Another consideration should be finding out the period or length of the impact waves in the input and output bars. This will determine the lengths of the input and output bars. The strain gage must be placed in the middle of the input bar and have enough length of bar on either side to keep the incident and reflected waves from overlapping at the strain gage. This will allow you to see the entire waves. The same consideration must be taken with the output bar, except that you only need to see the first transmitted wave so the strain gage can be placed towards the sample end of the output bar.

Another issue that the wave period brings up is the required sample rate. Once you know the period you want to make sure to get between 5 and 10 samples each wave (the more samples the better).

The rise time of the impact wave can have adverse affects on the strain gage connections so a wave shaper composed of a thin polymer material may be required. The plastic deformation of the wave shaper will slow the rise time and save the strain gage connections. This slow in rise time will affect the period of the wave and therefore the length of the bars and the sampling rate. Also the wave length divided by the gage length should be 100 or greater to better capture the wave.

The papers "Advancements in the Split Hopkinson Bar Test" by Michael Adam Keiser [54] and "A Split Hopkinson Bar Technique for Low-impedance Materials" by W. Chen et al [56] were read to better understand these concepts.

2.4 ANSYS AUTODYN Simulations

The data from the Split Hopkinson Bar tests was used to create computer simulations of the explosive tests done at EMRTC in the program AUTODYN. AUTODYN is a program that is used to simulate impact and explosive loading events. The models created to simulated the EMRTC testing were carried out in a revolved 2D simulation. Examples of the 2D and 2D revolved models can be seen below.

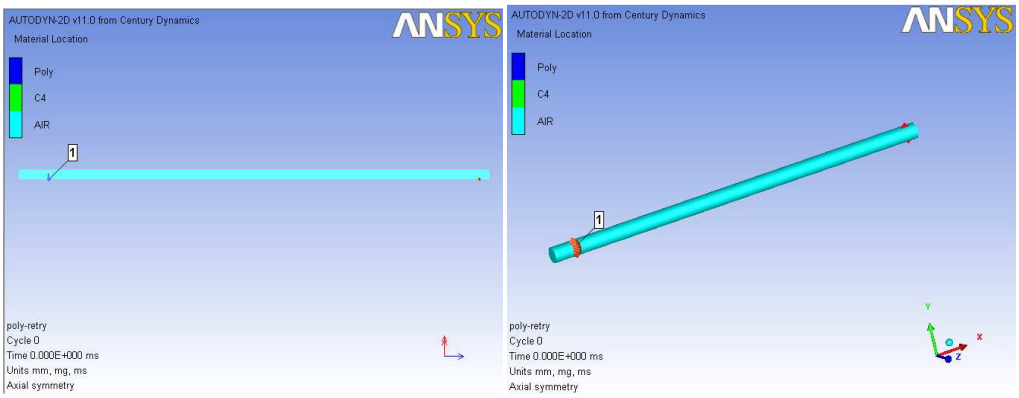

Figure 67: AUTODYN 2-D Model

Figure 68: AUTODYN 2-D Revolved Model

The modulus vs. time and strain vs. time histories from the Split Hopkinson Bar tests were used to model the polyurethane foam material. The simulated foam was not modeled as porous but as a solid material with the same material characteristics as the polyurethane foam. A Lagrange solver was defined for the material. A fixed boundary at the top of the 2D foam plate model was defined.

The 1lb hemispheres of c4 explosive used during the EMRTC testing were also modeled and placed at the various standoff distances used during the EMRTC testing. A Lagrange solver was defined for the c4.

The air also had to be modeled for propagation of the shock wave from the explosion. An Euler Ideal gas solver was defined for the air. A transmit boundary was placed on the two vertical boundaries and the top horizontal boundary to allow for the explosion to transmit and not be reflected causing an inaccurate blast wave.

A detonation point was set at the rear of the c4 explosive. A simulated gage was placed at the center rear of the simulated foam plate as in the EMRTC testing. [73, 74, 75, 76]

A simulation for each of the EMRTC samples and standoff distances were performed. The gage velocities time history data was then differentiated to find the position of the

gage, and thus the center of the sample, and the maximum initial deflection of the samples. A step by step history of the dry sample at 25 ft simulation can be seen below.

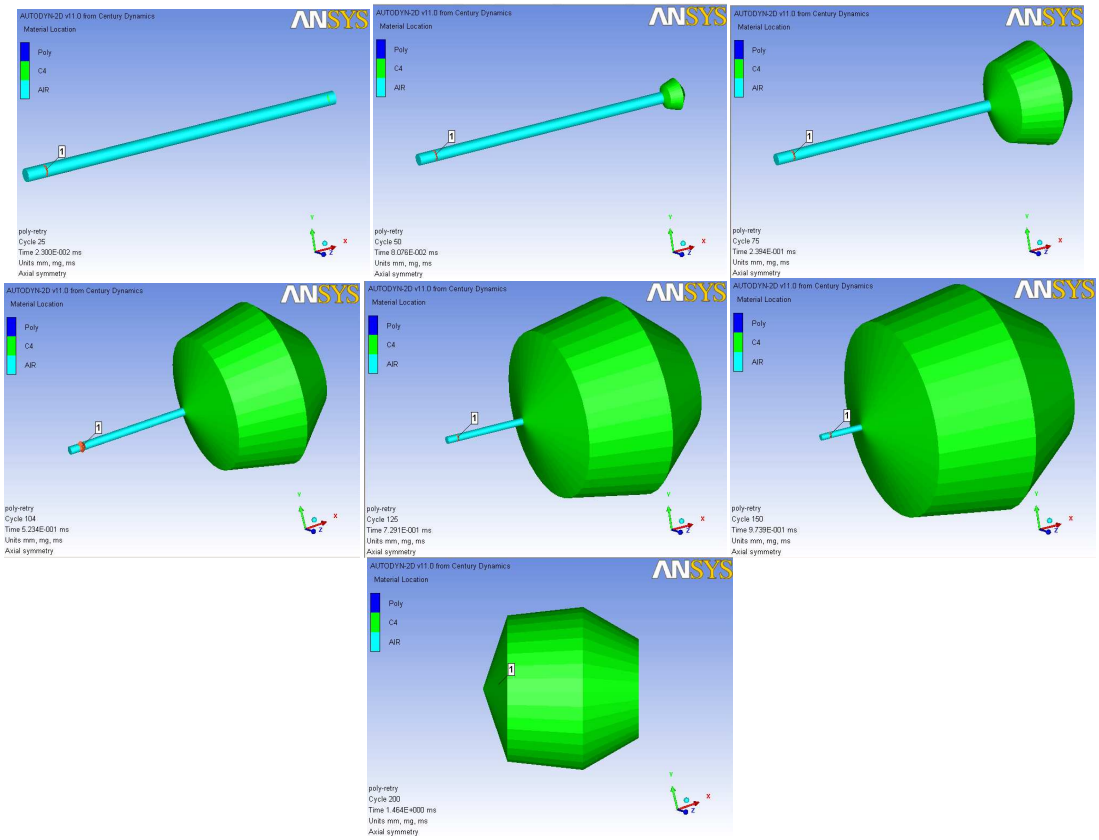

Figure 69: Step by step history of the dry sample at 25 ft simulation.

3. Results

3.1 Observations and Results of Air Blast Test

Table 5 is a list of the face reflected pressures and displacement of the 4 different samples during the explosive testing at EMRTC.

Test	Displacement (in)	Displacement (in)	Displacement (in)	Displacement (in)	Reflected pressure (psi)	Reflected pressure (psi
	Acc. 1	**Acc. 2**	**Phantom 1**	**Phantom 2**	**PR 1**	**PR 2**
	Wet (South)	**Dry (North)**	**Wet (South)**	**Dry (North)**		
Test 1	0.131	0.14	0.144	0.148	2.97	2.85
Test 2	0.203	0.234	0.219	0.242	4.63	4.77
Test 3	0.304	0.353	0.342	0.352	7.2	6.85
Test 4	0.138	0.146	0.131	0.147	2.99	2.82
Test 5	0.306	0.321	0.325	0.313	6.67	7.43
Test 6	1.28	N/A	N/A	N/A	Clipped	Clipped

Table 5: Displacement and Reflected Pressure Experimental Results

The reflected pressure difference from the top and the bottom of the stand was negligible for all of the 6 tests and can be explained as the error in the pressure sensors themselves.

It was hypothesized that the wet samples would deflect less and exhibit less acceleration than the dry samples due to the added mass of the water. Table 5 shows that the wet samples deflected less than the dry samples except for the phantom data for test number 5. This discrepancy may have been due to some slight delamination of the accelerometer on the wet sample during tests number 4 or 5.

No data was gathered from test number 6 due to the total separation of the accelerometers from the samples during loading. A better adhesive will have to be used in the future to prevent this from happening at ranges less than 15 ft.

Table 6 shows that the wet samples exhibited close to half the initial forward and reverse acceleration as the dry samples. This makes sense due to the added mass of water in the wet samples requiring more energy for movement.

Test	Distance (ft)	G's Wet	G's Dry	Impulse 1 (psi s)	Impulse 2 (psi s)	Avg Impulse (psi s)
1	45	117.47	212.3	2.75E-03	2.70E-03	0.002724
2	35	183.7	296	3.58E-03	3.89E-03	0.003738
3	25	298.51	442.32	5.23E-03	5.46E-03	0.005345
4	45	162.43	222.68	2.90E-03	2.74E-03	0.002819
5	25	380.75	593.64	5.27E-03	5.43E-03	0.0053495
6	15	850.6	1212.44	9.53E-03	9.74E-03	0.009635

Table 6: Impulsive Loading and Initial G's of the Samples Experimental Results

Table 6 also lists the initial impulses (lb*s) during the tests calculated by integrating the reflected pressure curves from the pressure sensors on the test set up. This data was used to calculate the impulse velocity (s) [reference] with the equation:

$$V = \frac{I}{\rho H} \qquad \text{(eq. 70)}$$

V = Impulse Velocity (s)

ρ = Material Density (lb/in^3)

H = Sample Thickness.

The impulse velocities are listed in Table 7 below:

Test	Impulse Velocity Wet (s)	Impulse Velocity Dry (s)
1	8.2937	20.2103
2	11.3811	27.7335
3	16.2739	39.6564
4	8.5830	20.9151
5	16.2876	39.6898
6	29.3356	71.4854

Table 7: Impulse Velocities

These values were needed in order to calculate a theoretical displacement of the samples to compare to the experimental values.

Next the plastic collapse moment of the samples had to be calculated from the equation [ref.].

$$M_o = \frac{\sigma_o H^2}{4} \quad \text{(eq. 71)}$$

M_o = Plastic Collapse Moment

σ_o = Material Yield Stress

The approximate material yield stress at the high impulse loading rates of the dry and wet samples were back calculated from the following equations as 1750 psi for the dry samples and 800 psi for the wet samples.

The non dimensional initial kinetic energy (Table 6) was calculated from the following equation [ref.]:

$$\lambda = \frac{\mu V^2 R^2}{M_o H} \quad \text{(eq. 72)}$$

λ = Non-Dimensional Initial Kinetic Energy

R= Mass Per Unit Area (slugs/in^2)

Test	Non Dimensional Initial Kinetic Energy Wet	Non Dimensional Initial Kinetic Energy Dry
1	1.8238	4.0961
2	3.4345	7.7133
3	7.0223	15.7711
4	1.9533	4.3868
5	7.0341	15.7976
6	22.8186	51.2472

Table 8: Initial Kinetic Energy

The initial theoretical displacement (Table 7) was then calculated from:

$$W_f = \frac{H(0.84)\lambda}{12} \qquad \text{(eq. 73)}$$

W_f = Maximum Initial Displacement of the Center Point of the Sample Face

Test	Initial Theoretical Displacement Wet (in)	Initial Theoretical Displacement Dry (in)
1	0.0638	0.1433
2	0.1202	0.2699
3	0.2457	0.5519
4	0.0683	0.1535
5	0.2461	0.5529
6	0.7986	1.7936

Table 9: Theoretical Maximum Displacement

Tables 9 and 10 assume a yield stresses of 1.4 psi for the samples at the high impulsive velocities in Table 5.

	Mass/Unit Area ($slug/in^2$)	Test 1 Deflection (in)	Test 2 Deflection (in)	Test 3 Deflection (in)
Experimental Dry	1.12E-05	0.14	0.234	0.353
Experimental Wet	2.97E-05	0.131	0.203	0.304
Theoretical Dry	1.12E-05	0.1434	0.27	0.552
Theoretical Wet	2.97E-05	0.0638	0.1202	0.2458
	Mass/Unit Area ($slug/in^2$)	**Test 4 Deflection (in)**	**Test 5 Deflection (in)**	**Test 6 Deflection (in)**
Experimental Dry	1.12E-05	0.146	0.321	N/A
Experimental Wet	2.97E-05	0.138	0.306	1.28
Theoretical Dry	1.12E-05	0.1535	0.5529	1.7937
Theoretical Wet	2.97E-05	0.0684	0.2462	0.7987

Table 10: Experimental and Theoretical Deflections Compared

The data in Table 10 is plotted out for each test in the next six graphs. It can be seen that using a yield of 1.4 psi for the dry samples gives a close comparative theoretical displacement to the experimental values but not as close for the wet samples. Figures 70-75 plot the theoretical and experimental displacements of the samples vs. the mass of the samples.

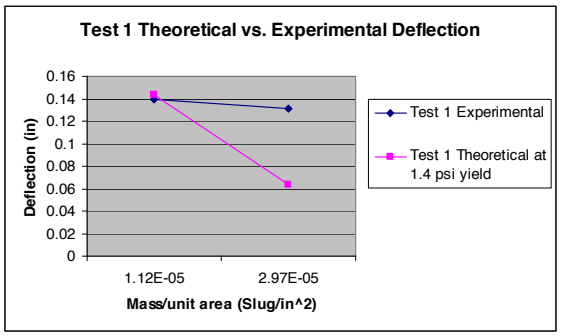

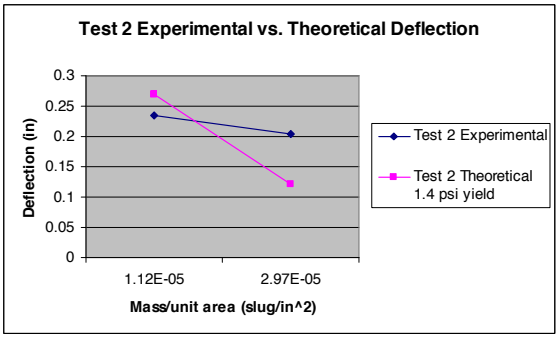

Figure 70 and 71: Test 1 and 2 Theoretical vs. Experimental

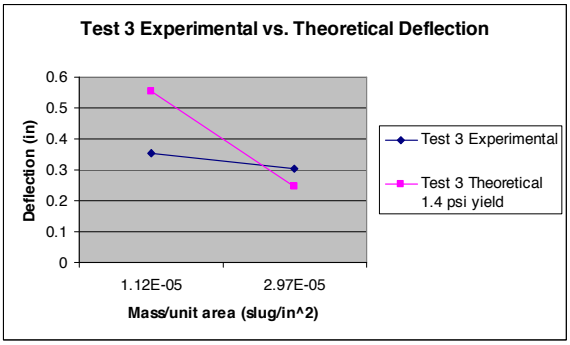

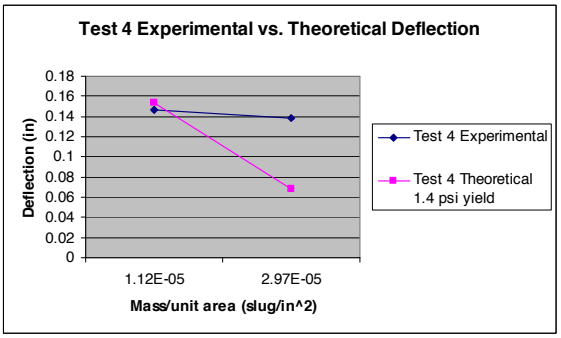

Figure 72 and 73: Test 3 and 4 Theoretical vs. Experimental

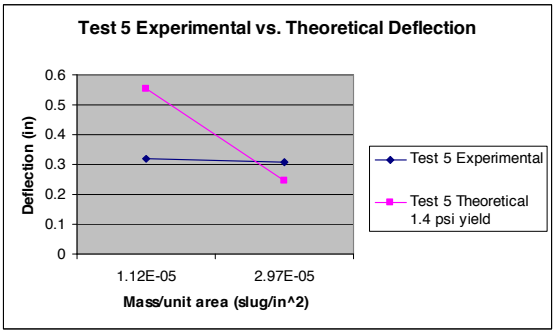

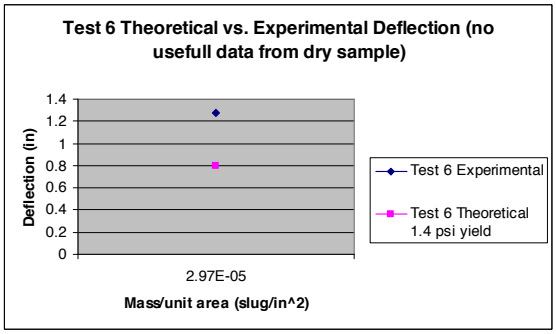

Figure 74 and 75: Test 5 and 6 Theoretical vs. Experimental

To have the wet samples theoretical deflection come close to the experimental values the wet samples would have to exhibit a yield stress at approximately 0.85 psi. This would

give results with more error for the dry samples. This would give theoretical displacements of:

Test	Initial Theoretical Displacement Wet (in)	Initial Theoretical Displacement Dry (in)
1	0.1051	0.2361
2	0.1979	0.4446
3	0.4048	0.9091
4	0.1126	0.2528
5	0.4054	0.9106
6	1.3154	2.9542

Table 11: Theoretical Deflections at 0.85 psi Yield Stress

3.2 Split Hopkinson Bar Results

Figure (x) below show examples of the incident, reflected, and transmitted pulses as seen in DIAdem.

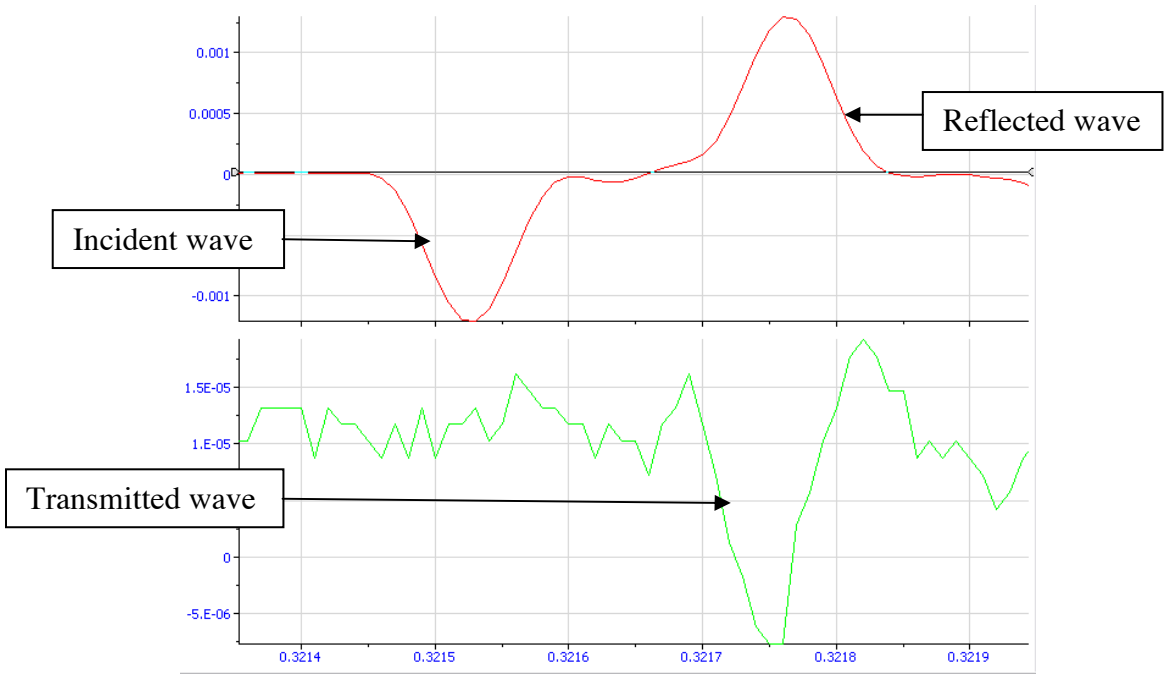

Figure 76: Example Incident, Reflected, and Transmitted Wave Data

Below are the velocities for each of the tank pressures, the wave pulse period, the wave pulse frequency, and the wave velocity from the incident wave.

10 psi = 20 ft/s, +/- 2 ft/s

15 psi = 44 ft/s, +/- 3 ft/s

20 psi = 60 ft/s, +/- 4 ft/s

Wave Pulse Period = 195e-6 s

Frequency = 5.128 kHz

Wave velocity = 4896 m/s

3.2.1 Split Hopkinson Bar Data Plots

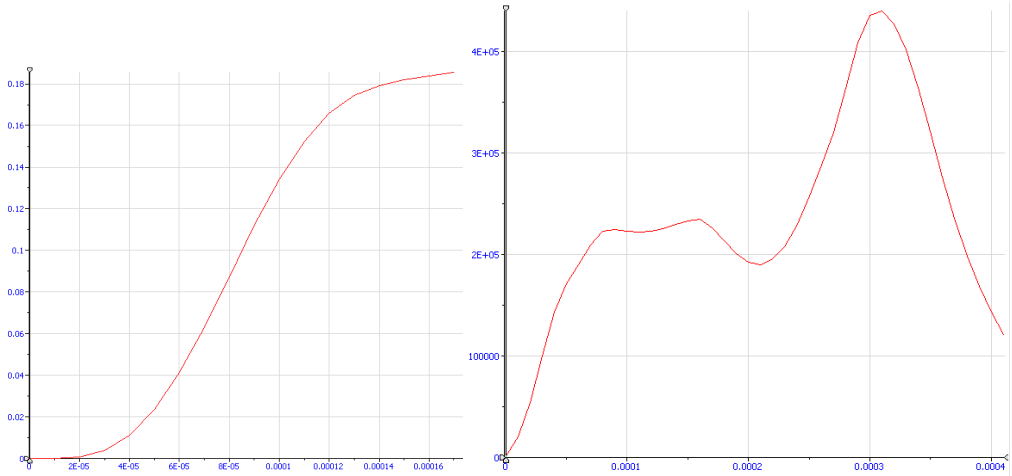

Figure 77: Strain vs. Time Test 1 10psi Dry-Figure 78: Stress vs. Time Test 1 10psi Dry

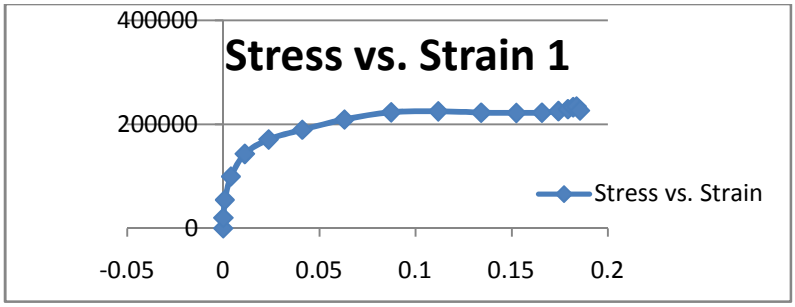

Figure 79: Stress vs. Strain Test #1 10psi Dry

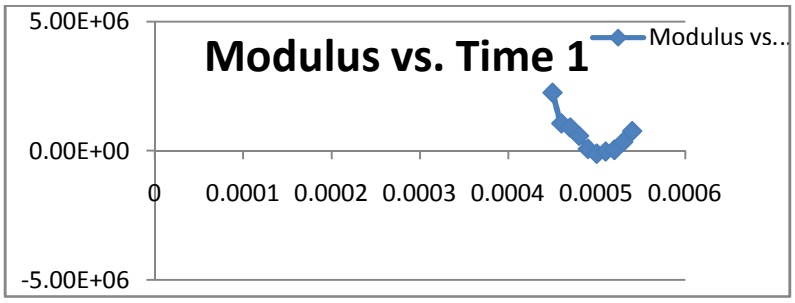

Figure 80: Modulus vs. Time Test #1 10psi Dry

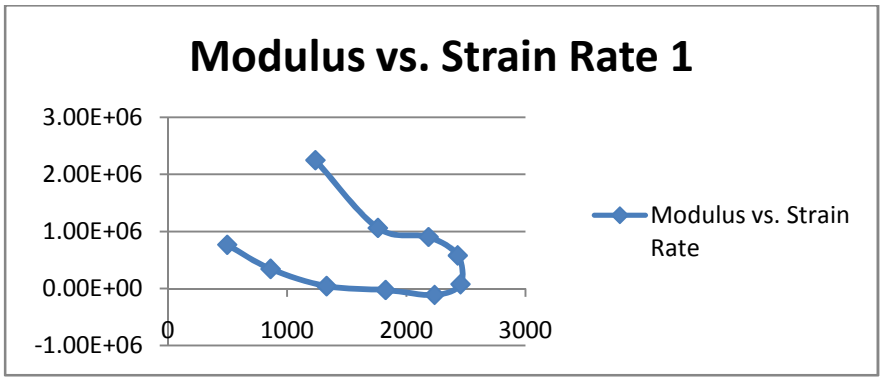

Figure 81: Modulus vs. Strain Rate Test #1 10psi Dry

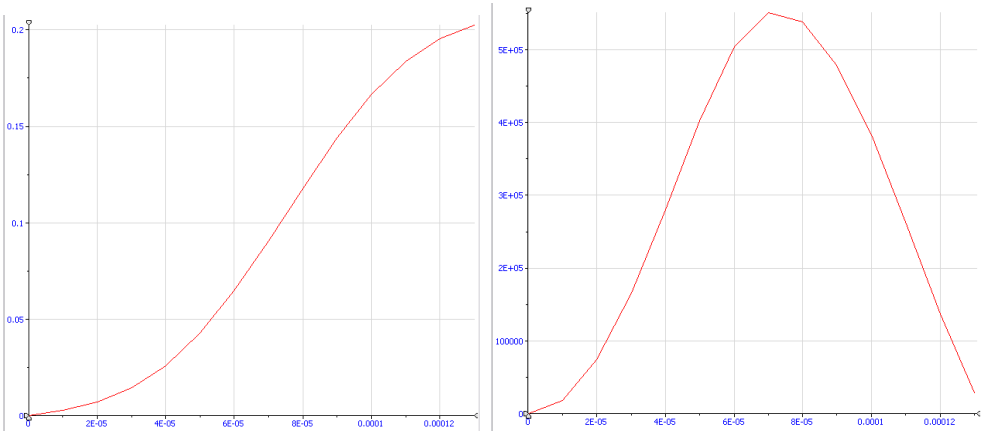

Figure 82: Strain vs. Time Test 6 10psi Wet-Figure 83: Stress vs. Time Test 6 10psi Wet

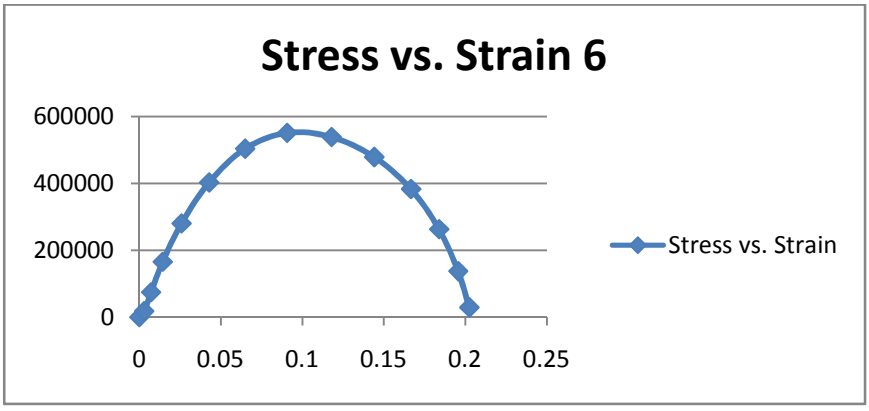

Figure 84: Stress vs. Strain Test #6 10psi Wet

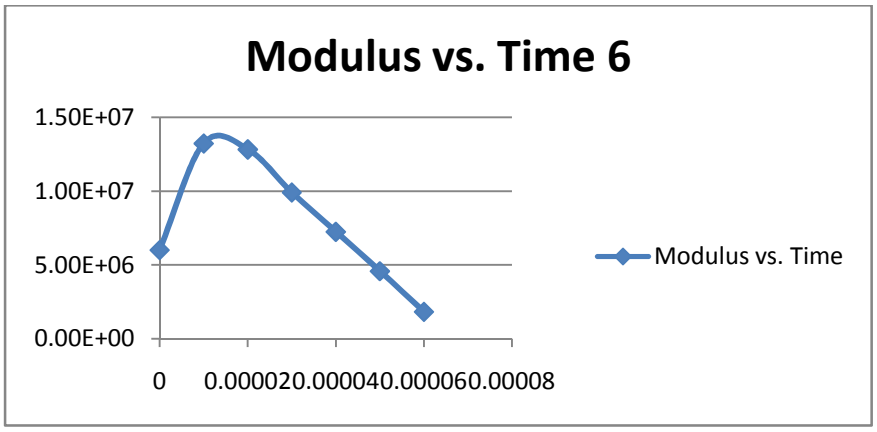

Figure 85: Modulus vs. Time Test #6 10psi Wet

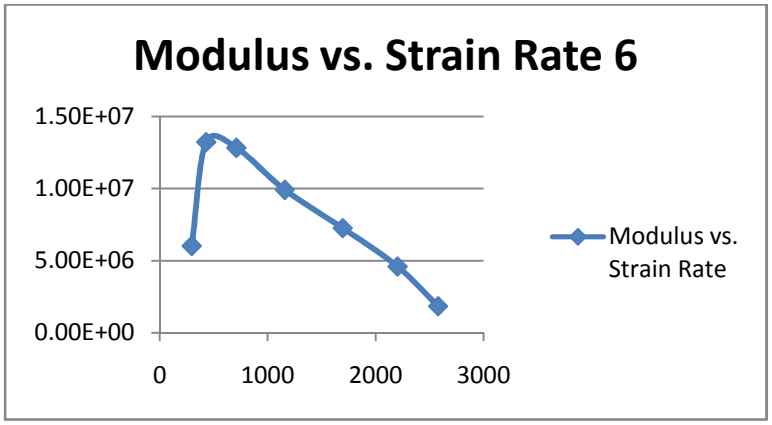

Figure 86: Modulus vs. Strain Rate Test #6 10psi Wet

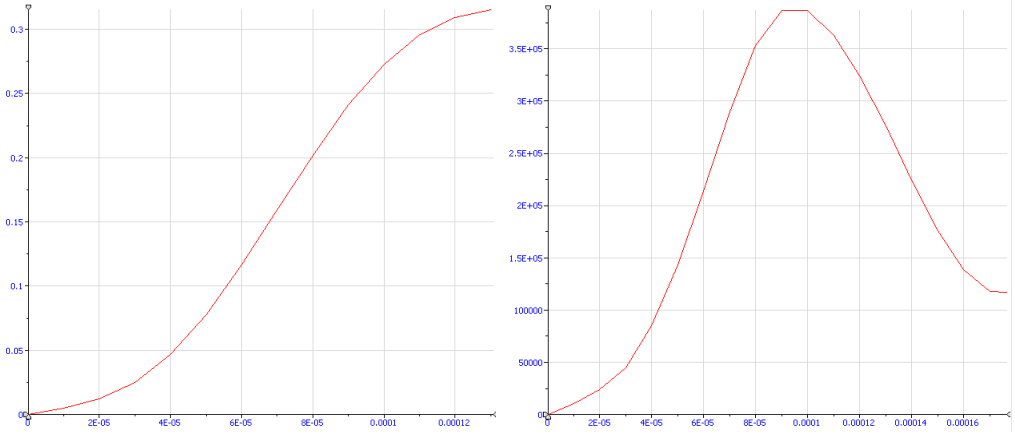

Figure 87: Strain vs. Time Test 13 15psi Dry-Figure 88: Stress vs. Time Test 13 15psi Dry

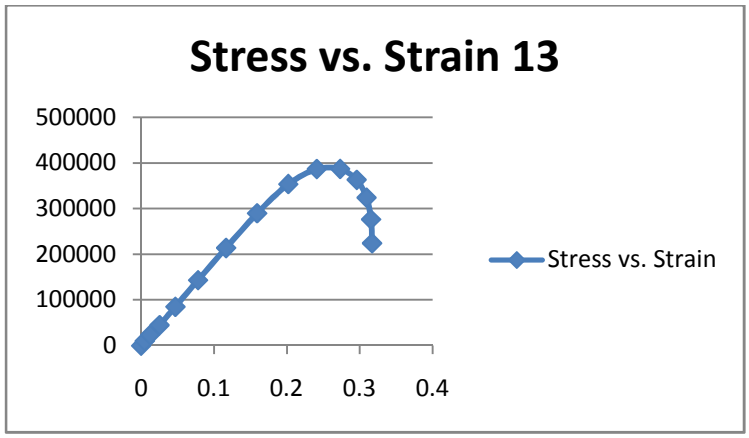

Figure 89: Stress vs. Strain Test #13 15psi Dry

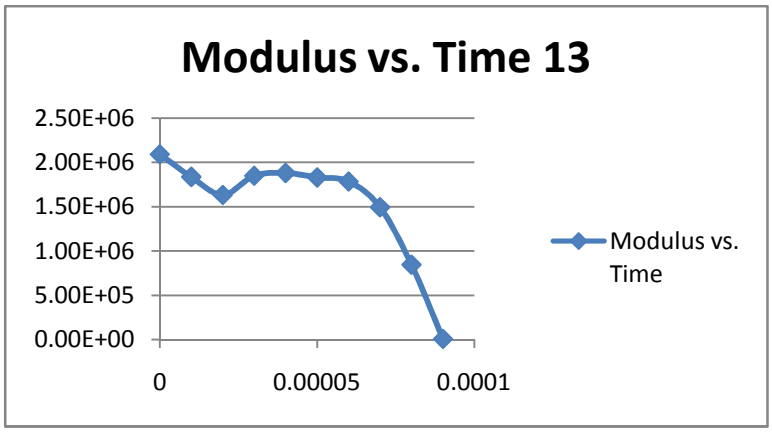

Figure 90: Modulus vs. Time Test #13 15psi Dry

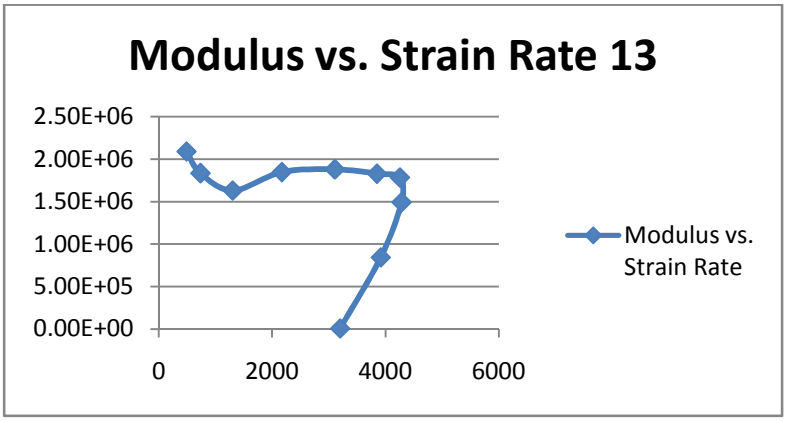

Figure 91: Modulus vs. Strain Rate Test #13 15psi Dry

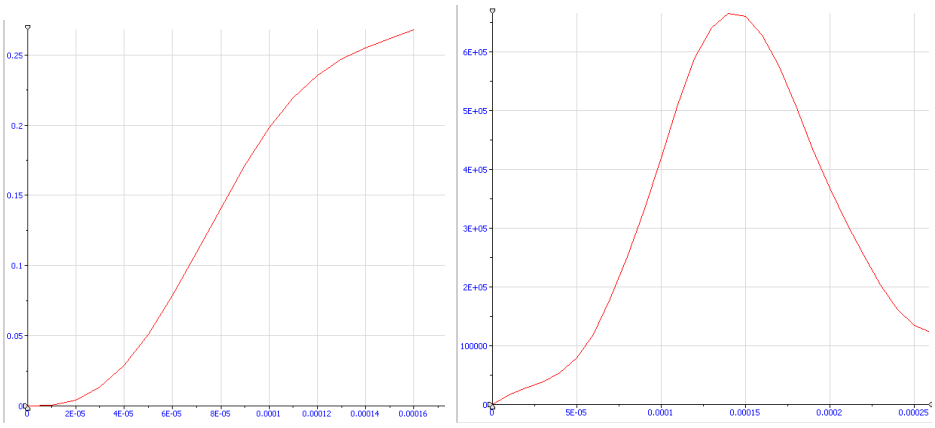

Figure 92: Strain vs. Time Test 16 15psi Wet-Figure 93: Stress vs. Time Test 16 15psi Wet

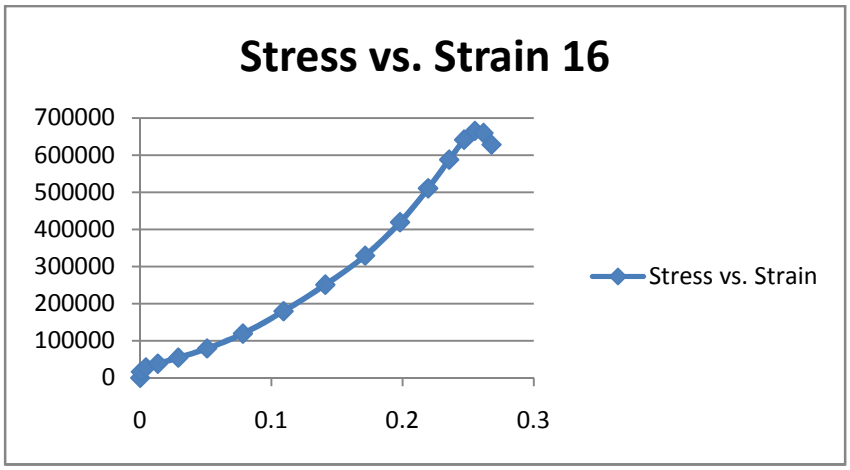

Figure 94: Stress vs. Strain Test #16 15psi Wet

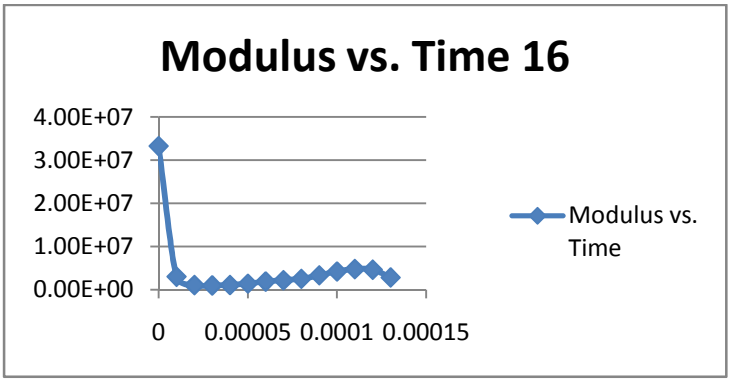

Figure 95: Modulus vs. Time Test #16 15psi Wet

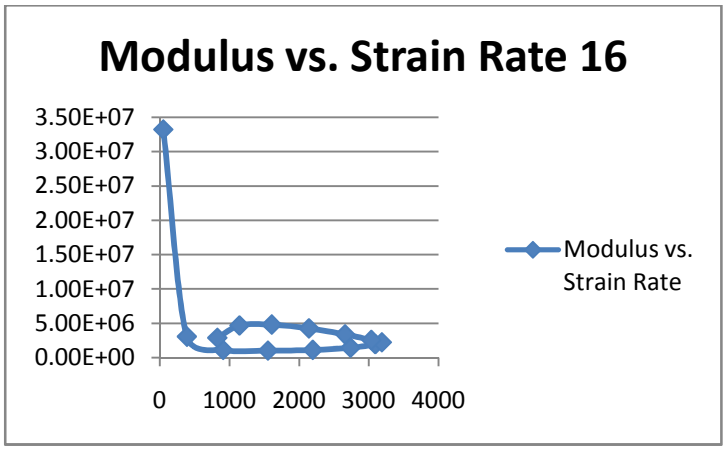

Figure 96: Modulus vs. Strain Rate Test #16 15psi Wet

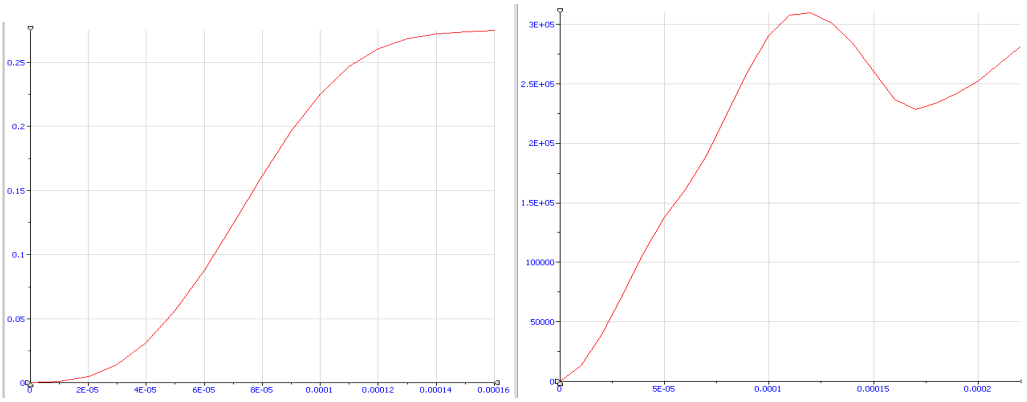

Figure 97: Strain vs. Time Test 12 20psi Dry-Figure 98: Stress vs. Time Test 12 20psi Dry

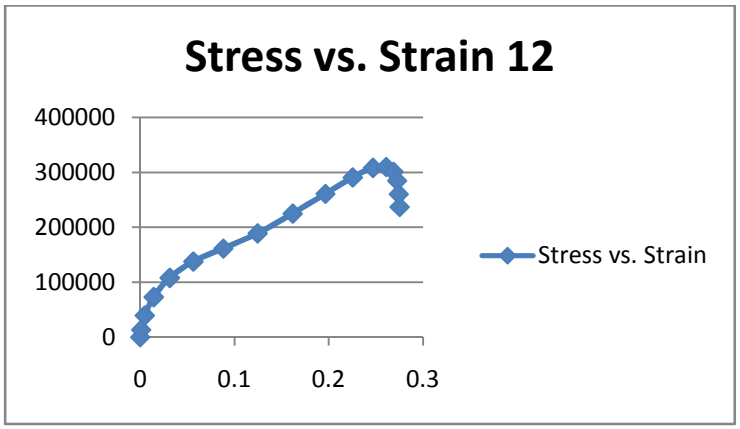

Figure 99: Stress vs. Time Test #12 20psi Dry

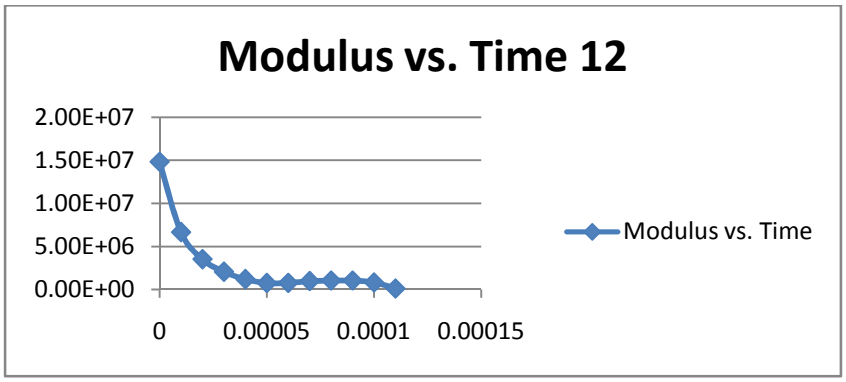

Figure 100: Modulus vs. Time Test #12 20psi Dry

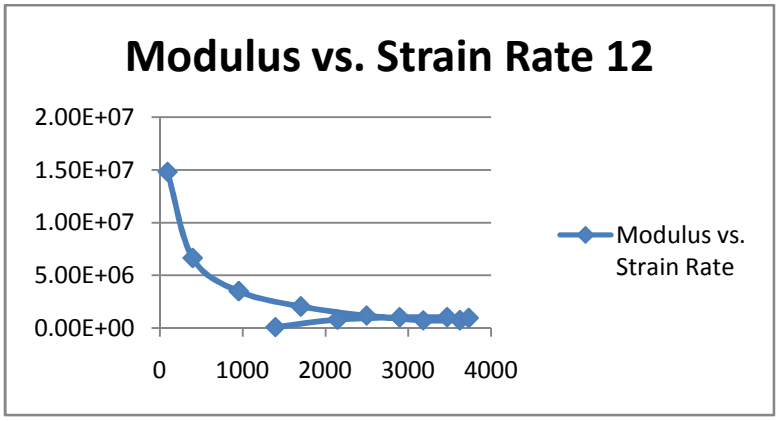

Figure 101: Modulus vs. Strain Rate Test #12 20psi Dry

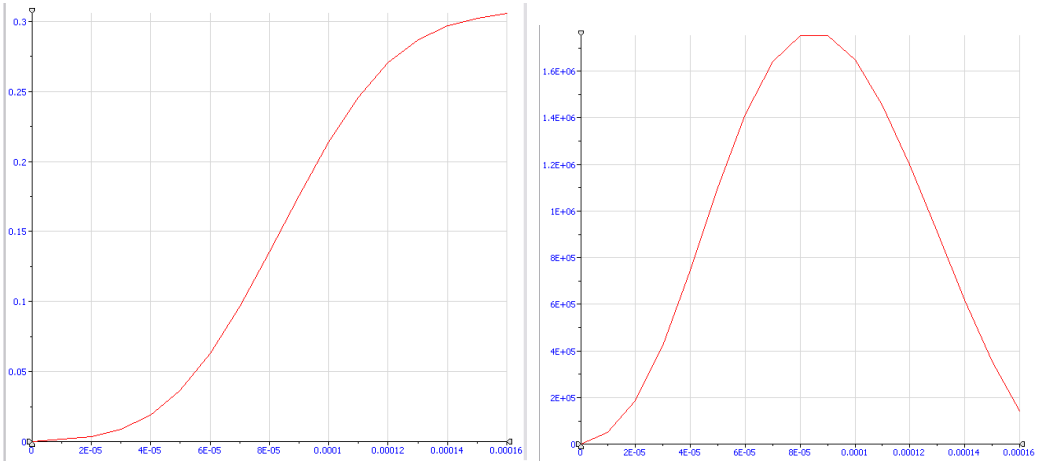

Figure 102: Strain vs. Time Test 17 20psi Wet-Figure 103: Stress vs. Time Test 17 20psi Wet

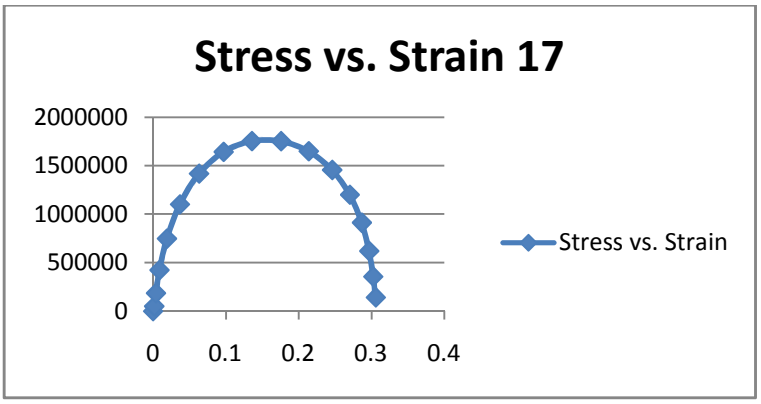

Figure 104: Stress vs. Strain Test #17 20psi Wet

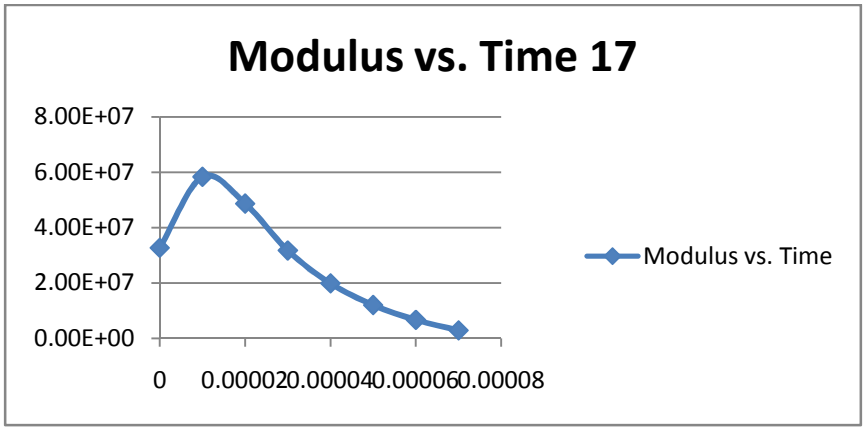

Figure 105: Modulus vs. Time Test #17 20psi Wet

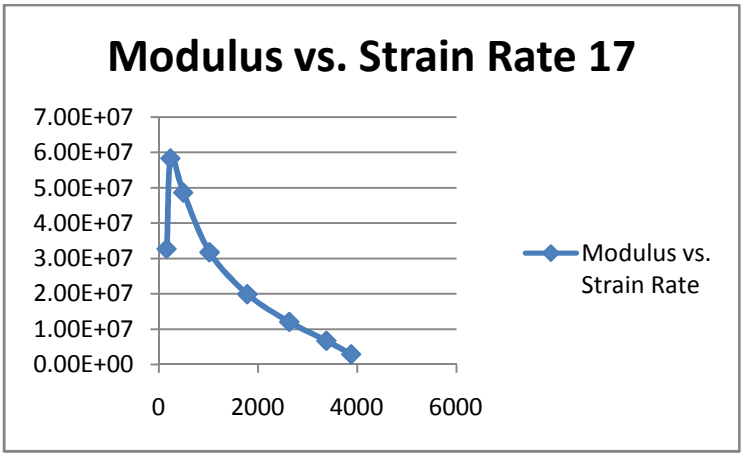

Figure 106: Modulus vs. Strain Rate Test #17 20psi Wet

Below are examples of the plotted data from the various tests. The top two plots are the strain gages[????]. The next two plots are the light sensors, and the bottom plot is the pressure sensor.

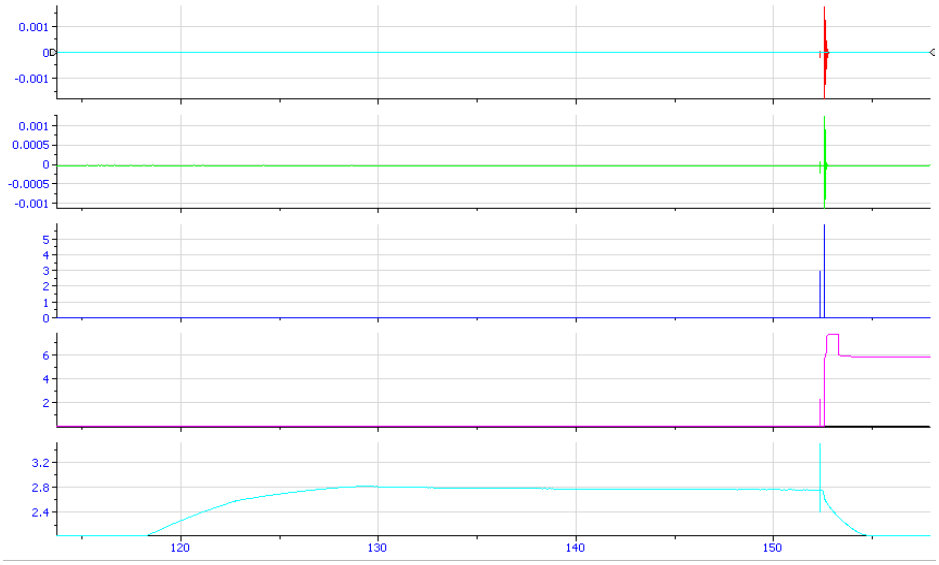

Figure 107: Example DIAdem Label the plots-1

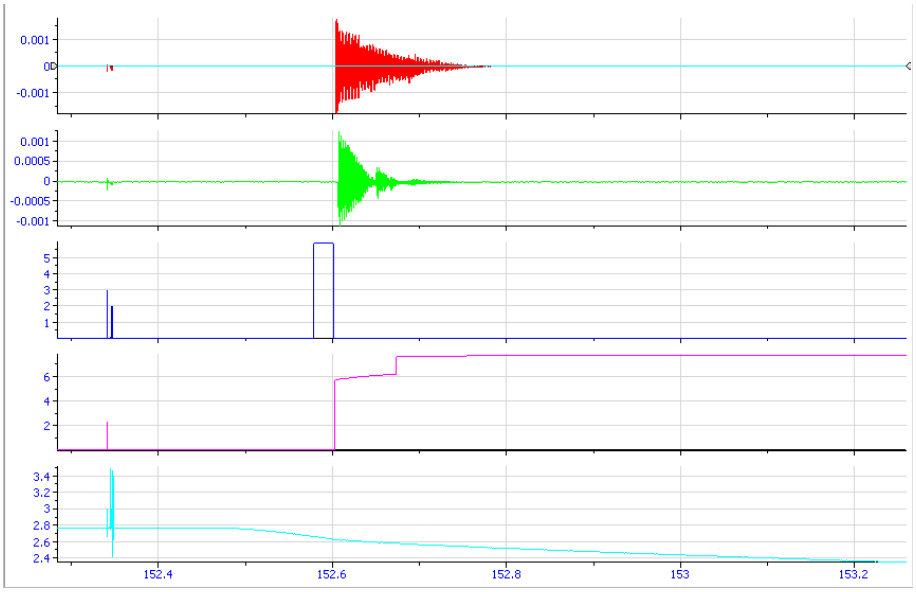

Figure 108: Example DIAdem Label the plots-2

The maximum value results from the Split Hopkinson Bar tests are shown in the table below.

Test #	Sample	Modulus (Mpa)	strain rate (/s)	Tank Pressure (psi)
1	dry	2.25	1088	10
2	dry	2.53	1101	10
3	dry	2.33	1078	10
4	dry	2.84	1086	10
5	dry	2.13	1088	10
6	wet	132	1538	10
7	wet	130	1523	10
8	wet	128	1532	10
9	wet	134	1567	10
10	wet	133	1525	10
11	dry	21.3	2341	15
12	dry	148	1687	20
13	dry	20.9	2461	15
14	dry	22.6	2511	15
15	dry	19.8	2437	15
16	wet	332	1687	15
17	wet	583	1937	20
18	wet	327	1701	15
19	wet	341	1665	15
20	wet	311	1623	15

Table 11: Maximum Value Results from the Split Hopkinson Bar Tests

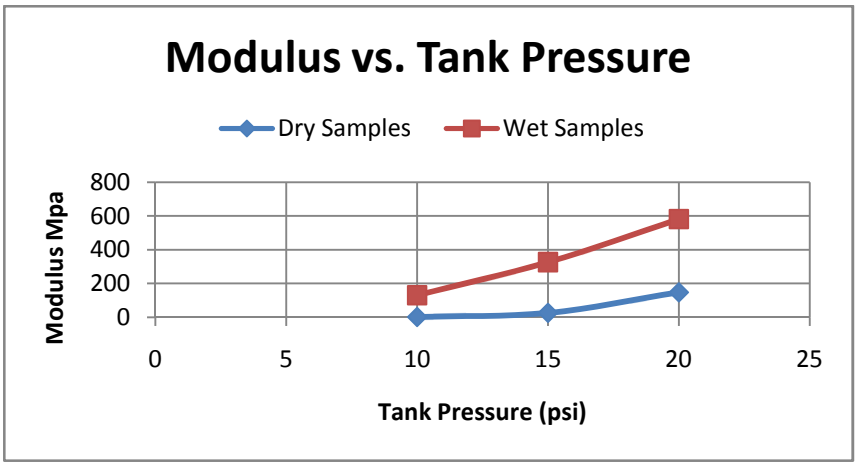

Figure 109: Modulus vs. Tank Pressure

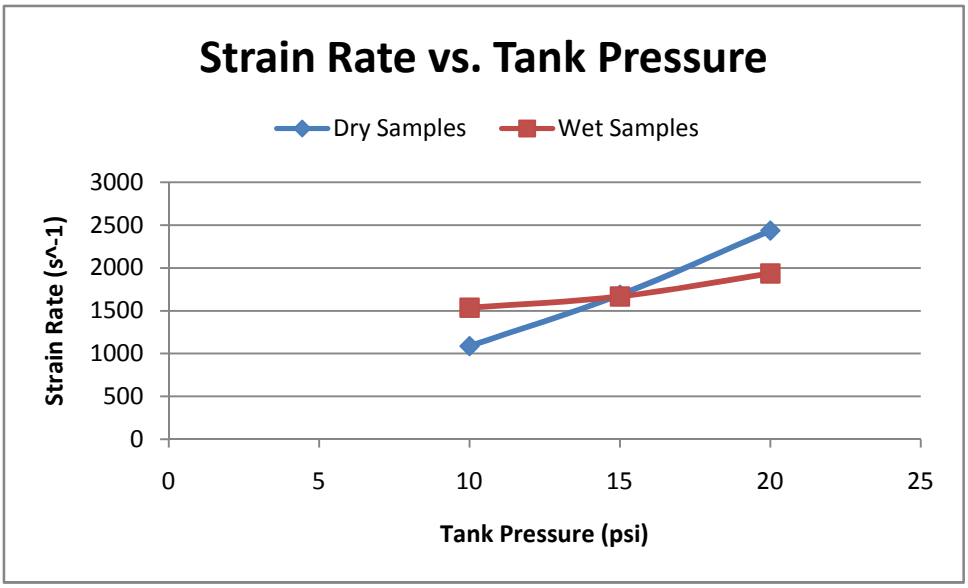

Figure 110: Strain Rate vs. Tank Pressure

From the above table it can be seen that the wet samples have a consistently greater modulus than the dry samples. The wet samples modulus is increasingly higher than the wet samples as the strain rate increases. The dry samples have a slower strain rate at 10 psi but as the pressure is increased, (the impact velocity), the wet samples have a slower

strain rate than the dry samples. The strain in the dry samples quickly increase to 30% strain by 15 psi, while the wet samples take until 20 psi to show the same strain.

The wet samples tested at 15 psi had their lexel stick to the input and output bars but they did not fail.

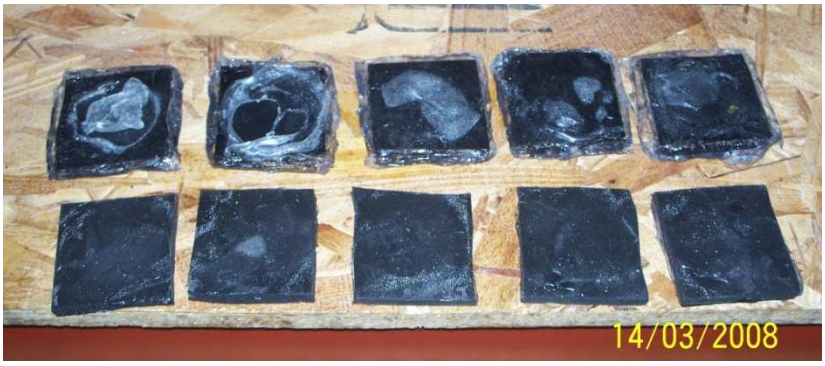

Figure 111: Foam Samples After Split Hopkinson Bar Testing

The samples tested at 20 psi all showed signs of failure, but the lexell remained intact. Higher strain and strain rate tests previously carried out showed definite signs of material failure. 20 psi was the maximum pressure that could be used before the strain gage solder connections would detach because nylon was the least impedance wave shaper material that could be used while still being able to make out the incident and reflected waves in the input bar.

Figure 112: Damaged Foam Samples and Wave Shapers

3.3 AUTODYN Results

The results from the Split Hopkinson Bar tests were used in AUTODYN to simulate the air blast testing. Below is the table of the results from AUTODYN compared to the results from the EMRTC testing.

Standoff distance (ft)	Deflection AUTODYN wet (in)	Deflection experimental wet (in)	% Difference
25	0.336	0.306	9.803921569
25	0.336	0.304	10.52631579
35	0.231	0.203	13.79310345
35	0.231	0.203	13.79310345
45	0.138	0.138	0
45	0.138	0.131	5.34351145
Standoff distance (ft)	**Deflection AUTODYN dry (in)**	**Deflection experimental dry (in)**	**% Difference**
25	0.367	0.321	14.33021807
25	0.367	0.353	3.966005666
35	0.245	0.234	4.700854701
35	0.245	0.234	4.700854701
45	0.151	0.146	3.424657534
45	0.151	0.14	7.857142857

Table 12: Results from AUTODYN Compared to the Results from the EMRTC Testing

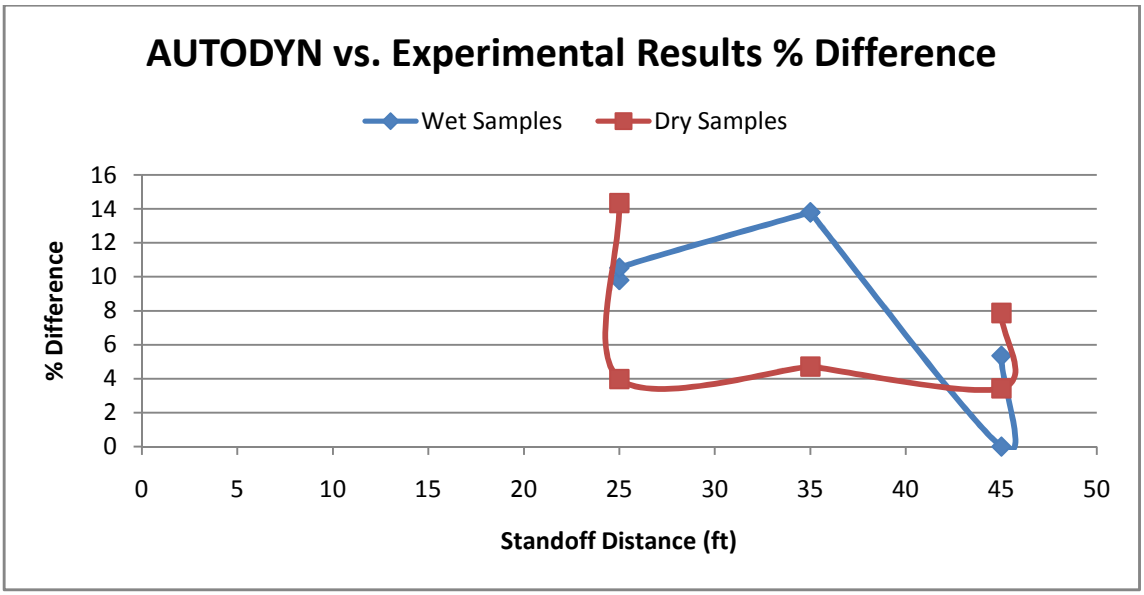

Figure 113: AUTODYN vs. Experimental Results % Difference

These results are plotted in the following figure.

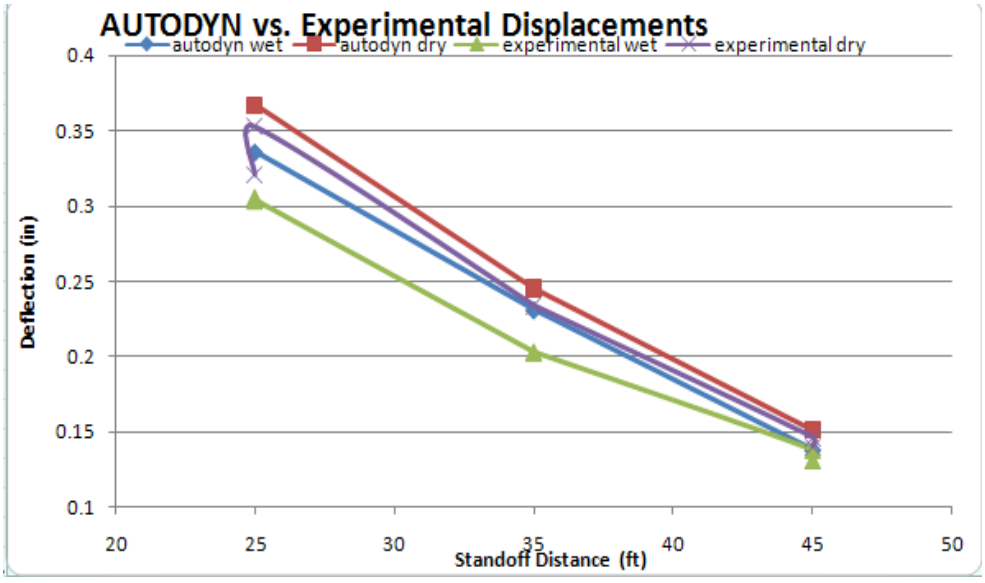

Figure 114: AUTODYN vs. Experimental Displacements

As can be seen from the figure above the AUTODYN model was very close at large standoff distances. The smaller the standoff distance the more discrepancy there is between the experimental and modeled. Also, the model for the dry samples stayed reasonably close throughout, while the wet samples had more discrepancy at closer standoff distances. In both the wet and dry samples the AUTODYN model showed a larger increase in deflection as the standoff distance was lessened than the experimental results showed. This is very apparent in the comparison of the experimental wet samples and the AUTODYN wet samples. In both AUTODYN and the experiments the samples did not fail.

Conclusion

We expected that the dry samples would have the most amount of deflection due to having less mass than the wet samples and therefore exhibiting more initial acceleration to accommodate the same amount of load as the wet samples. Table 10 shows that the experimental and theoretical data agreed with this assumption except for the camera data from test 5 (Table 5). This error was due to a slight delaminating of the accelerometer from the wet sample during test number 4.

We expected the dome shaped samples to deflect more than the flat samples due to more surface area exposed to the impulsive load. At first glance Table 7 seems to show that the domed samples do deflect more than the flat samples. A couple of things needed to be considered. The impulse data for the dome shaped samples is slightly higher than the

same for the flat samples. Also, the dome shaped samples inherently have more surface area than the flat samples [59]. Combining equations 60 through 66 yields:

$$W_f = \frac{(0.28)\mu I^2 R^2}{\rho^2 H^4 \sigma_o} \quad \text{(eq. 74)}$$

Equation 74 shows that the impulse and radius have squared influence on the deflection of the sample. Table 9 below shows that the dome shaped samples actually were slightly more efficient in resisting deflection than the flat samples.

Tests	Theoretical Ratio of Deflection With Different Impulses and Different Surface Areas (Dome Shaped/Flat)	Experimental Difference of Deflection (Dome Shaped/Flat)	Experimental/ Theoretical	Dome Shaped Comparative Efficiency (%)
4/1 Wet	1.09979	1.05344	0.957856	+4.2
4/1 Dry	1.1279	1.04286	0.924603	+7.5
5/3 Wet	1.02879	1.00658	0.978412	+2.2
5/3 Dry	1.05492	0.909348	0.862007	+13.8

Table 13: Efficiency Difference of Dome Shaped Samples from Flat Samples for Deflection

This must be due to the dome shape and the added surface area of the dome shaped samples absorbing or deflecting more energy than the flat samples. This shape factor will have to be studied more in depth in the future to analyze its magnitude of affect on energy absorption.

Previous static indentation testing led to an assumption of a possible softening affect of the water on the foam material itself (Figure 115).

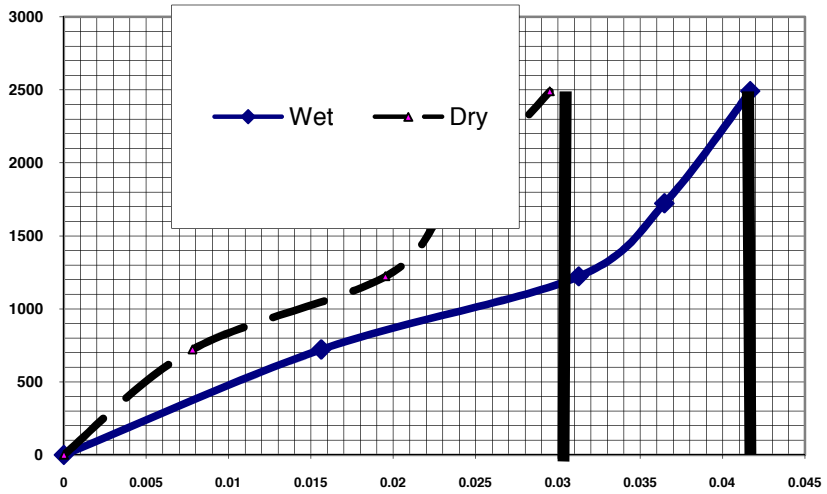

Figure 115: Stress (Pa) vs. strain diagram ½ in Plate Under Cylinder, Area Difference is 19%

As shown in Figure 34, the stress vs. strain curve from 0 to 0.01 strain shows a lower modulus for the wet sample at this low strain rate. This is shown by the smaller slope for the wet sample. Interestingly enough this softening affect was not observed in these series of blast loading tests.

Table 10 assumes that the yield stress of both the wet and dry samples is 1.4 psi. This closely agrees with the deflections experimentally observed for the dry samples (Table 5). The given values of the compressive yield stress for the sample material range from ~4 psi to ~8 psi [30]. The model used to calculate the theoretical displacements in the circular plate section of this paper is not valid for visco-elastic materials, but it does yield a close value to the book value for the dry material and was the starting point to modeling the polyurethane foam [30].

For the wet samples to have close to experimentally observed values they would have to exhibit a yield stress of ~0.85 psi according to the model used in this paper (Table 11). Figures 28 through 33 also show that the wet samples exhibited more deflection than the theoretical model yield value of 1.4 psi would allow for. The ratio of dry to wet yield strength in the test shown in Figure 34 is ~1.67. The ratio of dry to wet yield strength in this test is ~1.65. This shows that there is an affect of the water on the foam material. This softening affect will also have to be further studied in the future to determine the actual magnitude of it's affect on the foams material properties.

The Split Hopkinson bar tests showed less increase in modulus in the dry samples more deflection at higher strain rates, but the modulus were much greater than those initially calculated with not taking the porous structure into account. The wet samples showed greater increase in modulus and less increase in deflection at higher strain rates. The wet samples also showed more that 10 times the modulus than the dry samples with only 75% of the strain. Yet, the wet samples still showed 80-90% of the deflection that the dry

samples experienced. The Split Hopkinson Bar strain rates were within 10-20% of the experimental strain rates, but the Split Hopkinson Bar strains were compressive while the experimental strains were compressive to the face facing the blast and tensile perpendicular to the shock wave acting on the face of the samples. Due to the close AUTODYN results, this did not seem to have a great affect on the results.

From these experiments it can be said that, while it would add 700% mass to the foam, the wet foam has a consistently much higher modulus with less strain under blast loading conditions. The difference in foam thickness also had minimal affects on this property. This could lead to a much better energy absorbing and strong material to be used for protection from blast loading. It has been shown that foams can be used for protection against impacts, but the foams would be much more affective if the pores were filled with water. This could be used for protection of buildings, military vehicles, and possibly personnel armor. Future work may show that this composite could also be used for a wide range of applications.

5. Future Work

1. These experiments were carried out in small numbers. To better characterize this composite longer and more numerous series of tests would need to be conducted.
2. The ball rebound test described in this paper should be conducted to keep the loading in the same general tensile manner that was experienced during the blast testing.

3. The Split Hopkinson Bar apparatus could be improved on by lengthening the input and output bars. This would allow for more plastic deformable wave shapers, which would allow for higher strain rate tests due to the longer rise time in the incident waves. This would also allow for thicker samples to be tested while still generating transmission waves that would be visible over the noise in the instrumentation.
4. A data acquisition system capable of higher sample rates should be purchased to better sample the wave history through the input and output bars of the Split Hopkinson Bar apparatus.
5. Heat and noise absorption test should be run at more extent to better characterize the absorptive properties of this material.
6. Once the material characteristics are better tested the composite and foam should be tested against each other while placed between rigid plates such as aluminum and steel. The testing should focus on impact and blast loading situations. This would possibly add to the materials potential uses.

6. References

[1] Onenbook, http://www.nap.cdu/onenbook/0309087007/html , "Material Research to Meet 21st Century Defense Needs", The National Academy of Sciences, 2001.

[2] "Bioinspired and Bioderived Materials", Materials Research to Meet 21st Century Defence Needs, National Academy of Sciences, 2003.

[3] Giurgiutiu V., Cuc A., "Embedded Non-destructive Evaluation of Structural Health Monitoring, Damage Detection, and Failure Prevention", University of South Carolina, Department of Mechanical Engineering, The Shock and Vibration Digest, Vol. 37, No. 2, March 2005.

[4] Elert G., and Students, "The Physics Factbook", http://hypertextbook.com/facts/2002/AnnaYarusskaya.shtml

[5] "Wikipedia, the Free Encyclopedia", http://en.wikipedia.org

[6] Ghosh, A. K., "Designing Multifunctional Characteristics by Mimicking Skull Structure", Mechanical Engineering Department, New Mexico Institute of Mining and Technology, 2005.

[7] Wolff, J., The law of Bone Remodeling , Berlin: Springer Verlag; 1986 [English translation from German].

[8] Gefen A. and Seliktar, "Comparison of the Trabecular architecture and the isostatic stress flow in the human calcaneus", Medical Engineering & Physics, 26 (2004), 119-129

[9] Buechner P., Lakes R., Swan C., Brand R., "A Broadband Viscoelastic Spectroscopic Study of Bovine Bone: Implications for Fluid Flow", Annals of Biomedical Enginering, Vol. 29, 2001, Biomedical Engineering Society.

[10] Crawford J., "Modeling Blast Resistant Protection Systems Composed of Polymers and Fabric", Karagozian & Case, Burbank CA.

[11] Eamon C., "Reliability of Concrete Masonry Unit Walls Subjected to Explosive Loads", Journal of Structural Engineering, Vol. 133, No. 7, July 2007.

[12] Ma G., Ye Z., "Energy absorption of double-layer foam cladding for blast alleviation", School of Civil and Environmental Engineering, Nanyan Technological University, Singapore, 2005.

[13] Sriram R., Vaidya U., Kim J., "Blast impact response of aluminum foam sandwich composites", Journal of Materials Science, Vol. 41, 13, 2006.

[14] Thomsen O., et. all, "Sandwich Structures 7: Advancing with Sandwich Structures and Materials", Proceedings of the 7th International Conference on Sandwich Structures, Aalborg, Denmark, 2005.

[15] Dvorak G., Bahei-El-Din Y., "Enhancement of Blast Resistance of Sandwich Plates", Department of Mechanical, Aerospace and Nuclear Engineering, Rensselaer Polytechnic Institute, NY, 2006.

[16] Bahei-El-Din Y., Dvorak G., "Behavior of Sandwich Plates Reinforced with Polyurethane/Polyurea Interlayers under Blast Loads", Journal of Sandwich Structures and Materials, Vol. 9, No. 3, 2007.

[17] Nesterenko V., "Shock (Blast) Mitigation by "Soft" Condesded Matter", University of California, San Diego, CA, 2003.

[18] Muszynski L., Purcell M., "Composite Reinforcement to Strengthen Existing Concrete Structures against Air Blast", Journal of Composites for Construction, Vol. 7, 2, 2002.

[19] Vaziri A., Xue Z., Hutchinson W., "Metal Sandwich Plates with Polymer Foam-Filled Cores", Journal of Mechanics of Materials and Structures, Vol. 1, No. 1, 2006.

[20] Yen C., Skaggs R., Cheeseman B., "Modeling of Shock Mitigation Sandwich Structures for Blast Protection", 3rd First International Conference on structural Stability and Dynamics, 2005, Florida, U.S. Army Research Laboratory, 2005.

[21] Mohamed M., "3Weave Multi-functional Composites: Load Bearing and Armor Protection", 3TEX Inc., ONR-SBIR, 2006.

[22] NASA Tech Briefs, "Technical Support Package: Lightweight Energy Absorbers for Blast Containers", MFS-31563, 2007

[23] Gibson J., Ashby M., "Cellular solids Structure and properties", Cambridge University Press, 1997.

[24] Lee T., Lakes R., "Anisotropic polyurethane foam with Poisson's ratio greater than 1", Journal of Material Science, 32, 1997.

[25] Li Y. Mi, Susannah P. Fritton, Mitra Basu, Stephen C. Cowin, "Analysis of avian bone response to mechanical loading-Part One: Distribution of bone fluid shear stress induced by bending and axial loading", Biomechanics and Modeling in Mechanobiology, Springer-Verlag Berlin Heidelberg, 2005.

[26] Campbell F., "Secondary Adhesive Bonding of Polymer-Matrix Composites", ASM Handbook, Volume 21, 2001.

[27] Oosthuizen C., "Compressible Fluid Flow", McGraw-Hill Series in Mechanical Engineering, McGraw-Hill, 1997.

[28] Zhong, W., "Analysis of fluid flow through fibrous structures".

[29] Aaltosalmi U., Kataja M., Koponen A., Timonen J., Goel A., Lee G., Ramaswamy S., "Numerical Analysis of Fluid Flow Through Fibrous Porous Materials", Univ. Jyvaskyla Physics Dept., VTT Processes, Univ. Minnesota Wood Paper Science Dept.

[30] Rogers Corporation, http://www.rogerscorporation.com/hpf/CT/Poron-I/industrial_tech_info.htm

[31] Lu G., Xio Z., "Mechanical Properties of Porous Matherials." Journal of Porous Materials, 6, 1999.

[32] Dobson, C., Langton, C., Fagan, M., "Simulation of Cancellous Bone Remodeling, Sturcture and Biomechanical Stresses associated with Osteoporosis: A Review", Computer Simulation & Modelling in Medicine, Volume 1, Issue 2.

[33] Harrigan T., Mann R., Journal of Materials Science, 1984, 19, 761.

[34] Pleskanchevskii Y., Shil'ko S., Chernous D., "Structural Meodeling in the Mechanics of Porous Materials", Mechanics of Composite Materials, Vol. 39, No. 2, 2003.

[35] Ippili R., Widdle R., Davies P., Bajaj A., "Modeling and Identification of Polyurethane Foam in Uniaxial Compression: Combined Elastic and Viscoelastic Response", Ray W. Gerrick Laboratories, School of Mechanical Engineering, Purdue University, 2003 ASME Design Engineering Technical Conferences, Conference on Mechanical Vibration and Noise, Chicago, Illinois USA, September 2-6, 2003.

[36] Puri T., Widdle R., Davies P., Bajaj A., "Models to Characterize Mutiple Time Scale Behavior in Polyurethane Foam", Ray W. Herrick Laboratories, Purdue University.

[37] Widdle R., Bajaj A., Davies P., "Linking of Continuum and Microstructure Models of Foam to Aid in the Design of Automotive Seating", SAE International, SAE Technical Paper Series, Human Factors in Driving and Telematics, and seating Comfort, 2004.

[38] NASA Glenn Research Center, Ballistic Impact Facility, Structural Mechanics and Dynamics Branch, Structures and Acoustics Division, http://ballistics.grc.nasa.gov/pages/hopkinson%20bar.html

[39] Yi J., Boyce M., Lee G., Balizer E., "Strain Rate Dependence of the Stress-Strain Behavior of Polyurethane", Department of Mechanical Engineering, Massachusette Institute of Technology, Naval Surface Warfare Center.

[40] Widdie R., Bajaj A., Davies P., "Micromechanical Modeling of Polyurethane Foam", presentation.

[41] Wang L., Tseng K., "A multi-scale framework for effective elastic properties of porous materials", Department of Civil and Environmental Engineering, Vanderbilt University, Journal of Materials Science, 38, 2003.

[42] Spinhirne N., "Finite Element Analysis of Compressible, Fluid-Saturated Polyurethane Foam", New Mexico Institute of Mining and Technology, 2006

[43] Brace W., Journal of Geophysics Research, 82, 3343, 1977.

[44] Warren W., Draynik A., "The linear elastic properties of open-cell foams.", Journal of Applied Mechanics, 55, 341, 1988.

[45] Xue Z., Hutchinson J., "A comparative study of impulse-resistant metal sandwich plates", Division of Engineering and Applied Sciences, Harvard University, International Journal of Impact Engineering, 30, 2004.

[46] Goldstein R., Gordeev Y., Kornev K., "Features of deformation of poroelastic media with low structural strength", C. R. Academy of Science Paris, t. 328, Se'rie II b, 2000.

[47] Benallal A., Comi C., "On numerialc analyses in the presence of unstable saturated porous materials", International Journal for Numerical Methods in Engineering, 56, 2003

[48] Yong C., Jun Z., Yu W., Ping T., "Non-linear transient analysis of a blast-loaded circular plate resting on a non viscous fluid", State Key Laboratory of Vibration Shock and Noise, Naval Ship Research Center, China Academy of Engineering Physics, International Journal of Pressure Vessels and Piping, 82, 2005.

[49] Hanssen A., Enstock L., Langseth M., "Close-range blast loading of aluminium foam panels", Structural Impact Laboratory, Department of Structural Engineering, Norwegian University of Science and Technology, International Journal of Impact Engineering, 27, 2002.

[50] Treloar L., "The Phusics of Rubber Elasticity", Clarendon Press, Oxford, 1958.

[51] Rusch K., Journal of Cellular Plastics, 7, 78, 1971.

[52] "Standard Test Methods for Flexible Cellular Matherials-Slab, Bonded, and Molded Urethane Foams", Annual Book of ASTM Standards, Section Eight, Volume 8.02, Plastics (II), ASTM International, 2003.

[53] "Standard Test Methods for Rubber Property-Resilience Using a Goodyear-Healey Rebound Pendulum", Annual Book of ASTM Standards, Section Nine, Volume 9.01, Rubber, ASTM International, 2003.

[54] Kaiser, M., "Advancements in the Split Hopkinson Bar Test", Virginia Polytechnic Institute and State University, 1998

[55] Frew, D., Forrestal, M., Chen, W., "A Split Hopkinson Pressure Bar Technique to Determine Compressive Stress-strain Data for Rock Materials", Journal of Experimental Mechanics, Vol. 41, No. 1, 2001

[56] Chen, W., Zhang, B., Forrestal, M., "A Split Hopkinson Bar Technique for Low-impedance Materials", Journal of Experimental Mechanics, Vol. 39, No. 2, June 1999

[57] TM 5-1300, "Structures to Resist the Effects of Accidental Explosions", Departments of the Army, the Navy, and the Air Force, November, 1990

[58] Baker W., "Explosions in Air", University of Texas Press, Austin, TX, 1973

[59] Tang M. and Baker Q., "Non Ideal Blast Waves", 1999 International Workshop on Non-Ideal Explosives

[60] Olatidoye, O., Sarathy, S., Jones, G., McIntyre, C., and Milligan L., "A Representation Survey of Blast Loading Models and Damage Assessment Methods for Building Subject to Explosive Blasts", CEWES MSRC/PET TR/98-36, Clark Atlanta University, Atlanta, GA.

[61] Olson, D., "Ideal vs. Non-Ideal the TNT Equivalency Myth", EMRTC Safety Course for Explosive Firing Site and Laboratory Personnel", Section 11, Socorro, NM, 2002

[62] White F., "Viscous Fluid Flow, Third Edition, International Edition", McGraw Hill Education (Asia), 2006.

[63] TIGERWIN v4.0, Computer Software, MS-DOS, Blasting Analysis International, 1996

[64] Yeager, K., "Improvised Explosives and Non-Ideality: Understanding the Threat and the Science", 2001 International Workshop on Non-Ideal Explosives

[65] Cooper, P., "Explosives Engineering", Wiley and Sons Publishers, New York, NY, 1996

[66] HNDM-1110-1-2, "Suppressive Shields-Structural Design and Analysis Handbook", U.S. Army Corps of Engineers, Huntsville, AL, 1977

[67] Tedesco J., McDougal W., Ross C., "Structural Dynamics – Theory and Applications", Addison Wesley Longman, Inc., 1999.

[68] Xue Z., Hutchinson J., "Preliminary assessment of sandwich plates subject to blast loads", Division of Engineering and Applied Sciences, Harvard University, International Journal of Mechanical Sciences, 45, 2003.

[69] Jacinto A., Ambrosini R., Danesi R., "Dynamic response of plates subjected to blast loading", Proceedings of the Institution of Civil Engineers, Structures & Buildings 152, issue 3, 2002.

[70] Jones, Norman, "Structural Impact", Cambridge University Press, pg.'s 29-35 & 110-139, 1989.

[71] Bulson P., "Explosive loading of engineering structures: a history of research and a review of recent developments", Taylor and Franci, 1997.

[72] Ramirez J., "Characterization of Shear-Thickening Fluid-Filled Foam Systems for Use in Energy Absorption Devices", Department of Mechanical Engineering, Massachusetts Institute of Technology, 2004.

[73] IBM, Public Library, http://publib.boulder.ibm.com/infocenter.com

[74] ANSYS, Hyperelasticity, http://www1.ansys.com/customer/content/documentation/80/ansys/thy_mat5.html

[75] Monolithic Dome Articles, "Free Information, Dome Calculations", http://www.monolithic.com/plan_design

[76] MatWeb, "Material Property Data", http://www.matweb.com, Automation Creations, Inc.

7. Appendix A, Data Plots from the EMRTC Testing

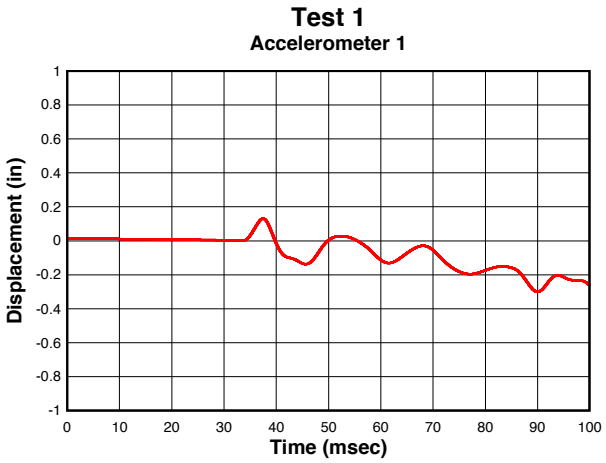

Figure 116: Test 1 displacement wet flat sample EMRTC

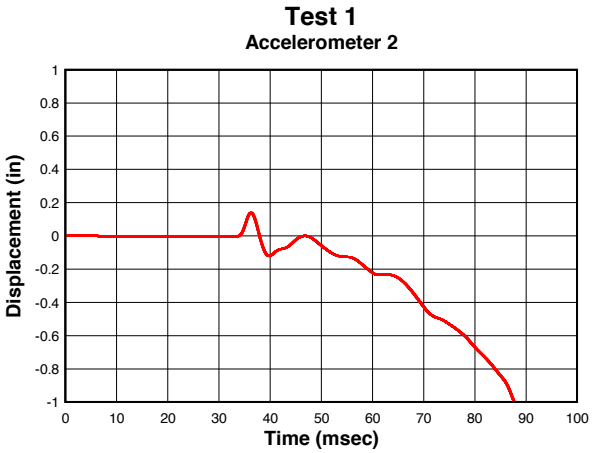

Figure 117: Test 1 displacement flat dry sample EMRTC

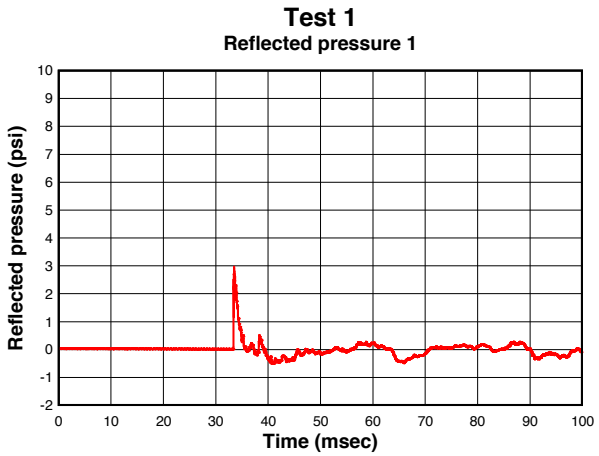

Figure 118: Test 1 reflected pressure top EMRTC

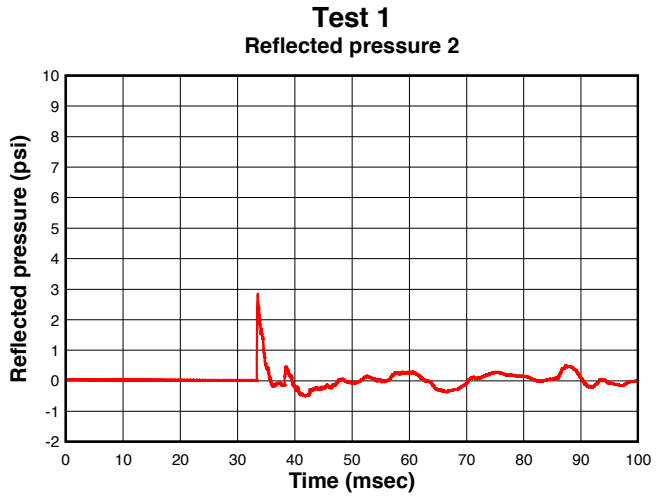

Figure 119: Test 1 reflected pressure bottom EMRTC

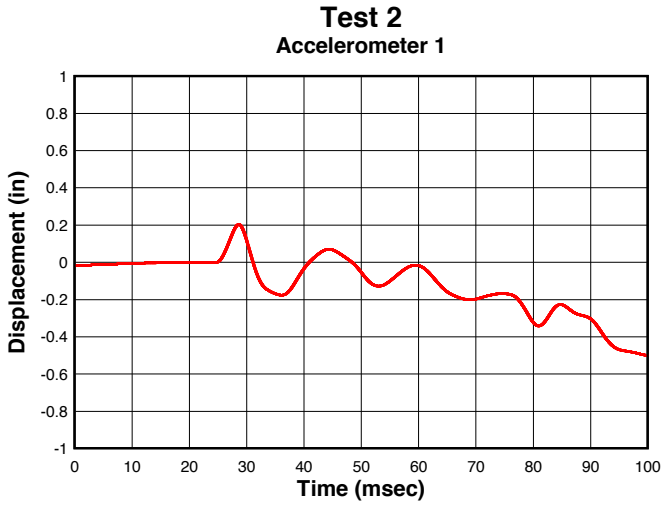

Figure 120: Test 2 displacement wet flat sample EMRTC

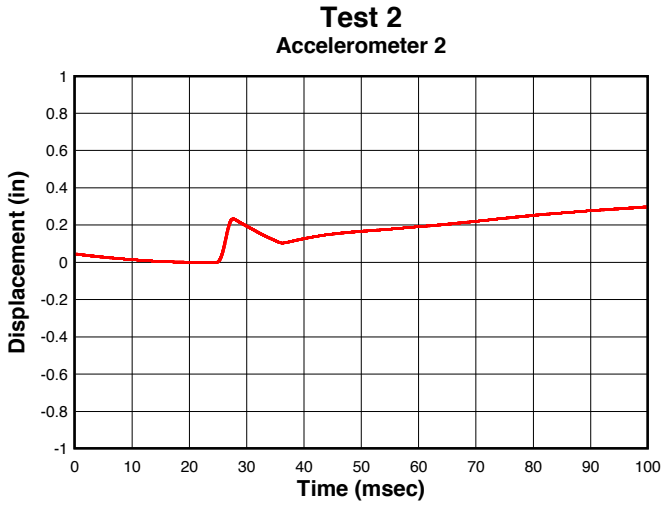

Figure 121: Test 2 displacement flat dry sample EMRTC

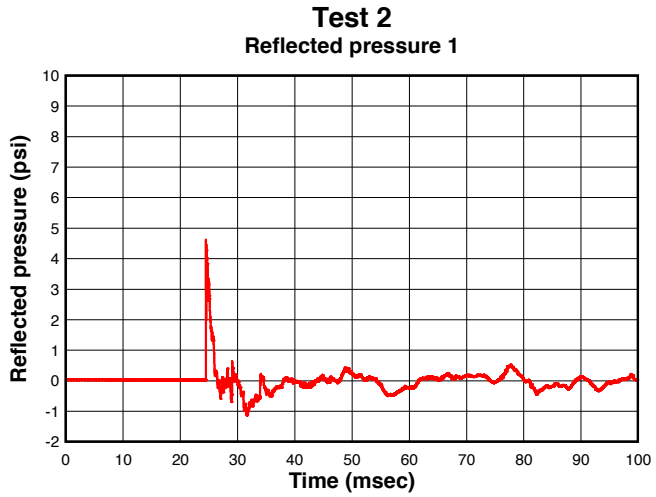

Figure 122: Test 2 reflected pressure top EMRTC

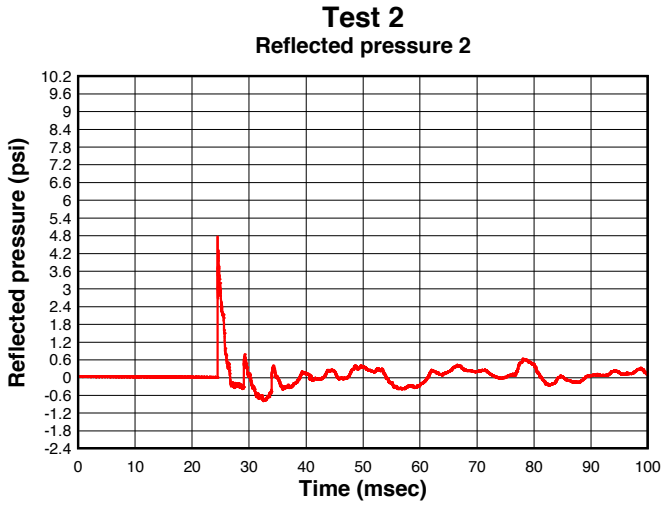

Figure 123: Test 2 reflected pressure bottom EMRTC

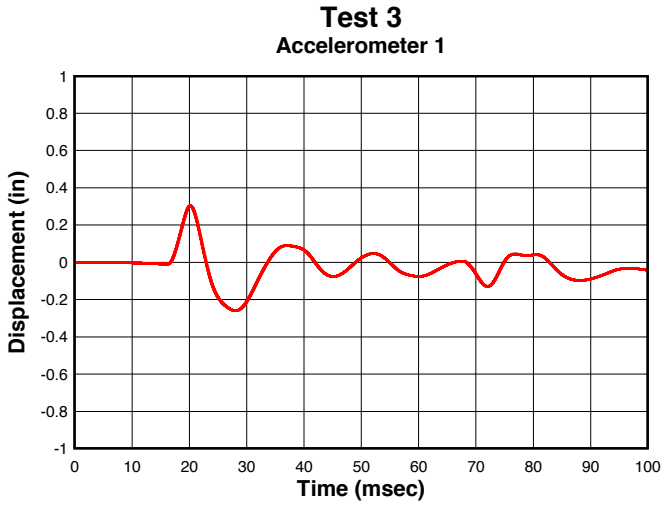

Figure 124: Test 3 displacement flat wet sample EMRTC

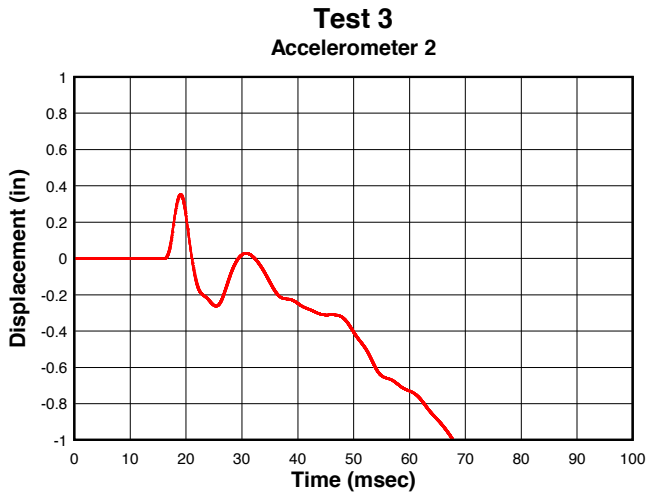

Figure 125: Test 3 displacement flat dry sample EMRTC

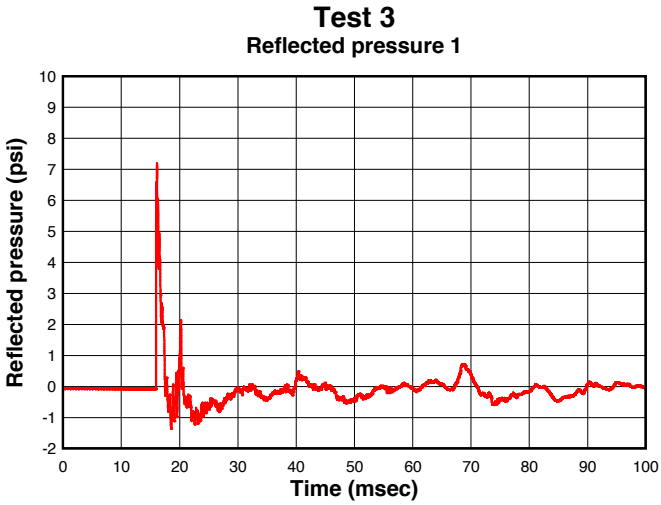

Figure 126: Test 3 reflected pressure top EMRTC

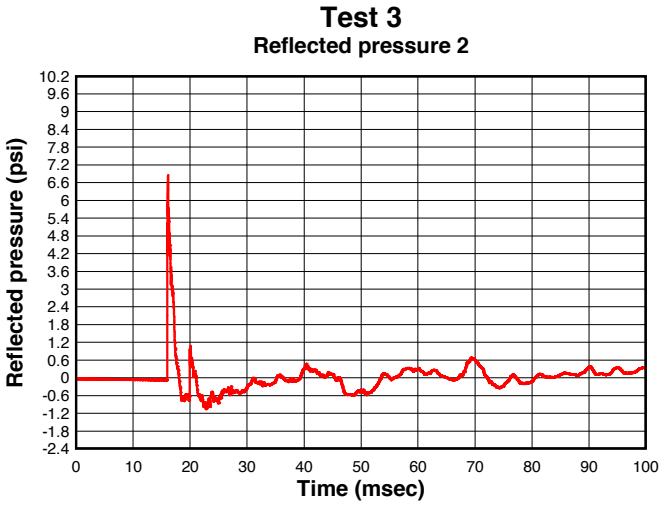

Figure 127: Test 3 reflected pressure bottom EMRTC

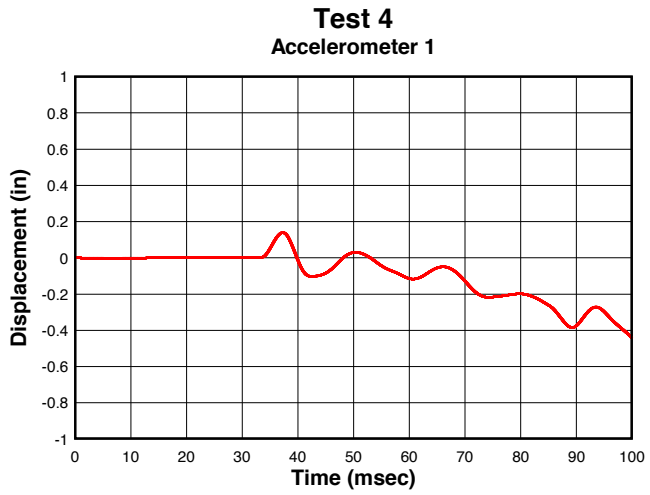

Figure 128: Test 4 displacement domed wet sample EMRTC

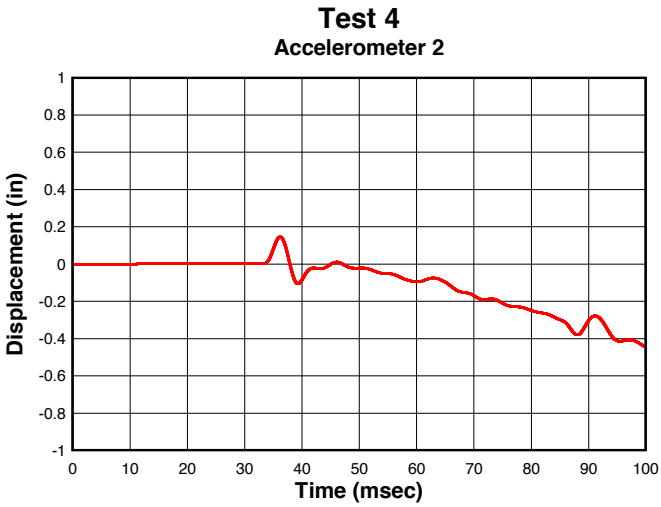

Figure 129: Test 4 displacement domed dry sample EMRTC

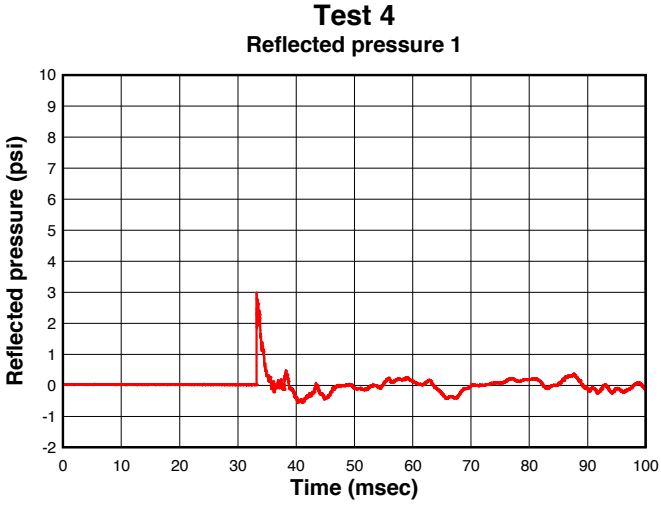

Figure 130: Test 4 reflected pressure top EMRTC

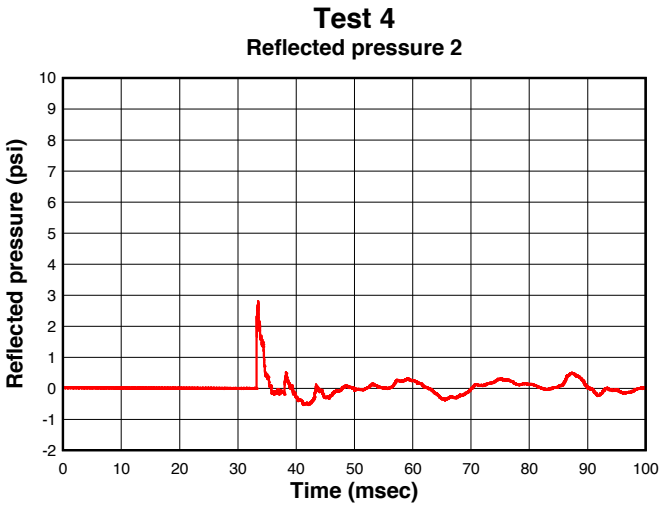

Figure 131: Test 4 reflected pressure bottom EMRTC

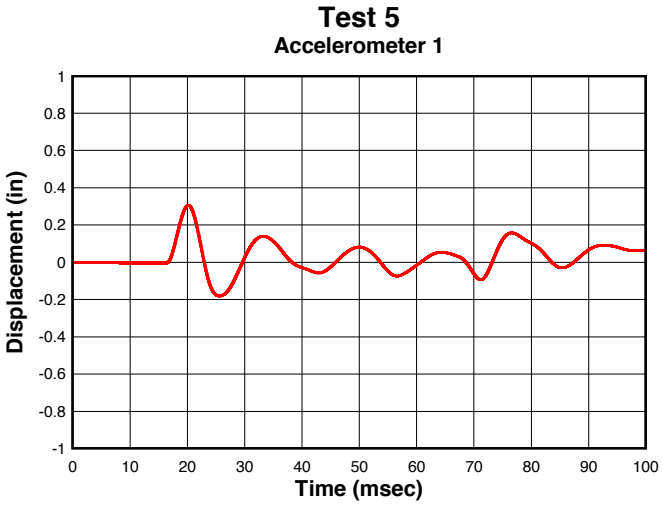

Figure 132: Test 5 displacement domed wet sample EMRTC

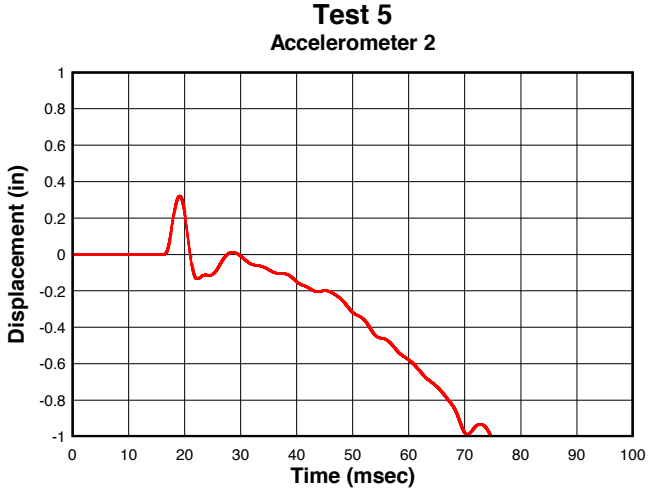

Figure 133: Test 5 displacement domed dry sample EMRTC

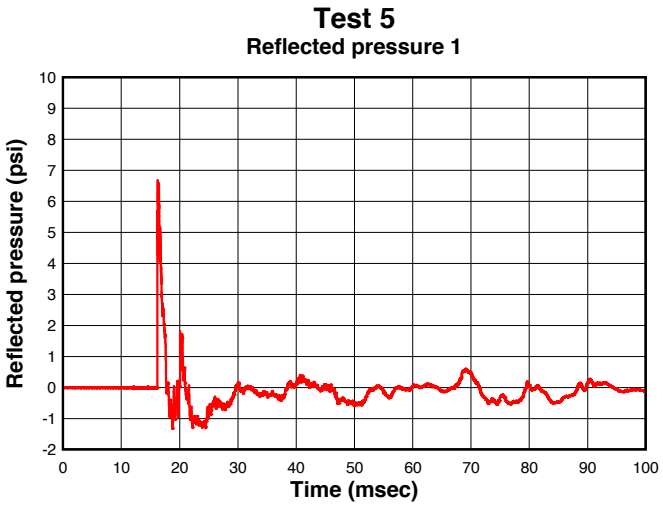

Figure 134: Test 5 reflected pressure top EMRTC

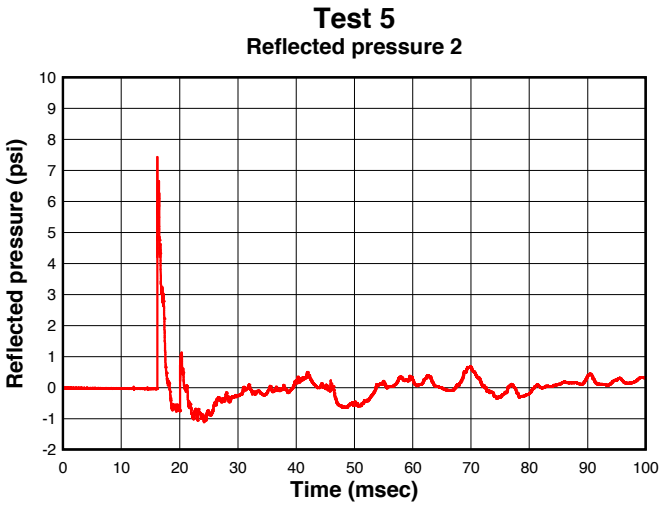

Figure 135: Test 5 reflected pressure bottom EMRTC

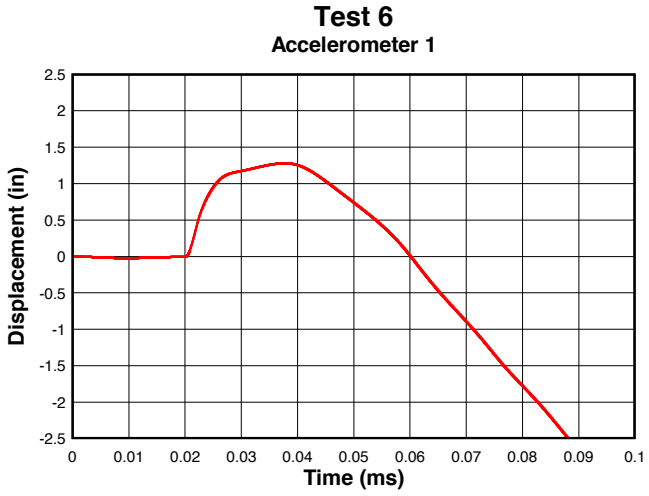

Figure 136: Test 6 displacement domed wet sample EMRTC

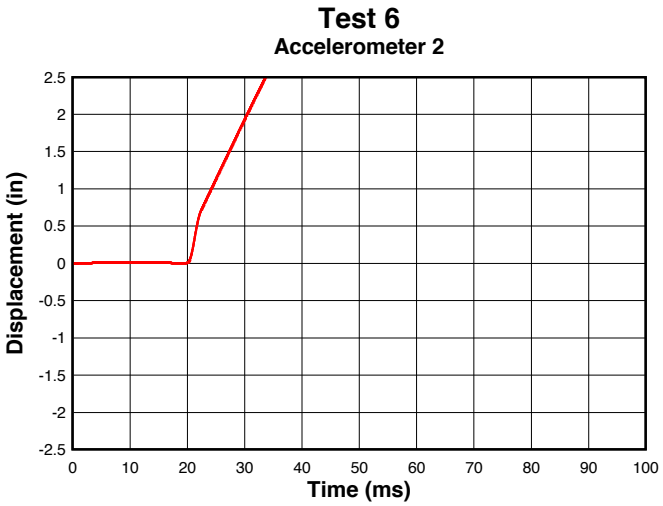

Figure 137: Test 6 displacement domed dry sample EMRTC

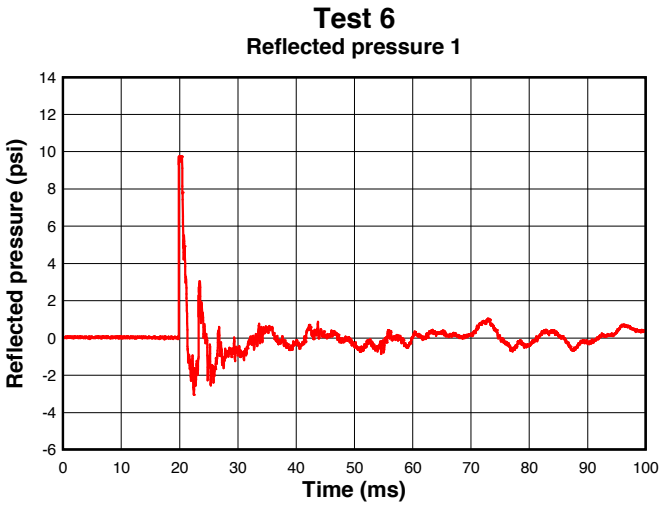

Figure 138: Test 6 reflected pressure top EMRTC

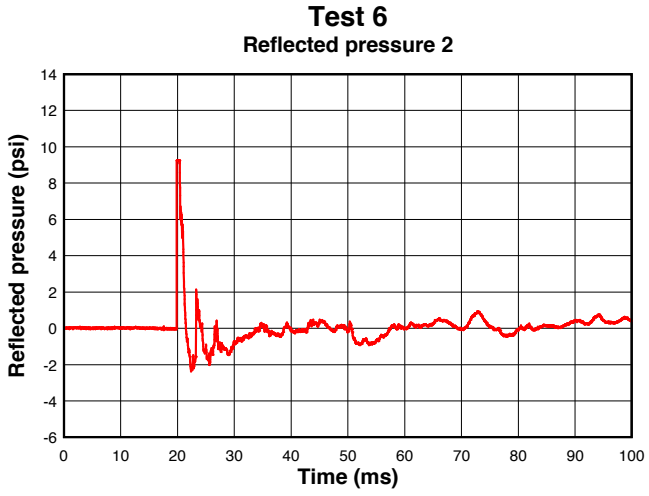

Figure 139: Test 6 reflected pressure bottom EMRTC

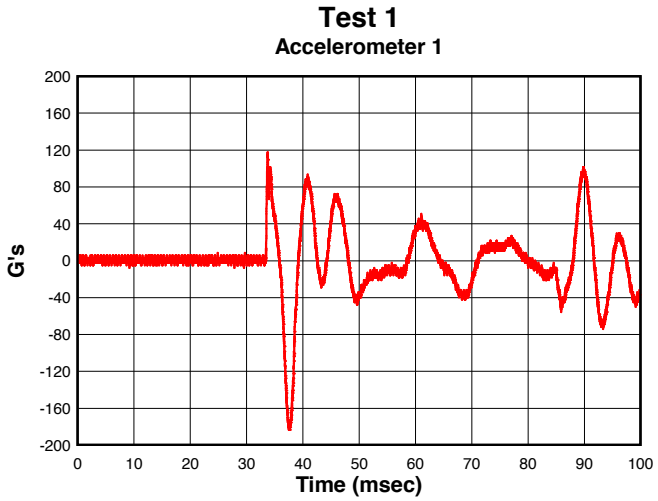

Figure 140: Test 1 G's flat wet sample EMRTC

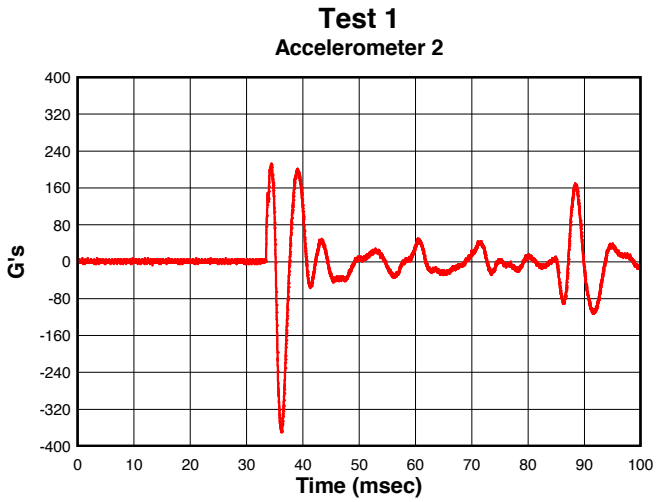

Figure 141: Test 1 G's flat dry sample EMRTC

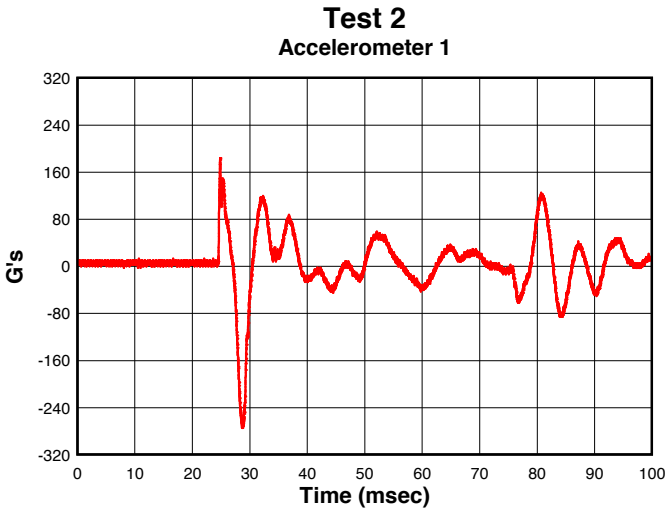

Figure 142: Test 2 G's flat wet sample EMRTC

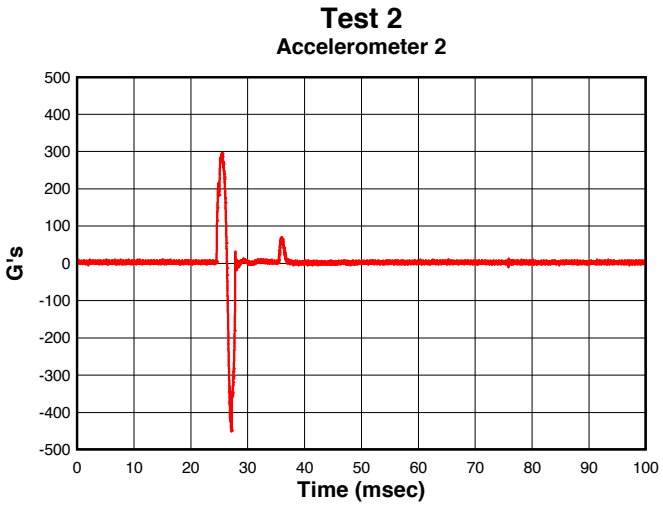

Figure 143: Test 2 G's flat dry sample EMRTC

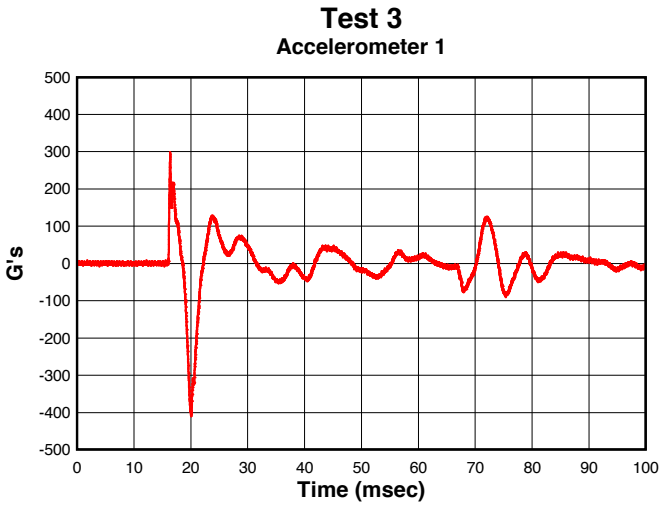

Figure 144: Test 3 G's flat wet sampleEMRTC

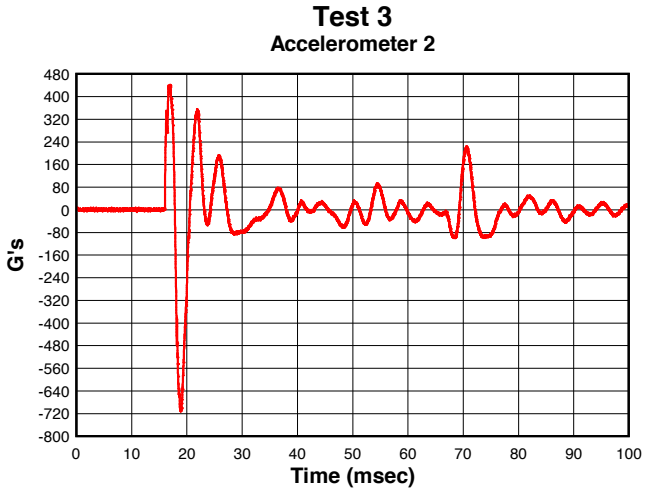

Figure 145: Test 3 G's flat dry sample EMRTC

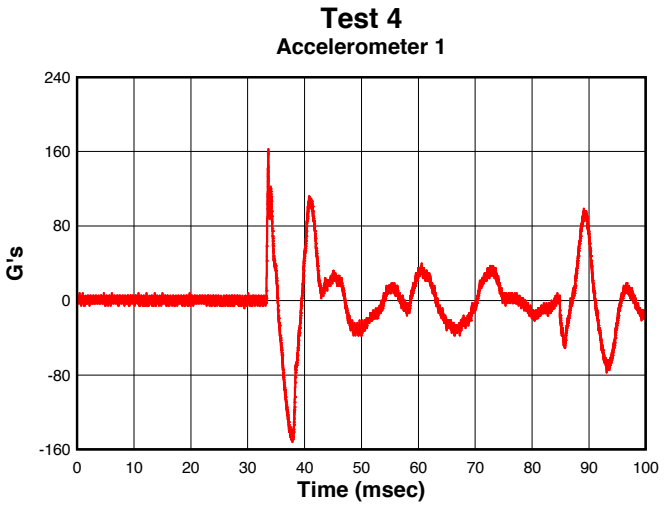

Figure 146: Test 4 G's domed wet sample EMRTC

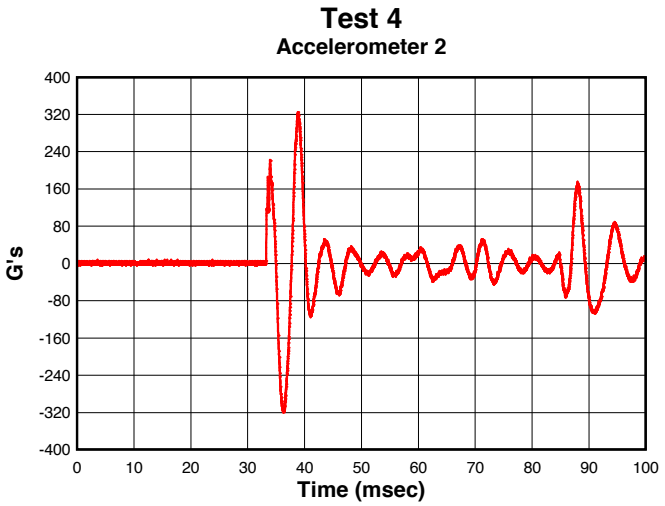

Figure 147: Test 4 G's domed dry sample EMRTC

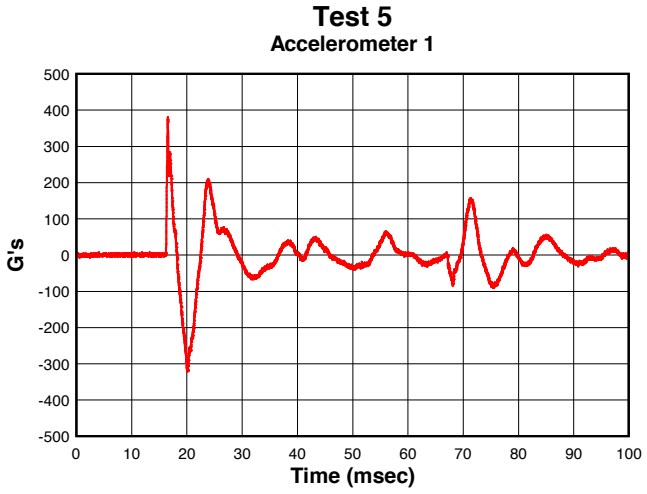

Figure 148: Test 5 G's domed wet sample EMRTC

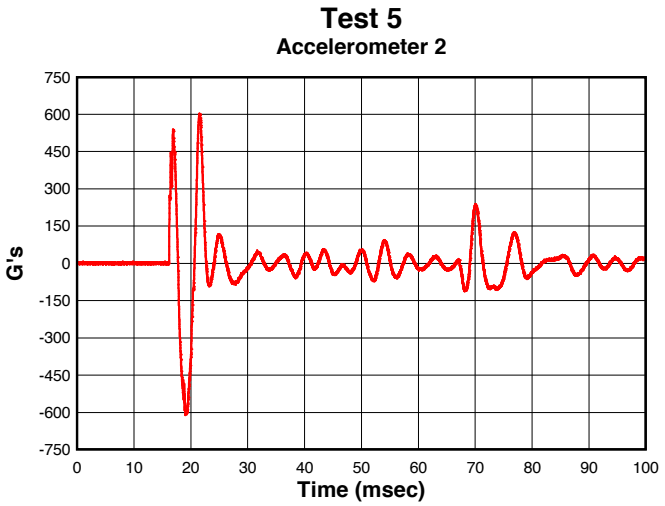

Figure 149: Test 5 G's domed dry sample EMRTC

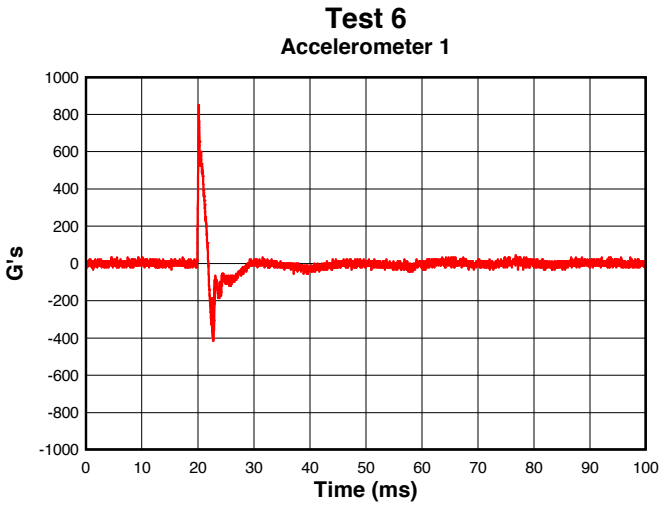

Figure 150: Test 6 G's domed wet sample EMRTC

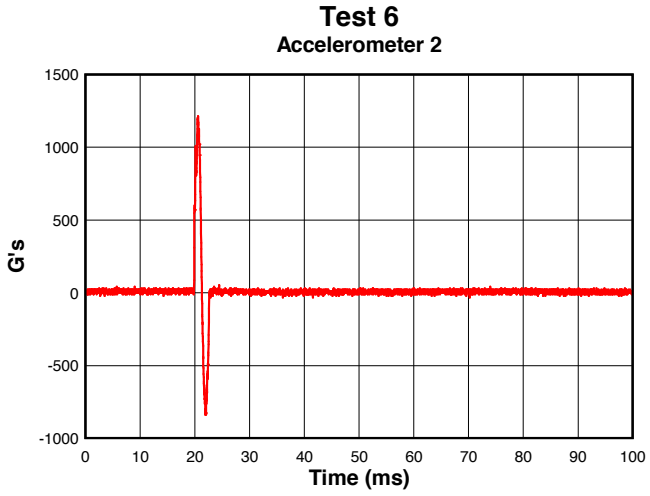

Figure 151: Test 6 G's domed dry sample EMRTC

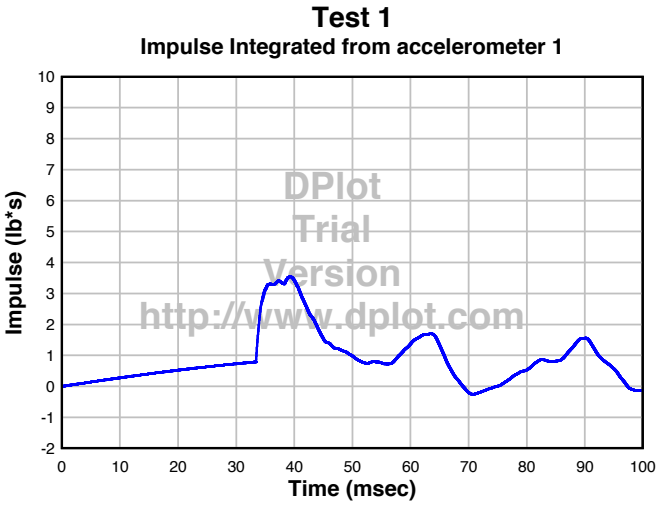

Figure 152: Test 1 impulse top EMRTC

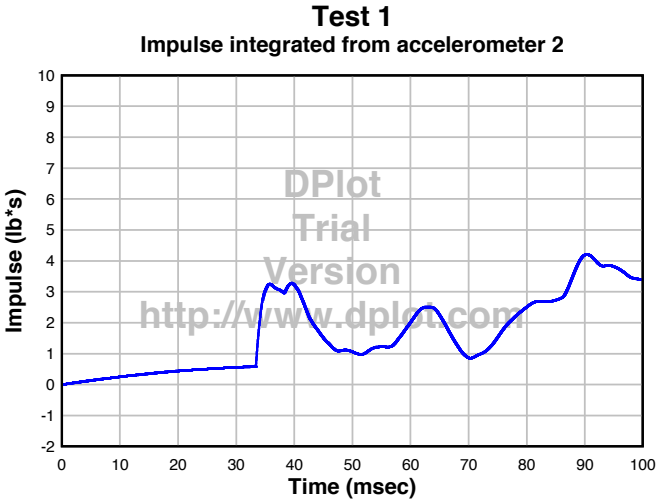

Figure 153: Test 1 impulse bottom EMRTC

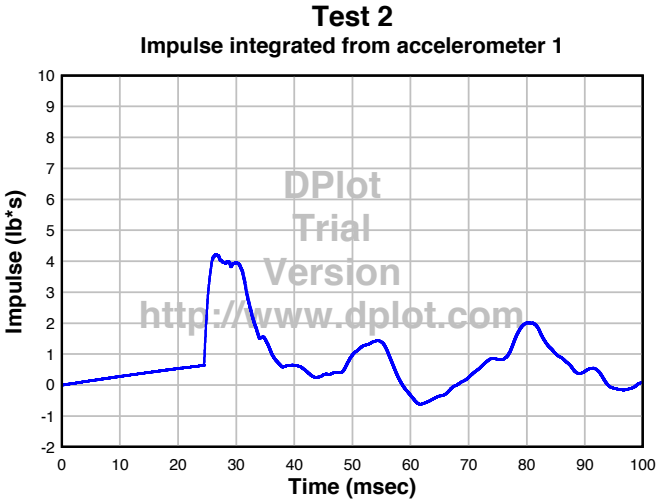

Figure 154: Test 2 impulse top EMRTC

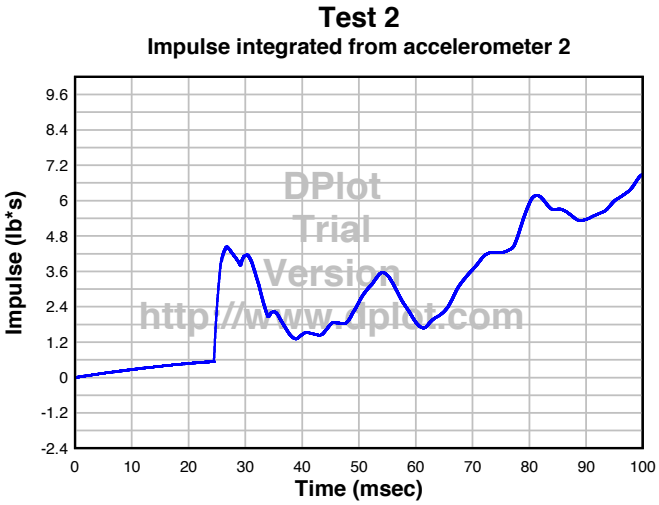

Figure 155: Test 2 impulse bottom EMRTC

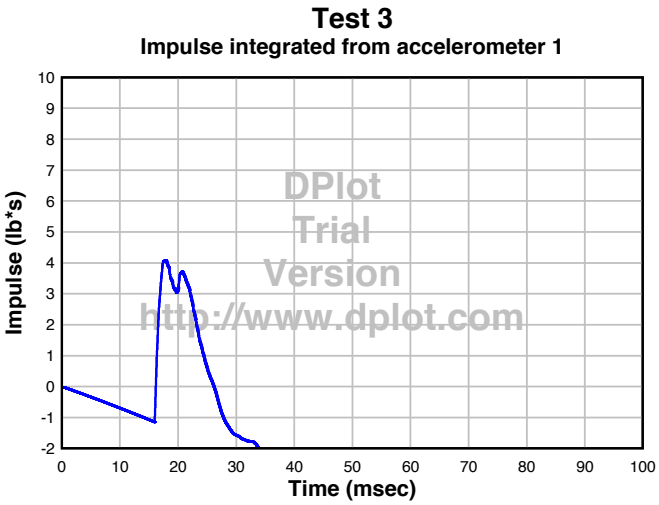

Figure 156: Test 3 impulse top EMRTC

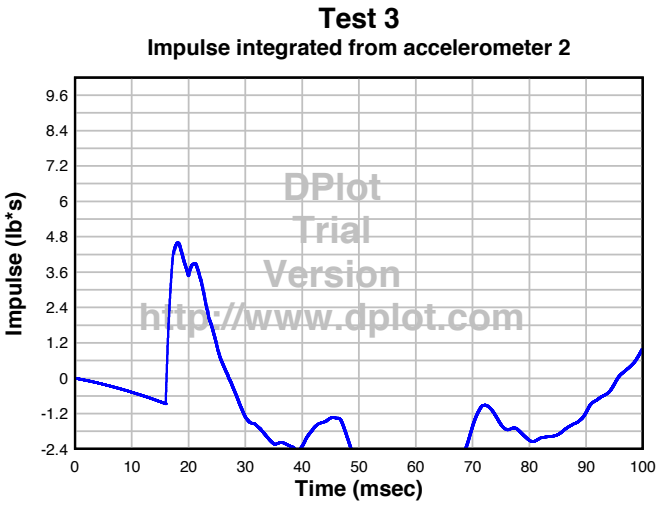

Figure 157: Test 3 impulse bottom EMRTC

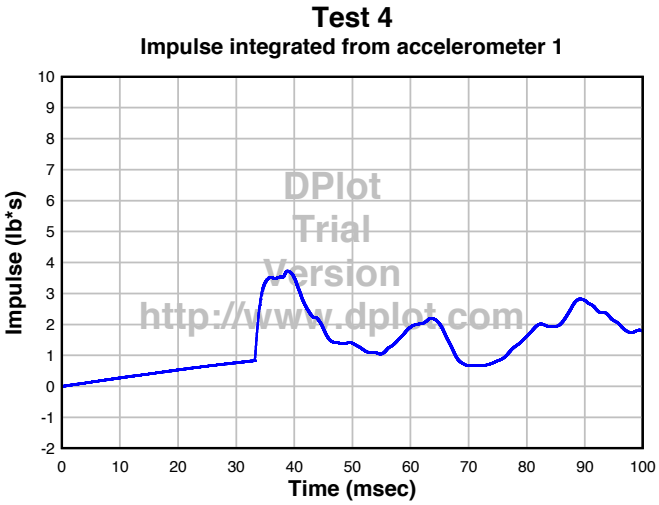

Figure 158: Test 4 impulse top EMRTC

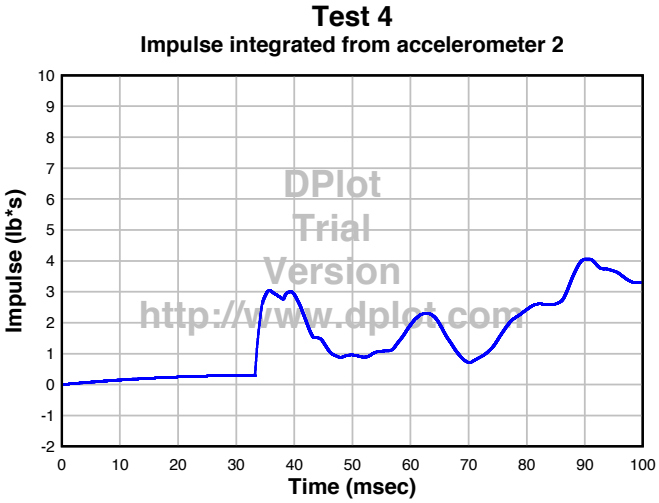

Figure 159: Test 4 impulse bottom EMRTC

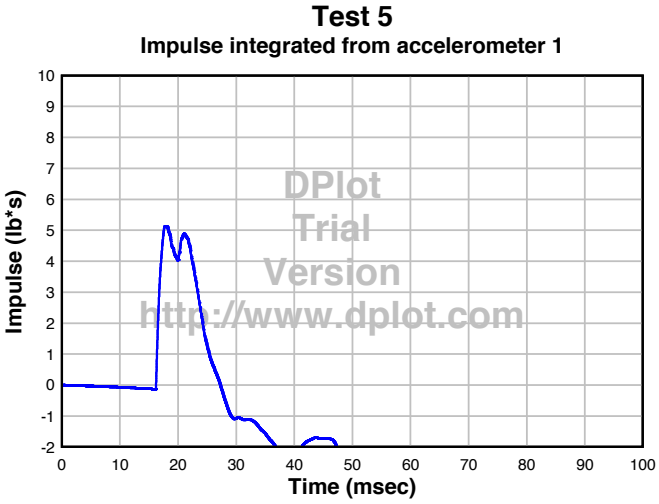

Figure 160: Test 5 impulse top EMRTC

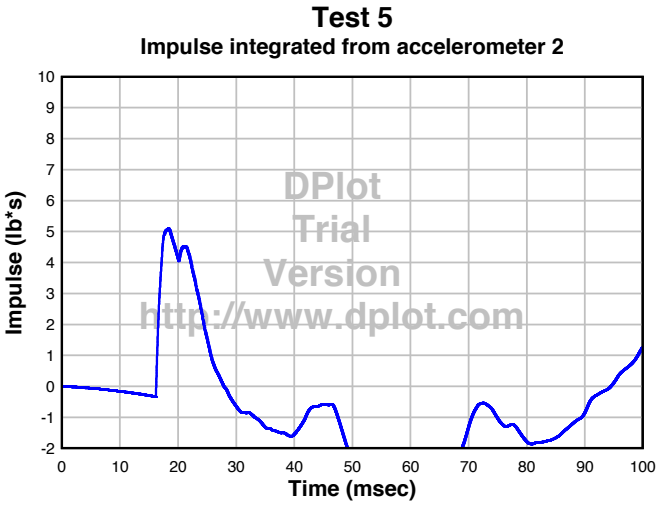

Figure 161: Test 5 impulse bottom EMRTC

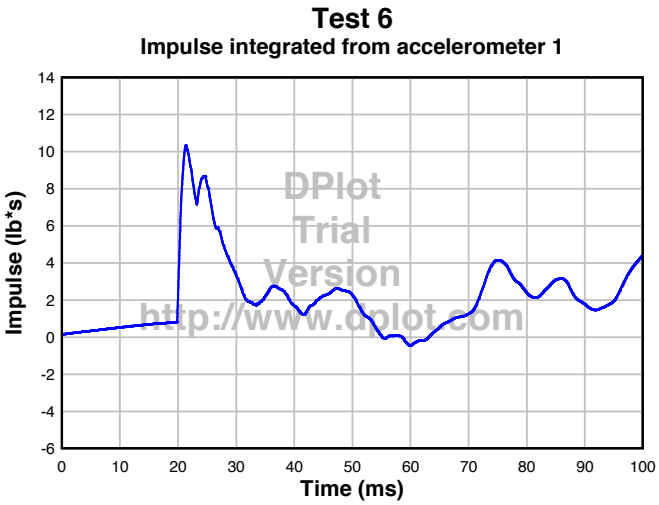

Figure 162: Test 6 impulse top EMRTC

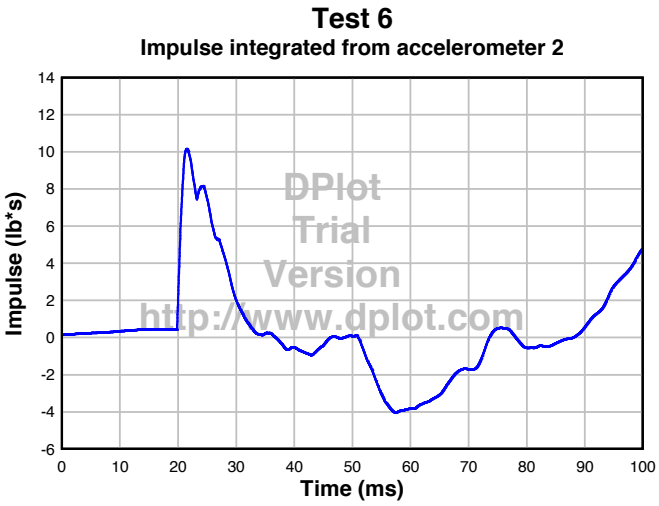

Figure 163: Test 6 impulse bottom EMRTC